STRUCTURAL BEHAVIOUR OF INTERLOCKING CONCRETE BLOCK PAVEMENT LAID OVER CONFINED BEDDING SAND

A thesis submitted to Indian Institute of Technology Guwahati

for the partial fulfilment of the award of the degree

of

Doctor of Philosophy

by

Ibaiahun Nongbet Sohlang

(Roll No. 146104023)

Under the guidance of

Prof. Teiborlang L. Ryntathiang

DEPARTMENT OF CIVIL ENGINEERING

INDIAN INSTITUTE OF TECHNOLOGY GUWAHATI

GUWAHATI-781039, INDIA

May 2024

Certificate

This is to certify that the thesis titled “Structural Behaviour of Interlocking Concrete Block Pavement Laid over Confined Bedding Sand” submitted by Ibaiahun Nongbet Sohlang to Indian Institute of Technology Guwahati for the award of the degree of Doctor of Philosophy is a record of bonafide research work carried out by her under my supervision and guidance. In my opinion, the thesis work has reached the requisite standard fulfilling the requirement for the degree of Doctor of Philosophy.

The findings presented in this thesis have not been submitted in part or full to any other university or institute for the award of any degree or diploma.

Dr. Teiborlang L. Ryntathiang
Professor
Department of Civil Engineering
IIT Guwahati
Guwahati- 781039, Assam, India

Place: IIT Guwahati
Date: 31/05/2024

Declaration

I hereby declare that this thesis represents my own research work which has been carried out during my Ph.D. at the Indian Institute of Technology Guwahati. The work presented in this thesis has not been previously included in any other thesis submitted for a degree or other qualifications. Wherever contributions from others are involved, I have provided relevant acknowledgement or reference to the original source. I also declare that I have adhered to all academic ethics and responsibilities and have not misinterpreted or fabricated or falsified any idea/ data/ fact/ source in my submission. This thesis, in any way, does not endorse any proprietary products or technologies.

Place: IIT Guwahati
Date: 31/05/2024

Ibaiahun Nongbet Sohlang
Roll No. 146104023

Acknowledgement

I wish to convey my heartfelt appreciation to my esteemed mentor, Prof. Teiborlang L. Ryntathiang, for his consistent guidance and unwavering encouragement throughout the course of my thesis. His dedication and belief in my capabilities have been instrumental, directing me towards the pertinent sources and perspectives in pavement engineering. I express my profound gratitude to Dr. Nelson Muthu, whose guidance and support were invaluable throughout my work. His consistent encouragement kept me actively involved, and his technical expertise played a crucial role in unravelling the complexities of my research problem.

I extend sincere gratitude for the substantial contributions of my respected committee members, Prof. Subashisa Dutta, Prof. Mallikarjuna C., Prof. D. Pamu, and Dr. Hrishikesh Sharma, whose valuable insights have significantly enhanced the quality of this thesis. I want to extend my gratitude to Dr. Anjan Kumar S. for being the guiding light through his wisdom and inspiration to grow as a learner.

I am profoundly thankful to Mr. Avinesh Kumar and Dr. Pallab Jyoti Das for their tremendous support and assistance in completion of my thesis. I extend special appreciation to Dr. Khwairakpam Selija, Ms. Nicola Thounaojam, Dr. Santanu Pathak, Dr. Nishant Bhargava, Dr. Bhaskar Pratim Das, Mrs. Saswati Das, Dr. Supratim Kaushik, Dr. Atmaprakash Sharma, and my dearest friends, Lt. Col. Shishir Makwana, Menan, Aruna, Boro, Banchiva and Juhi for their relentless encouragement throughout my Ph.D. journey. I also extend appreciation to the technical and administrative staff at IITG, with special mention to Mr. Kuldeep Kalita, Mr. Mrinal Sarmah, Mr. Balen Kalita, Mr. H Upadhyaya, and Mr. Soroj Patowary for their consistent assistance.

My gratitude extends to IITG for providing the necessary research facilities, and I express gratitude to K. K. EnviroTech Pvt. Ltd., Kolkata. for their material support. Special recognition goes to CIPET- CSTS - Guwahati for their assistance in plastic sample testing.

Most importantly, all the strength throughout the years would not have been possible without the enduring faith and unwavering support of my family. The consistent encouragement from my parents has inspired my pursuit of my goal, and this thesis is a tribute to them.

Abstract

Interlocking Concrete Block Pavement (ICBP) commonly exhibits structural and premature failures such as rutting and local settlement. Over time, these surface depressions can exacerbate the issues, leading to joint widening, block cracking, block spalling, and edge failure. A primary cause of these surface layer failures is the bedding layer, a sand bed compacted to a thickness of 20-40 mm, which is designed as a non-structural component. However, this thin layer is responsible for transferring vehicular stresses to the base and ultimately to the foundation, subjecting it to higher stress levels than the underlying rigid base.

To enhance the serviceability of ICBP, it is essential to strengthen all layers, including the bedding layer. The load-bearing capacity of the ICBP and the stability of the bedding layer can be significantly improved by implementing geocells tailored for this specific layer. Geocell technology involves confining the soil within rigid polymer walls to improve its load-bearing capacity and prevent early shear failure. The confinement effect of the geocells must be sufficient to retain the collapsible soil within a defined pressure region, achieved by reducing the size of the cell openings. However, the cell walls should not be placed too close together to avoid insufficient compaction of the infill material.

Since current construction practices and materials for ICBP are based on established guidelines with limited exploration into alternative methods, there is a need to develop a new construction approach of the bedding layer by implementing geocell stabilisation. Geocell technology operates on the principle that plastic walls can effectively alleviate excessive stress and restrict the horizontal movement of sand, enhancing the stability of the bedding layer. The use of geocells in a granular layer is precisely customised to match the specific stress conditions of that layer. Therefore, existing geocells are unsuitable for stabilisation in the bedding layer due to its thin profile and specific location within the pavement structure. Hence, it is justified to explore the potential implementation of geocell technology in the bedding layer.

A new construction method for the bedding layer utilising tailored geocell technology is investigated. Custom geocells with openings of 350 mm × 350 mm, 250 mm × 250 mm, and 150 mm × 150 mm, manually sealed to a height of 40 mm, are prepared from 0.32 mm thick HDPE sheets. The infill material is sand of a specified type and gradation. Both confined and unconfined bedding layers are compacted below the surface layer and on the base, overlying a subgrade and an embankment. A non-repetitive static plate load test is conducted on the surface layer, and pavement behavior is simulated using the finite element method (FEM). Confinement reduces early shear failure of the sand, and the confinement effect improves the stiffness of the confined layer, enhancing the overall stability of the ICBP.

The influence on the structural capacity of the confined bedding layer is demonstrated by the increase in the modulus of improvement factor (MIF), calculated as the ratio of the simulated elastic modulus of confined bedding layers to that of unconfined bedding layers. The MIF for confined bedding layers with geocell openings of 350 mm × 350 mm, 250 mm × 250 mm, and 150 mm × 150 mm are found to be 5.09, 13.26, and 37.13, respectively.

Simplifying the analysis of the current pavement model, further investigation into micromechanical homogenisation of the surface layer suggests representing the composite layer consisting of blocks and jointing sand as a uniform, orthotropic elastic material.

Keywords: Interlocking Concrete Block Pavement, bedding layer, plate load test, finite element analysis, homogenisation.

Table of Contents

List of tables

List of figures

Abbreviations and Notations

BIS	Bureau of Indian Standards
CBR	California Bearing Ratio
E_{base}	Elastic modulus of base
E_{ebl}	Equivalent elastic modulus of confined bedding layer
$E_{foundation}$	Equivalent elastic modulus of foundation
ECA	Equivalent composite approach
FEA	Finite element analysis
FEM	Finite element method
ICBP	Interlocking Concrete Block Pavement
IRC	Indian Roads Congress
KUBC	Kinematic Uniform Boundary Condition
MAE	Mean absolute error
ME	Mean error
MIF	Modulus of Improvement Factor
ML	Silty soil with low plasticity
MoRTH	Ministry of Road Transport and Highways, Government of India
MSE	Mean square error
OMC	Optimum Moisture Content
PBC	Periodic Boundary Condition
RMSE	Root Mean Square Error
RVE	Representative Volume Element
SP	Poorly-graded sand
SUBC	Static Uniform Boundary Condition
WMM	Wet Mix Macadam
2D and 3D	2-dimensional and 3-dimensional respectively
a	Radius of loading plate
c	Cohesion value
c'	Apparent cohesive strength
E	Elastic modulus
p	Pressure applied on loading plate
r	Radial distance measured from centre of loading region
w	Water content
y	Distance along the depth/ thickness

σ_y	Vertical stress
σ_r	Radial stress
ϵ_y	Vertical strain
ϵ_r	Radial strain
δ_y	Vertical displacement
v	Poisson's ratio
ρ_d	Dry density
ϕ	Angle of internal friction
ψ	Dilation angle, given by $\psi=\phi-30^{\circ}$ for cohesionless soil
μ	Coefficient of friction

Chapter 1. Introduction

1.1 General

The earliest widespread use of pavers may be traced back to the Roman Empire, when city streets and colonies were connected by block pavements paved with stone setts (Berechman 2003; Knapton 1996). In the damn and cold weather of Europe, logs were utilised for laying and raising a pavement on bogs (Casparie and Moloney 1994; Tohall et al. 1955). The wooden block pavement later was modified to designer's wooden blocks for the American trackways. The wooden block pavement has also been known as the Nicolson pavement, named after the American inventor, Samuel Nicolson (Nicolson 1854). In the late 19th Century, mass production of bricks, brick surfacing became a commonly utilised for small element surfacing (Jaster et al. 1938; Levi 1889). Stone blocks, bricks, woods and cobblestones were common road surfacing till the First World War, after which during the Second World War, shortages of materials pushed Netherlands to substitute them with concrete pavers (Kellersmann 1980; Meyer 1980; van der Vlist 1980). Then after, the usage of concrete block for surfacing widespread to several nations, with extensive research on its design was done in Australia, South Africa, Britain, and Japan (Kelly et al. 1996; Knapton 1988; Knapton and Barber 1980; Morrish 1986; Rollings 1983; Shackel 1986; Uchida et al. 1992). Concrete block paving only was implemented in India, in the early 1990s during the installation of block pavement in the snowbound area of the West Himalayas (Muraleedharan, T. and Sood 2003).

ICBP has been preferred over conventional pavements in some instances due to its following pros and cons. The advantages of Interlocking Concrete Block Pavement (ICBP) are as follows:

a. Factory-made blocks ensure high quality and reduce quality control issues in the field (van der Vlist 1980).
b. Concrete block pavement is suitable for traffic plying at low speeds, therefore, it is advantageous for high volume roads and intersections (Matthews and Van Niekerk 1996; Miura et al. 1984).
c. In concrete block pavement, digging and reinstatement of trenches for utility repairs is easier. Blocks can be reused multiple times prior they are reduced to rubble (Geense 1980).

d. The surface is insusceptible to surface oxidation and weathering, therefore it is suitable for bus stops, depots, and parking areas where oil spillage is likely to occur (Haviv et al. 2009).
e. Due to its ability to withstand concentrated high stress, it is suitable for heavily loaded areas like container depots, ports, intersections, etc. (Cairns and Gregory 2006; Haviv et al. 2009; Rollings 1983).
f. Recognised cost-efficient installation in India by utilising readily available and affordable labor force and requires basic construction equipment (Cairns and Gregory 2006; Kelly et al. 1996; Marler 2003; Milder 1992).
g. Lower costs, easy and less frequency of maintenance compared to bituminous surfaces .(Cairns and Gregory 2006; Haviv et al. 2009; Matthews and Van Niekerk 1996)
h. There is no requirement of in-situ curing, therefore, traffic can be opened immediately after blocks laying.
i. The surface grey color reflects light more efficiently than black bituminous pavements, thus, reducing street lighting costs (Shackel and Candy 1988).

The demerits of ICBP are as follows:

a. It is inadequate for high-speed facilities in noise-sensitive regions due to excessive road noise generation (Matthews and Van Niekerk 1996). At speed greater than 60 km/h, the noise level exceeds by 5-8 dBA than bituminous pavement (Kanzaki et al. 1984; Shackel and Candy 1988).
b. The riding quality is reasonably good at low-speed traffic (Shackel and Candy 1988).
c. Requires thorough attention to pavement surface and sub-surface drainage due to the potential for water seepage through the joints (Sharp and Armstrong 1984).

At present, ICBP are extensively being used in slow moving traffic lanes on urban roads, Fuel stations, ports, container depots, intersections, parking areas, lay byes, etc., as an alternative option to conventional pavements (Haviv et al. 2009; Miura et al. 1984; Sharp and Armstrong 1984). It is possible to introduce ICBP for primary roads with the fulfilment of safety and long life (Lekso 1980).

1.2 Problem statement

Concrete Block Pavement is a type of pavement, consisting of concrete blocks arranged on a thin bed of bedding sand. Underlying the bedding layer, a base, with/without sub-base and subgrade with/without embankment are laid. Whilst functions of the base and underlying layers of ICBP are similar to that of a conventional pavement, the whole ICBP differs from conventional pavements in the way the surface layer responses under action of vehicular loads. Load transfer across the surface and into the depth is due to the blocks interlocking and supporting against each other. While facilitating load transfer across the surface, along with prevention of water and dirt ingression, and block shifts, the gaps in between the blocks are filled with jointing sand. The surface elements of concrete blocks and the jointing sand are supported by a uniform layer of bedding sand, where the bed serves the following functions:

a. Provides a cushion for the blocks on the hard granular base;
b. Levels the blocks layer to an even riding surface;
c. Prevents crack propagation from the base;
d. The sand ridges below the block gaps provides sand-block interlocking.

ICBP encounters structural failure due to several reasons, such as inadequate base construction, poor drainage, heavy traffic loads, inadequate material quality, and environmental factors like freeze-thaw cycles and their associated soil settlement. Prominent structural failures in ICBP are rutting, block cracking, spalling, and edge failure. Even though measures have been recommended regarding choosing the sand type and gradation for the layer, an improper bedding layer construction also leads to major surface functional and structural deterioration. The prime cause of surface layer failure may be because the bedding layer's functions are merely non-structural even though it is in a highly stressed region of the pavement. Entirely an undulated riding surface complicates the underlying problem and with heavy loads plying on it results in joint widening, loss of sands, blocks displacement and breakage.

The pressure exerted by vehicular loads on the surface is transmitted and distributed throughout the depth of the pavement, with the highest stress occurring in the upper layer and gradually dissipating within the subgrade. Excessive stress caused by the intense vehicular trafficking right under the stiff blocks subjects the sand to collapse, resulting in permanent deformation (Jamshidi et al. 2019). Permanent deformation is the non-recoverable deformation, that is the material has reached the plastic stage and its associated pavement failures are rutting and localised settlement. A permanent deformation causes changes in layer thickness, resulting to blocks shifting, joints widening, water ingression and sand loss through sand sludging. In the course of time, the blocks knocking against each other causes corner and edge chipping.

The prime target of a pavement is its ability to function with minimal maintenance period and no instance for repair during its design period. Sometimes, premature failure occurs and therefore, to prolong the serviceability of the ICBP, it is crucial to strengthen marginal layers, including the bedding layer. Targeting the region of concern, i.e., bedding layer, the load bearing capacity of the ICBP and stability of the bedding layer can be enhanced by tailoring and implementation of geocells. This technology involves confining the soil within stiff polymer walls to prevent early shear failure of sand and improve layer load- bearing capacity. Customising a geocell for the designated layer involves selecting geocell sizes that can effectively confine pressure within a specific area of influence. The opening size of the geocell should be sufficiently small to contain the spreading stress. However, caution must be exercised to avoid excessive proximity between the cell walls, as this can lead to inadequate compaction of the infill material.

Since, there has not been explorations into modifying the construction practices and materials beyond what is mentioned in the guidelines. Therefore, there is the requirement of formulating a new construction process for the bedding layer of an ICBP. The geocell technology operates on the fundamental concept that plastic walls can effectively alleviate excessive stress and hinder horizontal movement of sand, resulting in a notable enhancement in the layer's stability. The technology has been adopted for lower layers of pavements, i.e., the base, sub-base, and subgrade. However, geocell stabilisation is uniquely suited to each layer of the pavement. In particular, the utilisation of geocell technology in a base, sub-base or subgrade is meticulously customised to suit the precise stress characteristic and layer conditions of the specified layer. Hence, the existing geocell technology cannot be used for stabilisation in the bedding layer due to the layer's smaller thickness and its distinct location within the pavement. For that reason, it is highly justified to thoroughly explore the potential implementation of geocell technology in the upper layer of the ICBP, specifically the crucial bedding layer.

1.3 Research objective

The objective of the research work is to investigate the influence of confining the bedding sand in ICBP using geocell made of polymeric material (HDPE). The study is also aiming to assess and compare the performance of ICBP, where blocks are placed on a confined bedding layer, as opposed to a conventional bedding layer adhering to the recommended sand gradation specified by IRC (Indian Roads Congress). Approaching the objective of the study is to focus on the following:

a. Evaluation of structural behaviour of precast concrete block pavement laid over a controlled bedding layer (gradation of sand) as specified in specifications with plate load test.
b. Evaluation of structural behaviour of precast concrete block pavement laid over confined bedding layer of different pocket sizes with plate load test.
c. Evaluation of elastic modulus of the ICBP.

1.4 Scope of the study

The scope of the study will address the following:

a. To highlight the functions of the thin bedding layer which is assumed to be a levelling and cushion layer, that it can also have structural influence on ICBP.
b. To implement stabilisation of bedding layer by geocell technology, which is design specific of the stresses and strains of the bedding layer of ICBP.
c. To demonstrate the varying geocell sizes influence on structural properties of the bedding layer.

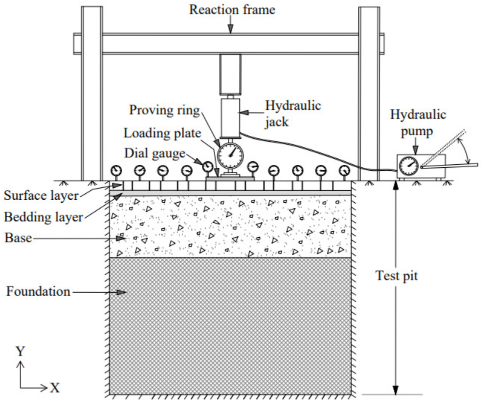

Figure 1.1: Schematic diagram of the test set-up

An experimental investigation on usage of the geocell technology in the bedding layer of a concrete block pavement is conducted in the laboratory. The sections are prepared in a test pit, a 2.5 m × 2.5 m × 2.5 m, and loading is through a 50 kN capacity reaction frame. Gradually the load is applied using a 100 kN hydraulic pump with a 1 kN graduation. To assess the structural response of the test sections, a non-repetitive static plate test is performed by gradually applying a maximum load of 40 kN. The maximum load, i.e., half the equivalent standard axle load of 80 kN is applied onto a rigid circular plate of 300 mm, of which the diameter size being an equivalent contact area of a dual wheel. Measuring the surface profile, plunger dial indicators are fixed at plate edge, 300 mm, 600 mm, 900 mm, and 1200 mm on either side of the loading center (i.e., center of plate). The illustration of the loading set-up is shown in **Figure 1.1**. It should be noted here, the label "Foundation" includes the embankment and subgrade.

Using locally available materials, the pavement sections comprise of embankment, subgrade, base, bedding layer and block-sand surface layer. As illustrated in **Figure 1.2**, support layer and surface layer are prepared following specifications, while the bedding layer prepared with and without geocells. The geocell considered in the study is a 0.32 mm thick HDPE sheet, that is trimmed to 40 mm strips. The strips are manually heat sealed in the laboratory to opening sizes, such that maximum geocell opening is guided by the observation where the pressure under the bedding layer completely dissipated at distances 250-350 mm (Panda 2006). The minimum cell opening is decided by the ease to seal as well as sufficient compaction of infill material.

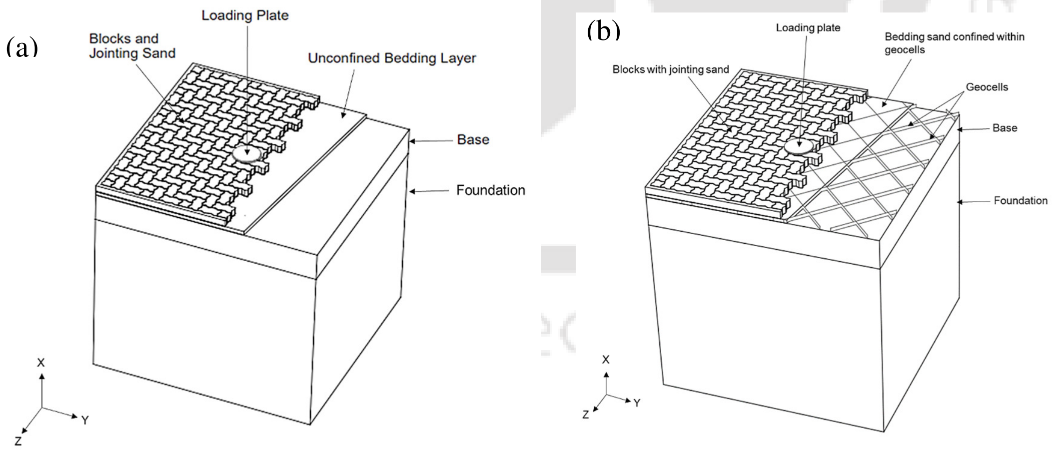

Figure 1.2: Pavement section with (a) unconfined and (b) confined bedding layer

The structural analysis is conducted on each section to investigate the pavement behavior due to the influence of confinement and compare it with the conventional construction. The analysis is facilitated by the FEM. To show the improvement of using confinement, and the influence of the cell openings on the structural capacity of the bedding layer, calculation of modulus of improvement factor (MIF) is taken (Al-Qadi and Hughes 2000; Garcia and Neto 2021; Kief et al. 2015; Kief and Rajagopal 2008; Rajagopal et al. 2012; Saride et al. 2022). The MIF is calculated as the ratios of simulated elastic modulus of confined bedding layers to the elastic modulus of unconfined bedding sand.

While simulating the exact physical system of ICBP, one might encounter challenges such as computational complexity, meshing issues, boundary condition complexity, solver sensitivity and increased computational time. Therefore, to ease the computational challenges, micromechanical homogenisation is conducted, in which the complex surface layer consisting of blocks and jointing sand will be replaced by an equivalent homogenised layer.

1.5 Organisation of the report

The thesis is organised into seven chapters as mentioned below:

- **Chapter 1** is an introductory section, delineating the scope of the research field, emphasising the research issue, and outlining the objectives of the research.
- **Chapter 2** proffers an in-depth examination of relevant literature pertaining to the research.
- **Chapter 3** describes the materials employed, their properties, the testing procedures and standards adhered to, and elucidates the research methodology.
- **Chapter 4** presents the numerical analysis; its methodology and analysis conditions adopted for executing ICBP simulations.
- **Chapter 5** presents the results attained from experimental investigation, and numerical analysis of the ICBP layers to achieved the material properties and simulation simplification with homogenisation.
- **Chapter 6** concludes the findings from the present study and suggests recommendation to the existing construction procedures.
- **Chapter 7** delves into the discussion of the research's limitations, and prospects for future development.
- The list of publications from the dissertation work and bibliographic details are presented

Chapter 2. Literature Review

2.1 Introduction

This chapter entails a concise exploration of the fundamental principles governing the functionality of ICBP and the application of geocells in soil reinforcement, drawing from an extensive review of existing literature. Additionally, it briefly touches upon the adopted methodologies for the structural analysis of block pavements and geocell-reinforced soils. Furthermore, an introduction to the concept of homogenisation through micromechanics, which will be employed in the context of concrete block pavements, is also provided.

2.2 Review on performance of ICBP

In all environmental and physical conditions, the pavement should be able to perform satisfactorily during its service life. In order to function sufficiently, the pavement should be able to possess the following features:

a. Ability to achieve the level of pavement service, assessed through the pavement structural capacity to sustain cumulative traffic load.
b. Occurrence of wear and tear of the pavement should be minimal and not hinder the safe, smooth and comfortable ride.

Therefore, pavement design method is based on the following three principles (Rollings 1984):

a. The layers should possess sufficient strength to withstand traffic induced stresses
b. The layers should be compacted to the point where the design-assumed layer strength is attained and no densification with subsequent surface settling occurs under traffic.
c. Each layer's materials must adhere to physical standards that have been determined to be essential for appropriate long-term performance.

Concrete block pavement is adopted for urban and local roads where medium to light traffic is expected (Eisenmann and Leykauf 1988). Concrete block pavement has also been adopted in places where traffic speed is limited to 60 km/h (Beld and Duiven 1984; Di Mascio et al. 2019), such as container ports, parking spaces, fuel stations, service lanes, etc. Concrete block pavement has been a better option because conventional flexible pavement will invariably rut under the wheel trolling same path repetitively (Shafer 2006). For regular traffic, sand is used for the bedding layer, however, in locations that handle heavy vehicular loads, a cement treated base is recommended to handle excessive rutting (Eisenmann and Leykauf 1988; Shafer 2006).

The behaviour of the surface layer of a concrete block pavement is truly not similar to either conventional flexible pavement or rigid pavement. Flexible pavement deformation can be explained as a wave, its maximal is at loading area, and a rigid pavement undergoes slab action, while the surface constituents of the concrete block pavement lodge-into, interlock and undergo progressive stiffening over time.

Actual behaviour of this pavement to repetitions of loaded wheels over time presses the blocks underneath lodging them into the sand beds, and by rotating and displacing about each other blocks interlock is mobilised. The movement minimises with time due to stiffening of the sand layers (Houben and Jacobs 1988); this phenomenon observed is termed progressive stiffening. The decreasing measured deformation that occur with an increasing number of load repetitions are used to quantify progressive stiffening**.**

The use of Concrete Block Pavement (CBP) as a functional and visually appealing substitute for conventional pavement systems has grown significantly (Lin et al. 2016). But much like any other building technique, it might encounter structural difficulties and malfunctions which are ineluctable due to loading. The CBP failures are mainly categorised into two groups:

a. Functional failures including block cracking, spalling, chipping, abrasion wear, joint sand loss (Mori et al. 2000; Shackel et al. 1998).
b. Structural failures including, rutting, unequal settlement, elephant footprint, horizontal creep and ravelling (Shackel et al. 1998; Yasuhisa et al. 2006).

ICBP structures are vulnerable to several conditions that may lead to their structural failure. This might include problems with the existing base structure, insufficient drainage systems, exposure to high traffic volumes, and even the quality of the building materials utilised.

CBP is allowed in medium to light traffic highway stretches (Eisenmann and Leykauf 1988) as heavy loading causes earlier rutting may have been stressing the base over time (Shafer 2006) for which concrete treated base (CTB) is recommended (Eisenmann and Leykauf 1988) For heavily trafficked concrete block pavement, an admixture of lime or cement to the bedding material could be appropriate but with provision of a sufficient surface crossfall >2.5% (while for pavement with heavy static loading, in container terminals, crossfall upto 2.0% is admissible) along with provision of slotted sewers for surface drainage (Eisenmann and Leykauf 1988). In case of severe frost conditions, no-fines concrete can be used instead of CTB (Eisenmann and Leykauf 1988).

2.2.1 Factors influencing performance

The manner in which the CBP responds to external loading is by activating interlocking among individual blocks, facilitating dispersion of the load horizontally across the surface and vertically into the underlying foundation. Three distinct types of interlocking mechanisms are identified (Füssl et al. 2016; Mampearachchi and Gunarathna 2010; Panda and Ghosh 2002a; Soutsos et al. 2011):

a. *Vertical Interlock*: The interconnecting gap in between the blocks is filled in with sand that not only bridge for load transfer across the surface but also facilitates interlocking by frictional forces.
b. *Horizontal Interlock*: Corrugated shapes and certain paving pattern provides horizontal interlock, resisting lateral movement during vehicle braking, acceleration or turning.
c. *Rotational Interlock*: Wheel loads eccentrically about the blocks, causing them to rotate. However, deformation of CBP surface in such moments undergoes the arching action, in which, when a set of blocks are loaded, they rotate and push the adjacent blocks, while hinging about each other. However, their movement is resisted by the adjacent blocks or edge restraint. As load increases, greater number of adjacent blocks participate in the resistance, causing wedging/ interlock over a larger area.

The events of block interlocking and progressive stiffening is influence by the hinging effect and frictional resistance influenced by block arrangement, block shape and size, joint width, edge restraint, bedding layer thickness and composition, and support strength. These factors influence the expanse and depth of surface deformation bowl. Smaller deformation is associated with higher load transfer efficiency across the surface and smaller block rotation (Panda 2006).

2.2.1.1 Block strength, geometry, dimensions and laying pattern

The greater side area of thicker blocks may have provided greater contact surface for vertical and rotational interlock. By increasing the block thickness, stress detected below the surface layer decreases (Hassani and Jamshidi 2006) and this is due to greater load transfer efficiency (Noda et al. 2009). However, block thickness has no influence on surface deformation when joint sand is absent (Panda and Pani 2020a). On the basis of block shapes and their arrangements, concrete block pavement can sometimes be called ICBP. According to IRC (2004) the shape of blocks can be grouped into three categories:

Category A: Dentated units are designed to interlock along all four sides, and keyed onto each other when placed on a surface, effectively deter any joint widening. Typically, arranging these blocks in a herringbone bond pattern enhances interlocking to the maximum compared to other combination of block shapes and patterns.

Category B: These blocks are dentated on only two sides and their interlocking effect is facilitated by arrangement. In most cases, these blocks are limited to being laid exclusively in a stretcher bond, although there may be occasional exceptions.

Category C: These blocks have no dentation on any side and its interlocking only depends upon its dimensional accuracy. These blocks can be arranged in all patterns.

The least efficient block shape and pattern is the rectangular block and stretcher bond (Yasuhisa et al. 2006). Arranging the blocks in a linear stack, rather than in a staggered stretcher pattern, results in the lowest efficiency when it comes to resistance against deformation. (Mampearachchi and Gunarathna 2010). Blocks of corrugated shapes and laid in herringbone pattern offers the most efficient interlocking effects during vertical loading or breaking action. While blocks in stretcher pattern slides smoothly along the bedding while in herring bone pattern, they rotate about each other, giving an uneven horizontal movement (Mampearachchi and Gunarathna 2010). The decrease of deflection of stretcher pattern arranged Category A blocks with Category B and Category C blocks are 21 % and 41 % respectively (Arjun Siva Rathan et al. 2022a). Thinner block exhibits a more pronounced improvement in its ability to resist surface deformation simply by arranging the blocks in a herringbone pattern (Panda and Pani 2020a). Block should also possess the strength to handle the traffic loads without breakage (Yaginuma and Kasahara 2006).

2.2.1.2 Joints

Efficiency of load transfer through interlocking effects occurs through the joints (Noda et al. 2009). The inclusion of jointing sand within the pavement resulted in a significant decrease in the maximum central deflection, with reductions of 30.35%, 49.35%, and 67.3% observed for block thicknesses of 80 mm, 100 mm, and 120 mm, respectively, when compared to instances where jointing sand was not utilised (Panda and Pani 2020a). The efficiency of load transfer increases when using narrower joints, as the wider spaces filled with granular material can hinder joint performance. This is because load transfer efficiency relies not only on the compressive force along the joint and the frictional interaction at the interface but also on the shearing of sand (Noda et al. 2009). The gap should accommodate the sand travelling during filling and compaction. Therefore, the joint width is recommended not too narrow and wide, but in between 2-4 mm (IRC 2004, 2018a; Panda and Ghosh 2002a; Yasuhisa et al. 2006). However, even at 18 service years, a bus station CBP encounter block breakage more than the maintenance standard value of 20 %, even when the joint width was narrow than 4 mm (Omoto et al. 2009). Besides, too narrow joints may cause the blocks to resist surface layer deformation by knocking against each other, causing earlier breakage, chipping and spalling.

In any pattern of block arrangement, strong interlocking will not be generated when joint filling is not densely compacted (Lin et al. 2021). Loss of jointing sand leads to reduced load transfer and blocks shifting, highly stressing on the separated blocks and also leads to collision and breakage of blocks (Yasuhisa et al. 2006).

2.2.1.3 Bedding Layer

The primary role of the bedding layer is to ensure a levelled surface for the block layer and to alleviate the concentrated stress (Lin et al. 2021). Presence of a bedding layer immediately disperses the stresses under the blocks to about 60% the contact pressure (Hassani and Jamshidi 2006)

Improper load surface dispersion only transfers greater stress onto the bedding layer, causing consolidation and pulverisation of bedding sand and blocks shifting (Yasuhisa et al. 2006). For bedding layer and joints construction, the sands are recommended to sound and free from deleterious elements. Sand in the bedding layer should also possess high load transfer, efficient in particle interlocking, and undergoes minimal pulverisation (IRC 2004, 2018a; Yaginuma and Kasahara 2006). The sands should not be prone to pulverisation and the sand sizes should be sufficient to provide particle interlocking (Yasuhisa et al. 2006). The latter sand property can be achieved by limiting sand passing 0.6 mm and 0.075 mm sieves, and having sufficient hardness (Mori et al. 2000; Omoto et al. 2009).

Insufficient bedding compaction during construction can results to a high degree of rutting within the first few months of service life (Yaginuma and Kasahara 2006). Rutting that occur due to pulverisation of sand occurs later in time, and it is intensified when seeped water bond the particles together (Omoto et al. 2006). However, the reason for early rutting is attributed due to improper compaction or unexpected heavy loading that cause the bedding sand to rearrange and may undergo shear failure (Houben and Jacobs 1988). The suggested compaction level involves a loose layer of sand with a specified thickness, which is to be compacted to achieve a desired level, without specifying the target density (ICPI 2007; IRC 2018a). As the layer is thicker, the shear strength becomes smaller, probably due to insufficient compaction to uniformly densify throughout the sand depth (Panda and Ghosh 2002a), eventually affecting the bearing capacity of a soil. Therefore, it is common to associate thicker bedding layer with earlier failure. Some researchers have recommended bedding thickness below 20-40 mm (Arjun Siva Rathan et al. 2022a; Chua et al. 2000; Eisenmann and Leykauf 1988; Gunatilake and Mampearachchi 2014, 2019; Houben and Jacobs 1988; ICPI 2007; IRC 2004, 2018a; Lin et al. 2016; Di Mascio et al. 2019; Morrish 1980; Panda 2006; Rada et al. 1992; Rollings 1986; Soutsos et al. 2011; Taheri et al. 2021). Omoto et al. (2009) observed a bedding thickness within 30 mm is prone to consolidation deformation under heavy load repetitions, however, thickness of the sound section is just a little thicker than 20 mm. While Panda and Ghosh (2002) shows pavement response nearly the same for 20-50 mm loose thickness of bedding sand, but they observed the optimum loose thickness of 50 mm is most effective thickness in terms of achieving level of compaction and shear failure resistance. Thickness greater than 50 mm only absorbs significant amount of the compaction energy in wedging the sand into the joints, thereby transferring less into the underlying bedding sand.

2.2.1.4 Support Layer and edge restraints

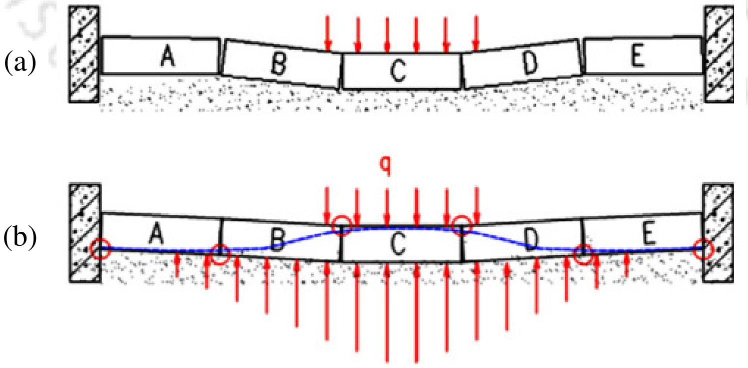

Figure 2.1: (a) Deformed block pavement (b) Hinge mechanism for load transfer (Soutsos et al. 2011)

As the load increases, CBP begins to create interlocks, causing the blocks to reach a locked state with the formation of hinges (Mampearachchi and Gunarathna 2010). If the edge restraints are positioned closer to the point of loading, the hinges will form more rapidly across the expanse of pavement, and with greater strength resulting in improved load distribution (Mampearachchi and Gunarathna 2010; Panda and Ghosh 2002a). The deflection is solely influenced by the support and block interlocking in the absence of edge restraint, since the blocks can push each other without greater resistance. When surface edges are free, Panda and Ghosh (2002) observed a deflection of 1.6 times to surfaces with edge restraint placed at 775 mm distance. For a Category A blocks arranged in stretcher pattern, difference in deflection is negligible beyond 400 mm from loading centre (Arjun Siva Rathan et al. 2022a).

A stiffer foundation and/or a base/sub-base supports the surface layer from excessive deformation (Mampearachchi and Gunarathna 2010; Panda and Pani 2020a). A 450 mm base supports the ICBP to a deflection of 0.55 times and reduces about 80 % of stress than that of a 150 mm base (Arjun Siva Rathan et al. 2022a). Compared to a 150 mm thick sub-base, a concrete block pavement with a 300 mm and a 450 mm sub-base reduces deflection by 30 % and 10 % respectively (Panda and Pani 2020b). Hinge mechanism is influenced by the simultaneous role of block features, edge restraints location and support strength, in which a concrete block laid on stiffer support stiffens at greater load due to earlier load spreading capacity commenced by closer edge restraints (Mampearachchi and Gunarathna 2010).

2.3 Review on stabilisation methods

According to engineering definition, soil is a natural aggregate obtained from the earth's crust, and constituting of mineral grains with/ without organic content. Soil is broadly classified into coarse and fine-grained. Additionally, plasticity properties, organic content, gradation, coarse portion and fines contents further specify the soil (BIS 1970). Soil, either situated in-situ or relocated, is the fundamental component for foundation design, with the primary objective of ensuring the soil do not excessively deform when strained and can satisfactorily withstand applied stress without undergoing failure. Consequently, the structural integrity relies heavily on the bearing capacity of the foundation soil, which pertains to the soil's capability to sustain external loads without experiencing shear failure. In certain instances, where weak soils are inevitably encountered, the necessity arises exploring solution to strengthening or replacing the material, with strengthening being a viable alternative.

2.3.1 Geocell Stabilisation

Failure of soils that are subjected to bearing load occurs as a shear failure of the soil supporting the structure. Shear failure can occur in three modes, i.e., are general shear failure, local shear failure and punching shear failure. The characteristics of each failure mode is the pattern of the failure region, which is governed by the ground condition and types of soil.

To improve the stability of the soil, enhancement of the engineering properties of soil is carried by biological, chemical and mechanical stabilisation. Biological soil stabilisation is achieved through afforestation and reforestation and its main purpose is in erosion management. Chemical stabilisation in solid or liquid forms and generally called soil binders, provides solutions to regions where vegetation cannot be established. In pavement, these soil palliatives improve the mechanical strength, shrink swell properties of expansive soils, acts as drying agent to reduce soil moisture contents promoting compaction. Improvement methods can also require no chemical change to the soil properties, achieved by compaction, addition of graded materials, or reinforcement.

Reinforcement improves the soil strength in a way it delays soil failure wherein the geotextiles and fibrous reinforcement hold the soil, deferring particles movement. Fibrous reinforcement by infusing natural or synthetic fibres that their stiffer strength improves the deformation of the composite. Fibrous reinforcement is limited with concerns related to enzymatic hydrolysis of the organic content of natural fibres (Béguin and Aubert 1994; Patel and Singh 2023; Sapkota 2022), non- eco-friendliness of synthetic fibres (Patel and Singh 2023), and has been limited to study at research level (Liu et al. 2021; Öncü and Bilsel 2017; Sujatha et al. 2021; Zhao et al. 2020).

Geosynthetic are commonly used in pavement layer strengthening and are classified based on their polymeric made and spatial characteristics, in one-dimensional, two- dimensional, and three-dimensional (IRC 2019). The basic functions performed by geotextile are as separation, filtration, reinforcement, drainage, moisture barrier, and for erosion control. While majority of the purposes is to preserve the original form of the material as intended, reinforcement imparts mechanical strength manifested as altered geotextile-soil composite stress-strain behaviour. Delayed deformation means improvement of mechanical properties of the soil and enhance the load-carrying capacity of pavements under repeated traffic (Thakur et al. 2012). Extensive research has been carried in implementation of geotextile in the subgrade and base stabilisation, and reduction of aggregate layer thickness in paved and unpaved roads (Haeri et al. 2000; Hausmann 1987; Khan et al. 2023; Meena et al. 2013; Önal et al. 2023; Saha and Kabir 1988; Yang et al. 2012, 2013).

2.3.2 Influence of confinement

Geotextile reinforcement improves the soil strength by corresponding to increase in the stiffness of the soil and resistance to flexural deformation (Pokharel et al. 2010; Yang et al. 2010). Acting as a semi-rigid slab or the "beam effect", about half of the vertical stress is diffused throughout the layer expanse rather than directly transferring it to the lower layer (Kief et al. 2011; Kief and Rajagopal 2008). This stress dispersion effect of the composite layer absolves the superstructure punching through.

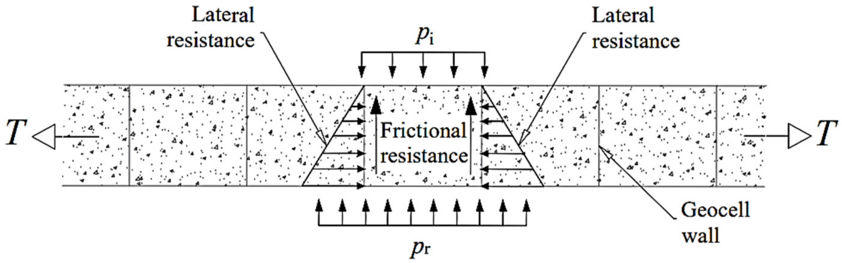

Figure 2.2: Confinement effect (Pancar and Akpinar 2016; Zhang et al. 2010)

Confinement effect encountered upon loading is contributed by three factors (refer **Figure 2.2**): lateral constraint along the perimeter walls (Bathurst and Karpurapu 1993; Han et al. 2008; Kief and Rajagopal 2008), tensioned membrane effect (Mindiastiwi et al. 2021; Rajagopal et al. 1999) and interface frictional resistance between the infill particles and cell walls (Han et al. 2008). The initial resistance to deformation initiates by the infill and geomaterial interaction in form of frictional resistance and particle interlocking, which at greater strains, the effect of confinement is more pronounced (Al-Qadi and Hughes 2000; Bathurst and Karpurapu 1993; Han et al. 2008; Pancar and Akpinar 2016). Lateral constraint occurring within the reinforced layer depth, results from the hoop strength of the geocell, upon encountering active and passive earth pressure (Madhavi Latha et al. 2006; Pokharel et al. 2010, 2018).

The two prominent reinforcement effect of planar reinforcement are lateral restraint and frictional resistance (Hufenus et al. 2006). Whereas, in geocell reinforcement, initial action of the confinement is suppressing infill dilatancy, and at large strains, the stiff circumferential expansion of geocell walls maintains the infill state while increasing the resistance to vertical deformation (Bathurst and Karpurapu 1993; Thakur et al. 2012). In other words, stiffness of geocell-reinforced layer is also contributed by hoop strength due to tensioned membrane effect of the geocell walls (Zhou and Wen 2008). The hoop stress on each wall not only encounters active earth pressure from its own infill but passive pressure from adjacent cells, in which the wall bottom experiences greater stress than the upper side (Han et al. 2008). The beam effect is more pronounced in layer with weak supporting layers (Baadiga et al. 2021; Saride et al. 2022) because the resistance to flexural deformation of the geocell bed is prominent when slab is allowed to stretch to its maximal, when hoop forces are mobilised (Giroud and Han 2004; Han et al. 2008; Tang and Yang 2013). However, at its own limitation where at greater loading stage, reinforcement is entirely dependent on the geomaterial make and seam strength (Bathurst and Karpurapu 1993).

2.3.3 Factors influencing geocell reinforcement

The concept of lateral cellular confinement was initially conceived and experimentally examined by the U.S. Army Corps of Engineers during the 1970s with the aim of enhancing the load-bearing capabilities of poorly graded sand (Webster 1981). The greater resistance to the flexural deflection depends upon type of infill material, aspect ratio (i.e., cell height to cell length/diameter ratio), geomaterial type and infill material condition (Pokharel et al., 2010; Rajagopal et al., 1999; Saride et al., 2022; Tang & Yang, 2013). Geotextile can be sewn from many polymeric sheets of high density polyethylene, polypropylene or alloy material (IRC 2019), in which stiffer material possesses greater membrane strength (Rajagopal et al. 1999). However, the seams within the geocell mat may be the weakest lines for rupture at high tensile force (Bathurst and Karpurapu 1993).

The initial resistance to deformation commences through the interaction between infill material and geomaterial, manifesting as frictional resistance and the interlocking of particles (Al-Qadi & Hughes, 2000; Bathurst & Karpurapu, 1993; Han et al., 2008; Pancar & Akpinar, 2016). Irrespective of aspect ratios, geocell sizes and its material type, and infill material density, the flexural deformation is similar at low load values which only becomes more prominent when the geocell reinforcements encounters greater load or experiencing larger deformation (Tang and Yang 2013). But then again, geocell efficiency also depends upon the infill material in which saturated and weaker infill benefits more (Jalili and Kabiri 2019). Compare to sandy infill, confinement is satisfactory to reinforce clayey soil (Madhavi Latha et al. 2006) but mitigating swelling capacity caused by its active clay content may not be resolved. Whereas, confinement of granular or sandy material will add resisting force beside bearing capacity that is contributed by particle interlocking. Fines in clayey material can impart additional strength in term of cohesion (Pokharel et al. 2010). Particles interaction within the infill and with the geocell walls build up the frictional resistance to settlement. Resistance to deformation, is contributed by the prominence of aggregate particle interlocking with finer particle and greater density of infill material observed to be desirable (Bathurst & Karpurapu, 1993; Jalili & Kabiri, 2019; O. Kief & Rajagopal, 2008; Pokharel et al., 2010; Sanat K. Pokharel et al., 2018; Tang & Yang, 2013). As dense as material can possibly is better is the particle interlocking, which can be achieved by direct compacting the layer. However, greater than 90% infill density cannot be achieved with geocell aspect ratio smaller than 1.0 (Jalili and Kabiri 2019; Pokharel et al. 2010; Yang et al. 2010).

Geocell size being a factor is considered in terms of opening sizes and height, which is oftentimes taken as aspect ratio. The greater aspect ratio, in terms of cell height reflects the greater length and cell area for membrane effect and frictional resistance effect. A single 100 mm high geocell performs better than two geocell of height 75 mm each, stack one on the other (Pokharel et al., 2010). Under a cyclic loading, Thakur et al. (2012) observed geocell tensioned membrane effect mobilising in which vertical stress reduces at the permanent deformations of 48, 52 and 22 mm for corresponding 0.15, 0.23 and 0.30 m thick reinforced base sections. The other way of explaining greater aspect ratio is term of cell opening sizes, in which small cell opening means greater density of geocell walls improves the effective resistance per unit area of the reinforced layer encountering incoming stress is greater (Dash et al., 2007; Pokharel et al., 2010; Rajagopal et al., 1999). Increment of aspect ratio for a triaxial test volume, the improvement to shear strength, due to additional strength imparted in terms of apparent cohesion escalates (Bathurst and Karpurapu 1993; Rajagopal et al. 1999). Even geocell opening sizes are taken with respect to maximum aggregate size (Jalili and Kabiri 2019; Kabiri Kouchaksaraei and Bagherzadeh Khalkhali 2020), however, density of material flow into each cell for achieving higher density is more essential (Jalili and Kabiri 2019). However, for large aggregates, the increment of aspect ratio may not support an improvement (Bathurst and Karpurapu 1993).

Stiffness improvement due to inclusion of a geomaterial, is evaluated by the Modulus Improvement Factor (MIF) value. MIF accounts for the effects of reinforcement in enhancing modulus of a layer, and calculated as the ratio of elastic modulus of reinforced layer to the unreinforced layer (Saride et al. 2022). MIF values for a planar reinforcement within a base layer overlying a sub-base ranges just greater than 1.0 and can reach 5.0 (Baadiga et al. 2021; Goud et al. 2022; Saride et al. 2022) depending upon its reinforcement-depth ratio (Baadiga et al. 2021; Saride et al. 2022; Shin et al. 2002). MIF values of geocell reinforced base ranges 1.4 to 5.4 (Kief & Rajagopal, 2008; Pokharel et al., 2010; Saride et al., 2022; Tang & Yang, 2013). Geocell reinforcing the sub-base is has MIF of less than 3.0 (Kief et al. 2011). On an average, for any underlying supporting material, geocell improvement is greater than a planar reinforcement (Saride et al. 2022) in which through the beam effect, geocell-reinforced section reduces the transfer of stress into the lower layer (Kief et al. 2011; Kief and Rajagopal 2008). Even though it is significant for their integration into pavement designs. the MIF values pertaining to geogrids and geocell reinforced base layers are currently in the developmental phase (Saride et al. 2022).

2.3.4 Influence of location of 3D reinforcement

The stress distribution through the pavement depth is essential as it governs how the number of axle passes and geotextile properties impact the necessary thickness of the pavement layers. Vehicular stress gets dispersed wider with depth, with the upper layer experiencing high stresses. Closer to the surface, the granular material encounters significant stresses, leading to greater deformation. Therefore, the rationale behind using superior materials for the upper layers lies in their ability to withstand higher stress levels while minimising deformation.

The effectiveness of the 3D reinforcement, in terms of lateral confinement, tensioned-membrane effect and stress distribution depends on the level of stress it intercepted. The bearing capacity elevation is contributed by two aspects, the soil interaction within itself and the geocell, and membrane effect, with little to no direct effect of lateral resistance (Pancar and Akpinar 2016; Zhang et al. 2010). Rajagopal et al. (1999) and Bathurst & Karpurapu (1993) observed in triaxial testing of cohesionless material the inert property of sand (ϕ) did not change while only shear strength is improved due to the membrane effect, indicating the internal friction within the soil do not differ. Mitigating stress is expected to be the highest under the loaded footing (Dash et al. 2007) and widely disperses beyond that loading region (Pokharel et al., 2010). Consequently, in addition to factors like geometric attributes of geocell, types and condition of infill material, and nature of applied load, the positioning of the geocell-reinforced layer within the pavement structure also plays a significant role in influencing its performance (Dash et al. 2007; Saride et al. 2022; Tang and Yang 2013). Geocell has been widely adopted in reinforcing materials in road sections, such the subgrade, base and sub-base of road pavement (Deshmukh et al. 2022; Gao et al. 2023; Gedela and Karpurapu 2021; Luo et al. 2022; Mamatha and Dinesh 2019; Sheikh et al. 2021) and ballast and sub-ballast embankment of railroad (Arslan et al. 2022; Banerjee et al. 2023; Indraratna et al. 2006, 2010; Leshchinsky and Ling 2013).

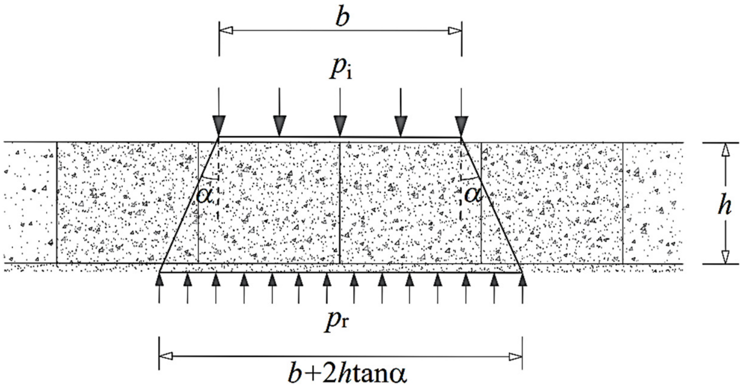

Figure 2.3: Stress dispersion (Pancar and Akpinar 2016; Zhang et al. 2010)

The stress dispersion effect, measured as the reduction of transmitted stress onto the lower layer due to the geocell ability to redistributes the footing load per unit area to a wider area, is navigated by the three confinement functions (Pancar and Akpinar 2016; Saride et al. 2009; Zhang et al. 2010). As shown in **Figure 2.3**, the angle of stress dispersion (*α*) when a load is applied at reinforced layer surface of width (*b*), and depth (*h*), is approximated by a relation given in Equation (**2.1**) (Pancar and Akpinar 2016; Thakur et al. 2012; Zhang et al. 2010).

$$\alpha = \tan^{-1}\left(\frac{\Delta b}{2h}\right) \tag{2.1}$$

Stress under the reinforced layer decreases from p_i to p_r, where p_i is intercepted stress on the geocell mat and dispersed stress respectively. Value of dispersed stress under the geocell is calculated by Equation (**2.2**) (Zhang et al. 2010).

$$p_r = \left(\frac{b + 2h\tan\alpha}{b}\right) p_i \tag{2.2}$$

The bearing capacity increment due to the stress dispersion effect (Δp_1) of reinforced layer is calculated as Equation (**2.3**)

$$\Delta p_1 = p_\mathrm{r} - p_\mathrm{i} = \left(\frac{2h\tan\alpha}{b}\right)p_\mathrm{i} \tag{2.3}$$

As deformation escalates, the proportion of the increase in bearing capacity, attributed to the membrane effect of geocell reinforcement, grows until the reinforcement reaches a point of failure (Zhang et al. 2010). The bearing capacity increment due to membrane effect (Δp_2) is taken as the tensile force acting along the geocell mat. As seen in **Figure 2.4**, the uniformly distributed load on a surface of width, b subjected the geocell bed to a tensile force, T.

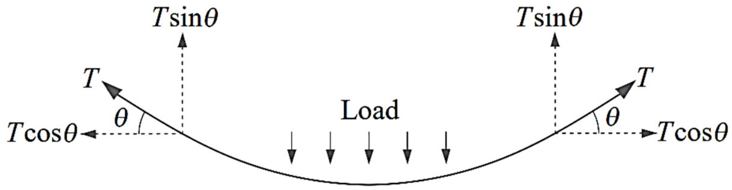

Figure 2.4: Membrane effect (Pancar and Akpinar 2016; Zhang et al. 2010)

The tensile force calculated by Equation (**2.4**), is approximated throughout the geocell mat height and singly dependent upon the geomaterial stiffness and its strain value.

$$\Delta p_2 = \frac{2T\sin\theta}{b} \tag{2.4}$$

where T is tensile force of geocell mat, when the geocell mat is inclined at angle θ, to the horizontal direction. Given in Equation (**2.5**), tensile force is calculated as a relation of tensile modulus of the geocell material ($\mathrm{E_g}$), tensile strain of the geocell mat (ε), and height of geocell ($\mathrm{h_g}$).

$$T = \mathrm{E_g}\varepsilon h_\mathrm{g} \tag{2.5}$$

The increase in bearing capacity resulting from the reinforcement provided by the geocell is closely tied to factors like the intercepted stress and the type of geomaterial involved. Since the stress distributed within the pavement depth is spread over a larger area, the specific placement of the geocell reinforcement determines the extent of the confinement effect mobilised. Consequently, a geocell designed for a particular pavement layer should adequately function without disintegrating.

2.4 Review on structural analysis of ICBP

Concrete block pavement differs from the conventional pavements by virtue of its surface layer. Comprising of discrete and discontinuous units, this layer responds differently to the external loads. These units are arranged in certain pattern with their gap in between being filled with jointing sand. While it is the block layer that majorly disperse the vertical stress, and, its behaviour is influenced by the units' thicknesses, length and width, composition and laying pattern. The surface components are supported on a levelled layer of bedding sand. The substructure, beyond the bedding is the same as that of a conventional flexible pavement.

2.4.1 Approaches to structural analysis of pavement composites

ICBP differs from conventional pavements of rigid and flexible type in its deformation pattern of the surface. The layers from bedding layer and underneath have quadrated volume which can be assumed to consist of homogeneous and uniform material. However, the surface consists of two materials, the concrete blocks and jointing sand, that differs in material types. The concrete blocks feature edges oriented in multiple directions.

The deformation of the surface and stress distribution to underlying layer is a result of the articulation of these stiff concrete blocks about their joints. Complexity of surface layer varies due to the shape of a block unit and arrangement of the blocks. The irregular shapes and arrangement of the surface components rather complicates the simulation of ICBP, making the designer choosing two ways of modelling ICBP layers, one is the equivalent composite approach and the other is three-dimensional (3D) modelling the layers. Similarly, geocell reinforced beds can be represented by ECA or actual geometry.

2.4.2 Equivalent composite approach (ECA)

Composite materials find applications in industries such as aerospace, sports equipment, infrastructure, transportation, and marine sectors. Key attributes of composites that hold significant importance include their strength, ease of fabrication, reparability, long-term durability, cost-effectiveness, and their ability to withstand fatigue and resist corrosion. Equivalent composite approach (ECA) in mechanical systems is a concept of replicating composites into a homogeneous material which is equivalent in terms of effective modulus (Hedge and Sitharam 2015a). There are two ways of accomplishing ECA, firstly, the composites equivalent properties are considered to be isotropic and homogeneous or orthotropic and homogeneous (Choi and Thangjitham 1991; Maji et al. 2016; Yang et al. 2010) throughout the macroscale volume, and secondly, ECA is employed by means of micromechanics. The composite material behaviour according to the earlier approach is presumed to be homogeneous, in which the constituents influence is detected as averaged apparent macroscopic properties of the composite materials. The latter method aims at converting the heterogeneous materials, considering the constituent characteristic attributes and tailoring effective properties, estimating the average responses of a small volume of the composites and its counter homogenised part to create isotropic, orthotropic or anisotropic materials as an equivalent homogenised material.

ECA is widely studied in applications for aircrafts, automotive, biomedical, fabrication, radiation environments, spacecraft, wind turbines, smart material technology, etc. Limited homogenisation analysis is implemented in pavement engineering, of which pavement composites consists of a strong material embedded in the volume along with a weaker material, such that the stiffer inclusion enhances the overall layer stiffness. ECA is implemented in geocell-reinforced pavement layers and surface layers of ICBP. Commonly adopted ECA is the heterogeneous material is presumed homogeneous by taken average properties apparently at macroscopic level. The geocell-soil composite is treated as a soil layer of improved strength and stiffness values and ICBP surface layer in combination with bedding layer is one stiff and elastic layer.

2.4.2.1 ECA of geocell reinforced layer

Simply, the geocell reinforced layer is considered as a homogeneous layer, in which the response calculated and collected is the equivalent response of the layer. In field, equivalent response is collected as equivalent bearing capacity and surface deformation from static plate load test (Banerjee et al. 2023; Han et al. 2010; Hedge and Sitharam 2015a; Madhavi Latha et al. 2008; Mhaiskar and Mandal 1996; Pokharel et al. 2018), surface deformation from cyclic plate load test (Jayanthi et al. 2022; Önal et al. 2023) or deflection during impact test (Deshmukh et al. 2021; Krishna and Madhavi Latha 2023; Luo et al. 2022; Saride et al. 2022).

The reinforced layer can be replicated as a uniform and homogeneous layer upon verification with the field responses in which improved elastic modulus can be back-calculated using the Boussinesq's elastic half-space theory (Deshmukh et al. 2021; Garcia and Neto 2021; Saride et al. 2022). Mhaiskar and Mandal (1996) modelled the geocell filled sand as an isotropic, elastic-perfectly plastic material in which yield condition follows Drucker Prager criterion. Most commonly, the equivalent layer is assumed as the composite layer possessing an improved cohesive strength and stiffness, and the layer yield condition is designed following the Mohr-Coulomb criterion or Drucker-Prager criterion (Hegde & Sitharam, 2013; 2015a; Madhavi Latha et al., 2008; Madhavi Latha & Somwanshi, 2009; Mhaiskar & Mandal, 1996; Yang et al., 2010). Henkel and Gilbert (1952), Bathurst and Karpurapu (1993), Rajagopal et al. (1999) and Madhavi Latha et al. (2008) proposed an equivalent composite model for sand enclosed within single and multiple geocells made of different geosynthetics based on the equivalent properties achieved from triaxial tests.

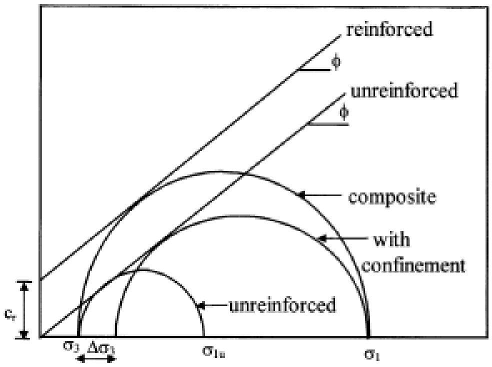

Figure 2.5: Mohr circles for reinforced and unreinforced soil (Rajagopal et al. 1999).

The influence of confinement within the granular layer can also be simply regarded as an enhanced strength of equivalent soil, in form of equivalent cohesion/ apparent cohesive strength (c_r) (Bathurst and Karpurapu 1993; Rajagopal et al. 1999). **Figure 2.5** demonstrates the Mohr circles for the reinforced and unreinforced soils in which, the relationship between induced cohesion (c_r) and additional confining stress ($\Delta\sigma_3$) can be visualised. The ultimate stress (σ_1^{ult}) that can be applied onto confined soil volume according to Equation (**2.6**) (Madhavi Latha et al. 2006, 2008; Rajagopal et al. 1999).

$$\sigma_1^{\text{ult}} = \frac{1+\sin\phi}{1-\sin\phi}\sigma_3 + 2c_r\sqrt{\frac{1+\sin\phi}{1-\sin\phi}} = K_p\sigma_3 + 2c_r\sqrt{K_p} \qquad \textbf{(2.6)}$$

where, ϕ is angle of internal friction, K_p is coefficient of passive earth pressure, and σ_3 is minor principal stress/ confining pressure. Here, apparent cohesive strength is calculated by Equation (**2.7**).

$$c_{\mathrm{r}} = \frac{\Delta\sigma_3}{2}\sqrt{K_{\mathrm{p}}} \tag{2.7}$$

And, increase in confining stress due to membrane stress in geocell wall is described by Equation (**2.8**).

$$\Delta\sigma_3 = \frac{2M}{D}\left[\frac{1-\sqrt{1-\varepsilon}}{1-\varepsilon}\right] \tag{2.8}$$

where,

D = initial diameter of the sample

M = modulus of the geotextile measured from tensile test of geomaterial. This value is approximated proportionally to the sample strain for each membrane.

For geocell confinement effect due to membrane stresses, the compression load, P at any axial strain, ε on the test specimen is given in Equation (**2.9**).

$$P = (\sigma_1 - \sigma_3)A_\varepsilon + \pi DM\varepsilon \quad \text{(Henkel and Gilbert 1952)} \tag{2.9}$$

where, $(\sigma_1 - \sigma_3)$ = deviator stress in the specimen

σ_1 = major principal stress

$A_\varepsilon = \frac{A_o}{1-\varepsilon}$ = corrected area of the sample at strain ε when original specimen with area A_o is assumed to deform as a right cylinder.

$$\text{The measured compression stress} = (\sigma_1 - \sigma_3) + \frac{\pi DM\varepsilon(1-\varepsilon)}{A_o} \tag{2.10}$$

The right side second term of Equation (**2.10**) indicates the membrane correction, of which Henkel & Gilbert, (1952) observed it to be roughly in agreement with the membrane tension value derived from hoop stress theory (given in Equation (**2.12**)).

Equation (**2.6**) can reasonably estimate collapse loads well for slope stability analysis of embankment with surcharges resting on a geocell reinforced foundation (Madhavi Latha et al. 2006). Although, the implementation of an enhanced confinement model gives a reasonable estimate, however, still under-predict frictional resistance between infill and the geocell wall material and stiffness increment of the composite due to interaction among multiple interconnected geocells. The apparent cohesion value is only valid for single cell confinement, and changes in magnitude when interconnected cells are present (Hegde & Sitharam, 2013). Through numerical simulations, Rajagopal et al. (1999) achieved interpreted c_r value improves 36 – 71% with increase in number of interconnected cells. Therefore, for the interconnected geocells, derived cohesive strength is corrected as a relation with total area and effective soil area encased within the geocell. Corrected cohesive strength of the geocell mat ($\boldsymbol{c}_{r_{\text{corrected}}}$) is calculated by Equation (**2.11**) (Rajagopal et al. 1999)

$$c_{r_{\text{corrected}}} = c_r \times \frac{\text{Area of soil confined in geocell}}{\text{Total area}} \qquad \textbf{(2.11)}$$

Another property of the composite, i.e., the equivalent stiffness parameter (E_r) of multiple-celled, geocell-reinforced sand can be calibrated to relate to stiffness parameter of unreinforced soil (E_e) by an empirical relation shown in Equation (**2.12**) (Madhavi Latha 2000)

$$E_r = E_e + 200M^{0.16} \qquad \textbf{(2.12)}$$

The interaction equation, Equation (**2.12**) is derived from regression analysis on triaxial test results of single and multiple cells made of different geosynthetic. The interaction parameter values of 200 and 0.16 is valid for medium dense sand confined in cells, in which each is surrounded by more than four cells (Madhavi Latha et al. 2008). The stiffness parameter of unreinforced layer corresponds to the dimensionless modulus number of a hyperbolic model (Duncan and Chang 1970). The Young's modulus of reinforced sand when subjected to confining pressure is then expressed in Equation (**2.13**) (Madhavi Latha and Rajagopal 2007)

$$\mathrm{E}_g = 4(\sigma_3)^{0.7}\left(E_e + 200M^{0.16}\right) \qquad \textbf{(2.13)}$$

There are many other similar proposals of deriving the equivalent geocell reinforced properties of long term behavior (Janbu 1970; Yang et al. 2013; Yang and Han 2013) . The equivalent method to develop numerical model of geocell-reinforced soil formulates the Equations (**2.6**) to (**2.11**), for composite behavior at failure point, and the phenomenon of reaching the equivalent peak strength of the composite is not clearly explained. By Equation (**2.12**) and (**2.13**), the characteristic of the composite equivalent is considered consistent with unreinforced layer behavior.

2.4.2.2 ECA of concrete block pavement

The equivalent composite approach for concrete block pavements is two ways;

(i) an equivalent thickness of the conventional paving material and predict the stress under the paving blocks same as measured in experiments. Trafficking tests cater to development of the equivalent thickness of concrete block layer.

(ii) an equivalent modulus method, i.e., an effective or equivalent modulus of the elasticity is determined for the block and sand layer by converting the discrete composition of the composite to a continuous bed. The method is implemented for layered elastic theory application of the concrete block pavement.

Due to the easy availability of graphs, tables, and computer programmes for the study of linear elastic pavement, equivalent thickness technique is developed throughout the initial design stage (Eisenmann and Leykauf 1988; Molenaar et al. 1984; Rollings et al. 1992). Block pavements can also be replicated as flexible pavements that possess high strength, thus, design methods of ICBP have been developed based on approximation of the surface behaviour similar to a flexible pavement (Rollings 1986; Rollings et al. 1992). The US Army Corps of Engineers adopted the design of considering the concrete block surface and bedding layer as equivalent to 165 mm of conventional bituminous layer and base, and preparing design index at different traffic description (Rollings 1984). A pavement built with 80 mm thick blocks and a 50 mm layer of bedding sand is regarded as having similar stiffness as a 160 mm rolled asphalt pavement (Soutsos et al. 2011).

The equivalent modulus of elasticity determination method considers a multi-layered section with an equivalent surface layer made up of both the sand and concrete block layers. Approaches to evaluate a concrete block pavement using the linear elastic theory are taken into consideration by assuming the layers are homogenous and isotropic, despite the fact that the top layer of a concrete block pavement comprises of small elements. The pavement structure here is represented by the layer thicknesses, modulus of elasticity and Poisson’s ratio of each layer. The early design of concrete block pavement in the North America follows the multi-layered elastic approach of AASHTO, in which a layer coefficient, counted as the surface layer relative ability to function as a structural pavement component, is imposed for the design (Rada et al. 1992).

The stress calculation underside the bedding layer under the influence of the load distributing effect of the continuous layer of concrete block with thickness h_b is taken into consideration the enlarged circular area of radius, $a' = a + h_b + d$ (here, a is radius of circular loading area and d is bedding layer thickness) (Eisenmann and Leykauf 1988). Irrespective of shape and thickness of blocks, the distribution of stress is considered frustum in shape with an almost 45° load diffusion, and this shape changes with the level of progressive stiffening, with the initial distribution range reaching 250-350 mm from the centre of loading (Panda 2006). While the Category A blocks exhibits a wider surface deflection profile in which Arjun Siva Rathan et al. (2022a) observed that beyond a distance of 400 mm from the central load point, the variation in deflection was almost undetectable. The load distribution is not uniform underneath the block layer, in which variation in deflection increased significantly toward the load's centre in a parabolic form (Arjun Siva Rathan et al. 2022a; Panda 2006). With progressive stiffening, the stiffness of the concrete block pavement increases over time and magnitude of loads (Mampearachchi and Senadeera 2014; Shafabakhsh et al. 2014; Soutsos et al. 2011), the process of formulating thickness design curves for the base layers involves considering the initial composite modulus of 350 MPa, and progressively reaches a peak modulus of 3100 MPa (Rada et al. 1990) while Rollings et al. (1992) recommends equivalent moduli of 214 MPa upto 2585 MPa for interlocking-shaped blocks.

The simplicity and general acceptance, the multi-layered elastic approach has been implemented for development of CBP design procedure. The method is implemented for pavement analysis at long term service period (Zoccali et al. 2018). However, application of an equivalent composite only relies on elastic solutions to distinguish concrete block pavement behaviour and may result in an improper description of the behaviour of the pavement. The existing homogenising the composite of surface layer of concrete block pavement has been assumptions of homogeneous properties assumed at a macroscopic level of the part. However, with the advances of homogenisation of composites, analysis of heterogeneous materials is conducted on the level of the individual constituents that constitute these materials by implementing micromechanics. Explanation of the principles and theory of micromechanics will be explained in Section 2.5.

2.4.3 Discrete Modelling

ECA of composite neglects the interaction between contacting constituents and do not predict the stress concentration as actual situations. An approach that allow calculation of stresses and strains after operating the interaction of the individual pavement units is the discrete modelling using FEM. In FEM analysis by mesh discretisation, the continuous domain is divided into a set of discrete sub-domains (i.e., finite elements), aiming at numerical estimation of the system mechanical response. The necessary inputs for FEM using commercial tools, are domains definition, material properties and behaviour, interaction details, loading and boundary conditions, and type of analysis.

2.4.3.1 Discrete Modelling of geocell reinforced layer

Main shortcoming of ECA is the estimation of an equivalent layer property, and under weighing the effect due to components interaction and the influence of interconnected geocell functioning as a mat. However, in experimental investigations, the strains can be detected by attaching gauges on/ within the constituents of the reinforced layer (Tang and Yang 2013; Thakur et al. 2012; Yang et al. 2012). To overcome the shortcomings of an equivalent homogeneous material, the composite can be discretised to the exact constituents. Infill sand material behavior is commonly elasto-plastic, sometimes linearly on non-linearly elastic, while the geosynthetic is linearly elastic (Hedge and Sitharam 2015a; Hegde and Sitharam 2015; Maji et al. 2016; Yang et al. 2010).

Depending upon the symmetry of the model volume, discrete modelling can be conducted either on a two-dimensional model, axisymmetric model or the complete three-dimensional model (Hegde and Sitharam 2013; Madhavi Latha and Somwanshi 2009; Saride et al. 2009; Yang et al. 2013). Even though analytically less cumbersome and representative of the actual geometry, two-dimensional model is difficult to model the three-dimensional confinement effect due to the geocell. Hence, geocell-soil composite is modelled as two different constituents, geocells as interconnected membrane and infill as deformable volumes (Madhavi Latha et al. 2008). Soil property are commonly taken according to Mohr-Coulomb criterion, Duncan-Chang condition and Hardening Soil Model (HSM) and the geocell walls are designed as plate embedded in the soil volume (Hedge and Sitharam 2015a; b; Saride et al. 2009; Yang et al. 2010; Yünkül et al. 2021). Mohr-Coulomb model and Duncan-Chang model are elastic-perfectly-plastic model and elastic hyperbolic model respectively. HSM is an elasto-plastic second order hyperbolic isotropic model implemented by many researchers to simulate cohesionless soils as non-linear, inelastic, stress dependent material behaviour. The benefits of the deducted shape are being analytically less cumbersome and representative of the actual 3-D nature of the pavement or layer section. With the advances of FEM, complex formulation of the interaction and executing the overall response of the composite is simplified and improved.

2.4.3.2 Discrete Modelling of concrete block pavement

Application of an equivalent composite might lead to an inaccurate depiction of the behaviour of the pavement. Molenaar et al., (1984) illustrated the disparity between this approach to actual pavement, where fitting the profiles of experimental and equivalent composite leads to assuming a very low elastic modulus of the concrete block layer, but even then, with respect to radial distance, the deflection decay is gradual than the decay observed in reality. The assumptions of a linear-elastic multi-layered system for concrete block pavement is insufficient as Houben et al., (1984) illustrated such a pavement do not behave linearly elastic especially on their early life. For that reason, a suggestion that a better structural model should be used is made as a result of the multi-layered systems approach's inability to explain concrete block pavement deflection behaviour while assuming linear elastic theory. It takes high number of load repetitions for the pavement to achieve elastic behaviour due to additional compaction of bedding sand under the vehicular loads and this number reflects the quality of block laying (Shackel 1980). Depending upon the loss of energy consumed in further compaction of the bedding layer, the elastic behaviour can be achieved after different loading cycles. An accelerated trafficking test shows a reduced rate of deformation after 10,000 load repetitions of a 40 kN single axle loaded Heavy Vehicle Simulator (Shackel 1980). Due to good quality control, achievement of properly compacted pavement section in laboratory can produce elastic behaviour in the second loading cycle (Mampearachchi and Gunarathna 2010). However, Panda and Ghosh (2002b) investigated elastic behaviour after 150 load repetitions. Another deficient knowledge is about the rutting caused by other than only accepting subgrade excessive permanent settlement (Rollings et al. 1992).

To predict the structural response of concrete block pavement, it is better to model the constituents of the surface layer as distinctive parts. There are two approaches to modelling the surface layer and its support: (a) The blocks are rigid bodies and supported by springs, that represents bedding layer and jointing sand, and (b) bounded and unbounded materials are rendered as spatial configurations. Concrete blocks can be assumed rigid because its deformation is comparatively negligible and stiffness is larger than surrounding materials and sands assumed as linear springs to imitate the deflection curve of a pure-shear-layer as an assumption that no bending moments are transmitted and only vertical displacement of the blocks will occur (Houben and Jacobs 1988; Molenaar et al. 1984). Such linear springs can be considered for small relative displacement, encountered under impact loading (Houben et al. 1984; Huurman 1996; Huurman et al. 1993; Lin et al. 2016; Molenaar et al. 1984) or/ after during long term performance (Houben and Jacobs 1988; Huurman 1996; Mampearachchi and Senadeera 2014). Another approach of discrete modelling, the rectangular blocks are designed as stiff rectangular plates resting on a Winkler foundation with translational and rotational forces only transmitted at four nodes of the corners (Nishizawa et al. 1984). Instead of linear spring resembling the behaviour, bedding layer and layers underneath can be modelled with linear-elastic three-dimensional parts (Huurman et al. 1993).

Modelling surface layer as an arrangement of rigid unit, interacting through springs only shows the surface deflection of the surface while stresses and strains calculated will not completely reflect actual conditions. Therefore, the disadvantage of representing sandy layers as springs also neglects understanding sand behaviour in the highly stressed region of the pavement. The numerical approach using finite element methods can further handle more realistic modelling of the block paving system. The sand layer, can be represented as continuous beds sandwiched between the pavement elements. Material behaviour for concrete blocks can be treated as linear elastic and sand layer as non-linear, linear elastic or elastic-plastic (Arjun Siva Rathan and Sunitha 2022a; Chua et al. 2000; Di Mascio et al. 2019; Nejad and Shadravan 2010; Nishizawa 2003). The analysis can be conducted as two-dimensional analysis, three-dimensional analysis and axisymmetric analysis. The axisymmetric model represents the block elements by simulating them as circular rings concentric the central axis (Houben et al. 1984). A two dimensional model of the pavement section will only show shape uniformity throughout the width (Houben et al. 1984; Huurman 1996; Kellersmann et al. 1984). Blocks translation and rotation during loading can be clearly established with the three-dimensional model (Arjun Siva Rathan and Sunitha 2022a; Ascher et al. 2006; Gunatilake and Mampearachchi 2014, 2019; Hassani and Jamshidi 2006; Huurman et al. 1993; Mampearachchi and Gunarathna 2010; Nejad and Shadravan 2010; Taheri et al. 2021). The zig-zag arrangement of commonly adopted block pattern, the herringbone is not axially symmetric as the joint and block arrangement differs about different axis of symmetry (Chua et al. 2000).

2.4.4 Structural Analysis of Pavement

Determination of the effects of loads on the pavement and its components can be accomplished by analytical methods or by numerical approximations. FEM is a commonly used numerical approximation, and it is versatile and flexible in pavement design, in which FEM software consists many pavement material properties and options of loading conditions. The initial effort of computerising FEM was done in 1953 by Mr. M. J. Turner's Structural Dynamics Unit, Boeing Airplane Company, which however, did not attain instant recognition(Clough 1980). When Edward L. Wilson and Ray W. Clough created the Symbolic Matrix Interpretive System (SMIS), a structural mechanics computing code, in 1963, the use of FEM in computers was born (Clough and Wilson 1999; Liu et al. 2022). Thereafter, a plethora of FEM softwares made to the market that facilitates certain analyses or is a general purpose tool. However, structural analysis of a foundation can also be formulated with analytical method upon loading its surface by a point load and calculating responses according to the Boussinesq's theory. A multi-layered pavement, can be assumed to consist of layers, each of the layers are made of uniform, homogeneous and linear elastic materials. The common multi-layered theory of structural analysis is based on predictive analysis on the mechanistic approach outputs which uses and verifies with empirical data, and formulating graphs or softwares that can assist in future pavement designs.

2.4.4.1 Structural analysis of continuous layers

Associating to the empirical behaviour of actual pavements, systematic criterial of pavement structural analysis emerged from classical postulates. The theories encapsulate the behaviour under the effect of traffic, variation of support conditions, variation of environmental conditions and variation of component thicknesses and material qualities. Considerable emphasis has been employed towards analysing the mechanical response of pavements to static and dynamic loads, alongside development of theoretical analytical techniques that rely, to some extent, on the computation of critical stresses, strains, and deflections in the structure.

The stresses estimated at any point in a soil mass due to external loading is essential to settlement prediction of a structure. For a foundation with an infinite bottom, according to Boussinesq's theory the solution soil behaviour is the three-dimensional elasticity equations for the homogeneous, isotropic and elastic soil, given by the case where a concentrated force acts on the surface of the semi-infinite volume (Huang 2009). The medium is independent of self-weight effects and obeys Hooke's Law. Unstressed initially, and during load application, the change in volume is neglected. Stress is believed to be continuous through the depth and distributed outward radially and distributed symmetrically from axis passing the centre of loading.

A multi-layered section of pavements response to the external loading is a cumulative response of its layers. Several theories and mechanistic- empirical design software are developed to predict appropriate stress, strain and settlement values which are functions of the layer characteristics. A famous Indian Mechanistic-Empirical Pavement Design Guide (MEPDG) is the development of the IITPAVE program by the Indian Institute of Technology Kharagpur under the MoRTH Research Scheme, R-56-Analytical Design of Flexible Pavement (IRC 2018b; Kumar et al. 2013). The software is developed for the design and study of flexible multi-layered pavement sections. the layers are each composes of homogeneous, isotropic and linearly elastic material, and layer interface are completely bonded to each other. Wheel loads and contact pressure are the load inputs, while layer details required are elastic constants (elastic modulus and Poisson's Ratio of each material) and thicknesses excluding of subgrade. A cylindrical coordinate system is considered in which element in the pavement is located by the depth of the location from pavement surface and its radial distance measured from the vertical axis of symmetry. The current mechanistic-empirical design approaches for multi-layered systems is based on algorithmic techniques for calculating responses within the stratified system comprising elastic materials.

2.4.4.2 Structural Analysis of concrete block pavements

Approaches of concrete block pavement behaviour assessment includes the equivalent composite approaches and discrete modelling. The choice of selecting a simulation model reflects the similarity of replicating the actual geometry and material behaviours. As two-dimensional models do not accurately depict the influence of blocks movement for different arrangement, a three dimensional model can better capture the responses of pavement.

The finite element model is used to simulate the field conditions of the concrete block pavement. Numerous structural analysis tools have been developed that can cater to simulate concrete block pavements, such as, LOCKPAVE (Shackel 2000), BLPPAVE 3D (Nishizawa 2003), DELPAVE (Huurman et al. 2003), SAFE (Hassani and Jamshidi 2006), ANSYS (Gunatilake and Mampearachchi 2014, 2019; Di Mascio et al. 2019; Nejad and Shadravan

2010), SAP2000 (Mampearachchi and Gunarathna 2010), Abaqus/CAE (Lin et al. 2016; Shafabakhsh et al. 2014; Taheri et al. 2021; Zoccali et al. 2018), and PLAXIS (Arjun Siva Rathan and Sunitha 2022a). With varying base thickness, block thickness, subgrade CBR values, and design traffic within 0.5 to 50 msa, Arjun Siva Rathan and Sunitha (2022a) developed a programmed software NITT-BLOCKPAVE that is used to design section meeting deflection and rutting requirement.

Structural tool designed for Nishizawa (2003) study on influence of block pattern using elastic blocks, still implemented springs sand cushion and joints. The surface deflection can be better captured if the jointing sand, bedding layer and underlying layers are continuous beds of linear elastic or elasto-plastic properties. Concrete blocks, assumed elastic and its stiffness can be estimated from the elastic modulus and concrete cube/cylindrical 28 day strength relationship (Mampearachchi and Gunarathna 2010; Taheri et al. 2021). Bedding layer plastic behaviour maybe assume to follow Mohr-Coulomb criterion or the Drucker-Prager criterion (Arjun Siva Rathan et al. 2021, 2022b; Nejad and Shadravan 2010; Shafabakhsh et al. 2014).

Due to the disadvantages of ECA model of concrete block pavement, finite element method simulation of the actual geometry of the pavement is commonly adopted in present researches. The finite element model of the pavement is a volume of finite regions, composing of pavement layers lying one on the other or arranged at same level. The components either interact frictionally or bond onto one another, designed as expected. The interaction between the blocks and surrounding sand is taken as 0.78-0.85 (Arjun Siva Rathan and Sunitha 2022a), 0.30 (Taheri et al. 2021), 0.70 (Di Mascio et al. 2019) and 0.60 (Füssl et al. 2018; Hengl et al. 2018). Laboratory pavement sections are contained within stiffed tanks or pits, and layer walls boundary conditions disallows volume bulging while the section bottom is restrained against all movement. Structural analysis of stress, strain and deformation can be conducted in static, quasi-static or dynamic FEM analysis. In static analysis, loading conditions can be a static load applied onto a loading region, while dynamic amplification factor or impact coefficient is introduced for dynamic loading effects. Dynamic amplification factor (DAF) is calculated by dividing the maximum load effect (static and dynamic combined) by the maximum load effect (static). For dynamic load effects of concrete block pavement complying characteristic speed of traffic on urban and local roads, an analysis considering DAF= 10% is considered (Di Mascio et al. 2019; Taheri et al. 2021). With impact coefficient, a fraction of the static load is taken to ascertain the dynamic load value (Taheri et al. 2021). Even more complicated than static analysis, dynamic analysis handles calculation of system response under dynamic loading.

Material behaviour depends upon the material part assumed, in which comparatively highly stiff material can be considered rigid, otherwise are defined deformable. Deformable bodies can be elastic or undergoing plastic and fracture. Concrete blocks and lower lying layers of base and downwards are mostly assumed elastic, whilst sand lying on the top layers are either elastic or elasto-plastic (Taheri et al. 2021). **Table 2.1** enlisted the material properties of blocks, jointing sand and bedding sand, i.e., modulus of elasticity (E), Poisson's ratio (v), cohesion (c) and angle of internal friction (ϕ), that have been considered in previous works.

Table 2.1: Material properties of blocks and sand of earlier researches

Material	E (MPa)	v	c (MPa)	ϕ (deg.)	Reference
Concrete block Bedding sand Jointing sand	27250 61 48	0.20 0.35 0.35	- 0.00415 0.00321	- 43 38	(Arjun Siva Rathan and Sunitha 2022a)
Concrete block & Jointing sand Bedding Sand	2000 70	0.30 0.35	- 0.00392	- 32	(Taheri et al. 2021)
Sand	100	0.30	-	-	(Di Mascio et al. 2019)
Concrete block Bedding sand	45000 350	0.15 0.30	- -	- -	(Hengl et al. 2018)
Concrete block Sand	12090 10	0.20 0.26	- -	- -	(Lin et al. 2016)
Concrete block Sand	2500 350	0.30 0.35	- 10	- 30	(Shafabakhsh et al. 2014)
Concrete block Sand	23200 10	0.20 0.26	- -	- -	(Mampearachchi and Gunarathna 2010) (Gunatilake and Mampearachchi 2014) (Gunatilake and Mampearachchi 2019)
Concrete block Sand	2500 350	0.30 0.33	- 0.0	- 41	(Nejad and Shadravan 2010)
Concrete block Jointing Sand	30000 350	0.20 0.35	- -	- -	(Hassani and Jamshidi 2006)
Concrete block	29400	0.20	-	-	(Nishizawa 2003)
Concrete block	35000	0.20	-	-	(Chua et al. 2000)
Concrete block	40000	0.25	-	-	(Huurman 1996)

Another important step for FEM analysis is meshing, i.e., creating finite elements and connecting them to formulate a set of functions. Two essential components are computing speed and accuracy, which determine how reliable finite element analysis (FEA) simulations are. Mesh size, element type, and element quality are the main aspects that directly affect the results. Choosing the appropriate element type for a given simulation is essential to guaranteeing accurate results. For example, in a bending model, using fully integrated hexahedral linear components may result in shear locking, which essentially stiffens the model. A mesh sensitivity study should be carried out to determine whether a specific mesh is appropriate for a given analysis. The quality of the mesh serves as an indicator of how uniform, well-shaped, and well-connected the elements are that fill the region.

2.4.5 Experimental Evaluation of concrete block pavement

The behaviour of concrete block pavements have been investigated through ranges of field and experimental tests, such as;

- (i) accelerated trafficking tests,
- (ii) impact testing by falling weight deflectometer (FWD) on roads in service, and
- (iii) laboratory simulation under static or dynamic and repetitive or non-repetitive loading conditions.

Pavement long term performance can be established through accelerated trafficking test of the recently established section by simulating traffic loads numerous times reaching the design traffic volume. Accelerated traffic loading can be simulated by implementing an accelerated loading facility in which a loaded wheel is assembled onto a movable girder or an axle that will provide a to-and-fro wheel movement (Füssl et al. 2018; Ryntathiang et al. 2006), or continuous plying of heavily loaded vehicles and converting impact to an equivalent axle load repetitions (Barber and Knapton 1980). The advantages associated with accelerated pavement tests are: (i) provides the total structure response within a short period of time, and (ii) provides long-term monitoring of pavement condition beyond expected traffic loads. The number of wheel repetitions varies and it is mostly halted when rutting depth is achieved (Füssl et al. 2018). Structural evaluation of the tested pavements is often a follow-up procedure, similarly, Houben and Jacobs (1988) subjected the concrete block pavement to 275,000 wheel load repetitions of a 6 kN wheel load, and regularly, and periodically deflection is measured upon application of a dynamic load of 50 kN. Assessment of pavement performance by dynamic loading, using the FWD is commonly conducted on a road length in service (Huurman et al. 1993).Lately, a light falling weight deflectometer (LFWD) is also adopted for assessment of pavement elastic behaviour (Lin et al. 2016; Yaginuma et al. 2003).

Response and material behaviour under dynamic and static loading differs and this is explained by the strains that are caused due to the different forms of resistive force to the deformation wave. Under dynamic tests, the solid's response to the external force exhibits an elastic oscillatory motion that is transferred longitudinally as an elastic compression wave and this dynamics is characterised by the Young's modulus and Poisson's ratio (Yoshida et al. 2020). The shear strain changes within the elastic threshold shear strain is very small that shear modulus appears constant (Likitlersuang et al. 2013). As the solid is subjected to larger deformation, the relationship between the shear modulus and shear strain varies non-linearly, continues till it reaches the stage where the material loses shear stability and eventually fracture, i.e., material incapability to dissipate the shear stress in the form of travelling wave. Pavement dynamic test such FWD, LFWD and non-nuclear Geogauge, and Ground Penetrating Radar are also called non-destructive tests because they inflict very small strain in the material that the shape of the body behaves elastic. Very small shear strain can also be encountered at low stress levels or stressing a highly stiff material (Thomaz et al. 2021). However, as frequency of the deformation is larger and the loading is considered static. Static type of loading is implemented to determine the maximum loads that the body can withstand and thus testing the material strength.

Modulus of elasticity can be determined from the strain response under static and dynamic loads. The way that the methods for calculating the static and dynamic moduli depends on the practical requirements. The elastic characteristics are obtained from the static modulus if the demand for determining the elastic modulus is framed from the perspective of long-term loading as the stability problem. On the other hand, determining the dynamic modulus is necessary if the loading is short-term, such as the impact of moving vehicles.

A static load subject the pavement to a greater penetrating strain through the depth and expanse of the pavement, and it can be applied once or repeatedly. A gradual loading is applied till peak load is reached, and responses as stresses and displacements are recorded. In the non-repetitive testing on the concrete block pavement, Panda (2009) observed stresses on the base layer when a 51 kN is gradually loaded onto the block surface layer, and at same load, a parametric study was conducted by Nejad and Shadravan (2010) to show significant influence of jointing width, shape, size and thickness of blocks on block pavement behaviour. Soutsos et al. (2011) determined the equivalent pavement elastic modulus of concrete pavement with different block arrangement by the modulus relationship with the modulus of reaction upon applying a 50 kN load onto a 300 mm circular steel plate. Mampearachchi and Gunarathna (2010) and Gunatilake and Mampearachchi (2014) applied a one-time loading of 60 kN, higher than half the maximum legal axle load of most countries. Other researches consider half the standard single axle load, i.e. 40 kN as dynamic or static load (Lin et al. 2016; Shafabakhsh et al. 2014). However, one-time static plate load test on a 300 mm circular plate can be conducted to either 60 kN or stop when deformation rate became less than 0.03 mm/min for each load increment, whichever occur earlier (Arjun Siva Rathan et al. 2022a). The resilient behaviour of the pavement can also be achieved by repeated application of a constant load onto a loading plate to show the stiffness upon consequent deformation (Chua et al. 2000). Arjun Siva Rathan et al. (2022) conducted cyclic loading on a 300 mm circular rigid plate, according to the ASTM specification for calculation of the stiffness ratio, i.e., a ratio of the reloading strain modulus (E_{v2}) to the initial strain modulus (E_{v1}), in which

$$E_{\mathrm{v1}} = 1.5\, a \frac{\Delta\sigma_1}{\Delta s_1} \text{ and } E_{\mathrm{v2}} = 1.5\, a \frac{\Delta\sigma_2}{\Delta s_2} \quad \text{(ASTM 2021)} \qquad \textbf{(2.14)}$$

Equation (**2.14**) assumes the pavement section as an elastic isotropic half-space, in which a is radius of the loading plate, $\Delta\sigma$ is difference in normal stress below the plate, and Δs is difference in deflection between $0.3\sigma_{\max}$ and $0.7\sigma_{\max}$, and $\sigma_{\max}$ is maximum average normal stress below the loading plate. The denotation 1 and 2 for stress and deflection indicates values taken at initial and reloading stage respectively.

Under dynamic action, a 50 kN load can trigger a maximum principal stress only upto 0.924 times the triaxial tests results (Huurman et al. 1992). Modulus of elasticity of concrete block pavement differs in which static modulus is higher than its dynamic counterpart (Arjun Siva Rathan et al. 2023). The higher value of static modulus can be explained due to the progressive stiffening of the block layer (Soutsos et al. 2011) while for dynamic test, the interconnected sand layer in the joints damps the vibration.

The investigation on concrete block pavement can be conducted on actual pavements or laboratory simulated sections. Simulated models composing of the actual pavement materials are constructed within test tanks, test pits or test tracks. Test tanks consists of a rigid steel tank of sides by depth of 775 mm × 775 mm × 450 mm (Nejad and Shadravan 2010; Panda 2006, 2009). The prototype is a laboratory pavement section consisting of the sub-base, bedding layer and blocks compacted into the 900 mm × 900 mm × 360 mm in which pressure cells attached underneath the block layer detected the reduced vertical stress (Soutsos et al. 2011). However, Mampearachchi and Gunarathna (2010) constructed a 1000 mm × 1000 mm × 1000 mm experimental model sufficient to contain the stress distribution that reaches the perimeter of 450 mm away from the center of load application zone (Mampearachchi and Senadeera 2014). Shafabakhsh et al. (2014) simulation model is a conducted in a region of 1180 mm × 1080 mm × 1500 mm, consisting of 100 mm thick surface layer, 20 mm bedding layer, 160 mm base and 1220 mm subgrade. However, for dynamic loading such as LFWD impact and simulated traffic, a larger area of 1500 mm × 1500 mm is recommended (Lin et al. 2016; Di Mascio et al. 2019). Loading plate size and shape is taken to approximately equal tire contact area of single wheel (Mampearachchi and Gunarathna 2010; Shafabakhsh et al. 2014).

The discrete model of concrete block pavement can be validated with ECA elastic model, such as Burmister's model and IITPAVE model, if the pavement encounters small strains that can be considered elastic, and this is encountered after recurring loading (Arjun Siva Rathan and Sunitha 2022c).

2.5 Homogenisation of ICBP Surface Layer

To facilitate effective engineering design and analysis, it is important to appropriately evaluate and describe the selected material for use in engineering systems. The process of characterisation serves two main steps:

a. Identifying the relevant properties of the material to accurately predict the overall response of the system

b. Analysing the local response of the material based on the behavior of the entire system.

A composite is a heterogeneous structural material consisting of two or more constituents that are combined together at a macroscale. One of the constituent is the reinforcing phase or the *inclusion* and the other in which it is embedded is called the *matrix* (Eshelby 1957). The matrix phase is generally continuous while the inclusion is in the form of fibers, particles, filaments, etc. the mechanical advantage of the composite is the presence of the inclusion stiffens the composites. The material behavior becomes complex with heterogeneous media because individual property of the components altogether contributes to the overall composite performance. A unidirectional inclusion such as laminates, strengthens the composite in carrying simple loads such as uniaxial tension or bending, whereas a fiber-embedded composite picks stress equivalently in all direction. The approach to the mechanics of heterogeneous media is predictive, which cannot be achieved quickly or cheaply. Careful derived theories of behavior based on certain hypotheses establish the range within which the outcomes are valid. Confined by the assumptions, the theory possesses a comprehensive capacity to simulate actual behavior.

Composites behavior can be determined through two methods, mechanical and physical experiments, and multiscale composite mechanics (also called micromechanics). Mechanical test of the composites complies the performance in tensile, flexural, impact, shear and compression requirements, whereas, physical testing includes water absorption, density, void content, hardness and durability. Physical experiments seemingly assume the composites as a quasi-homogeneous body and understanding the constituents' roles, each in contributing to the overall composite behavior is limited.

Macroscale composite behavior can be bridged with the microscale features and mechanisms. The main concern to be addressed revolves around how the characteristics of the composite are influenced by the individual properties of its constituent phases, as well as their respective volume fractions, dimensions, and geometry. The primary approach of composite micromechanics is localisation, aims at evaluating the local stress and strain fields based on its macroscale load state, phase properties and geometries. With the implementation of homogenisation theory, the heterogeneous structure is modelled to an equivalent homogeneous medium, which may not necessarily be isotropic (Hill 1965). To highlight, the scales mentioned do not represent the absolute unit of length, instead signify the characteristics of the scales, which depends upon the dimensions of the structure and crystal lattice.

Essentially, the objective of multiscale mechanics is simplifying the analysis by transforming intricate composites into a single, uniform material through homogenisation and de-homogenisation or localisation, which is predicting the local fields such as stress and strains within the microstructure projected through macroscale behavior. Composite micromechanics, a branch of composite mechanics identifies the constituent properties and their geometric configuration, providing a systematic structure with equivalent properties. Establishing the two-way response between local and global dimensions seeks appropriate rendering the idealised characterisation otherwise can lead to inadequate and inconsistent results. The many homogenisation approaches to assess the composite material properties are broadly classified into the analytical mean-field technique and the numerical full-field approaches (Böhm et al.

2010; Henkes et al. 2021). Various multiscale methods facilitates bridging scales from an engineering component down to its microstructure, such as, higher-order three-scale reduced homogenisation (Yang et al. 2021), Fast Fourier Transform based models (Henkes et al. 2021; Tootkaboni and Graham-Brady 2010), mean-field homogenisation of the Representative Volume Element using finite element methods (FE-RVE) (Ali et al. 2021; Jeon et al. 2022; Schmitz and Horst 2014; Tian et al. 2019; Zabihyan et al. 2018), asymptotic homogenisation (He and Pindera 2021; Pinho-da-Cruz et al. 2009), generalised method of cells (Aboudi 2004; Aboudi and Pindera 1992; Arnold et al. 1999), radial point interpolation method (Rodrigues et al. 2018), and incremental secant linearisation method (Rao et al. 2021).

2.5.1 Representative Volume Element for the composite material

One can project the macrostructure is form by a spatial periodicity of the Representative Volume Element (RVE). The size of the RVE is chosen such its response is independent of its location within the structure while also being large enough to be representative. The state of being representative characterises the RVE which is determined by the following assumptions (Beran, 1965; Hill, 1965):

a. On average, the representative volume possesses structural characteristics that are representative of the entire mixture.

b. The representative volume must include sufficient number of inclusions to ensure that the overall moduli are not significantly influenced by the surface values for traction and displacement, so long as these values are ‘macroscopically uniform’.

RVE maximum size is determined if it exhibits statistically homogenous constitutive response (Böhm et al. 2010; Drugan and Willis 1996; Hashin 1983; Kanit et al. 2003; Shahzamanian et al. 2022). In order to achieve a statistically uniform response, it is convenient to impose boundary conditions that result in uniform fields within the body (Hashin 1983). By statistical homogeneity, the responses, i.e., stress and strain fields at every location on the RVE are statistically admissible (Böhm et al. 2010), which their average is calculated at RVE center, and such focal points interprets each material point at a macroscale (Ogierman and Kokot 2013).

2.5.2 Finite Element homogenisation scheme

Consider a structure, occupying a domain Ω with an external boundary $\partial\Omega$ in the current configuration at macroscale. The material is assumed heterogeneous, composing of a periodic microstructure. the structure is subjected to a prescribed displacement and forces on the disjoint complementary part of the Dirichlet boundaries ($\partial\Omega_u$) and Neumann boundaries ($\partial\Omega_q$ or Γ). In the absence of body forces, the differential equation for quasi-static equilibrium employed to estimate the effective mechanical properties is given by Equation (**2.15**).

$$\nabla\bar{\sigma}(\bar{x}) = 0 \tag{2.15}$$

where, in current configuration (t + dt), $\bar{\sigma}(\bar{x})$ is Cauchy stress tensor of a point at location $\bar{x}$ within the macroscale domain. Weighted stress at initial configuration (t= 0) is measured as Kirchhoff stress. For a point in the body, moving at an arbitrary potential, action at any configuration is defined by a smooth function called the Lagrangian function. Lagrangian formulation is based on the stationary-action principle in which the computation at current configuration (t + dt) is based on the previous configuration at t (Hand and Finch 1998; Morin 2008; Tchalla et al. 2013). According to the principle of stationary action, strain rate is infinitesimal, i.e., the reference and current configuration are infinitesimally different, thus making the Kirchhoff stress and Cauchy stress almost the same. The strain rate to the Cauchy stress is a conjugate strain rate, i.e., the rate of deformation ($\bar{F}$) that is defined as:

$$\bar{F} = \frac{1}{2}\left(\nabla\bar{v} + \nabla\bar{v}^{\mathrm{T}}\right) \quad \text{(Tchalla et al. 2013)} \tag{2.16}$$

where $\bar{v}$ is the velocity field. The canonical boundary conditions on $\boldsymbol{\omega}$ defined as:

$$\begin{aligned} \bar{u}(\bar{x}) &= \hat{u}(\bar{x}) \text{ on } \partial\Omega_u \\ \bar{\sigma}\cdot\mathbf{N} &= F \text{ on } \Gamma \end{aligned} \quad \text{(Tchalla et al. 2013)} \tag{2.17}$$

Where displacement field in the macroscale is given by $\bar{u} = \bar{x} - \bar{X}$, $\hat{u}$ is a specified displacement of a point located at $\bar{X}$ in the initial configuration. **N** is the unit normal vector to

ω and F is a prescribed load. The weak form associating the problem statement and boundary conditions of Equation (**2.15**) and (**2.17**) is given

$$\int_{\Box} \bar{\sigma} : \delta\bar{F} \; d\Box = \int_{\delta\Box_q} F : \delta\bar{v} \; d\Gamma \tag{2.18}$$

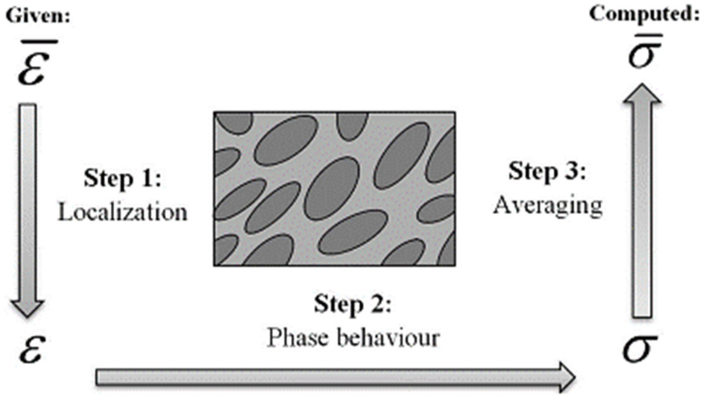

Figure 2.6: Micromechanical homogenisation scheme (Ogierman and Kokot 2013)

As shown in **Figure 2.6**, the constitutive relation between $\bar{\sigma}$ and $\bar{F}$ at this scale is computed by solving localised finite element problem through steps of localisation, predicting microscale behaviour of the composite and averaging the material properties prior implementation at macroscale/ whole part size of the system.

Now, assume the heterogeneous microscale material which is heterogeneous that is characterised by a volume occupying a finite domain ω within the macroscale domain $\Box$, with external boundary $\partial\omega$ in current configuration. In the absence of body force, the equilibrium equation is given by

$$\nabla\sigma(x) = 0 \tag{\textbf{2.19}}$$

where $\sigma(x)$ is Cauchy stress tensor at a microscale location x. The microscale structure or RVE is subjected to boundary conditions depending on the macroscale strain tensor $\bar{\varepsilon}$. Macroscale strain tensor is calculated as strain-rate tensor, defined as the integral of deformation rate. The total strain is approximated over the integral of the strain rate at every increment. Periodic boundary conditions (PBC) are implemented along the perimeters of the RVE, such that,

$$u^{+} - u^{-} = \bar{\varepsilon}\left(x^{+} - x^{-}\right) \quad \textbf{(2.20)}$$

where u is displacement at the microscale. + and – signs denote the node indices located on opposite sides of the RVE. Assume an elastic material behavior, the constitutive equation is generalised as follows:

$$\sigma(x) = \mathbf{C}^{r} : \varepsilon(x) \quad \textbf{(2.21)}$$

where $\mathbf{C}^{r}$ is the fourth-order elastic tensor corresponding to phase r, and ε is the strain tensor. The weak form of the equilibrium equation is formulated as

$$\int_{\omega} \sigma : \delta\varepsilon \; d\omega = 0 \quad \textbf{(2.22)}$$

Thereafter, phase stress tensors are averaged and macroscale stress tensor are obtained. The two response at the micro and macroscale are coupled to evaluate the equivalent stress $\bar{\sigma}$ at a particular point $\bar{x}$ at domain □

$$\bar{\sigma} = \langle \sigma(x) \rangle = \frac{1}{V} \int_{\omega} \sigma(x) \; d\omega \quad \textbf{(2.23)}$$

(Suquet 1985; Tian et al. 2019)

(here, $\langle \; \rangle$ is the averaging operator)

here, V is the volume of the RVE.

By linear constitutive law, the relationship between the macroscopic stress and the macroscopic strain can be written as

$$\bar{\sigma} = \langle \sigma(x) \rangle = \bar{\mathrm{C}} : \bar{\varepsilon} \quad \textbf{(2.24)}$$

where $\bar{\mathrm{C}}$ is the macroscopic fourth order tensor, also the homogenised elastic property of the microscopic constituents. For non-linear constitutive law, the relationship is written in an incremental form:

$$\Delta\bar{\sigma} = \bar{\mathrm{C}}_{\mathrm{t}} : \Delta\bar{\varepsilon} \tag{2.25}$$

where $\bar{\mathrm{C}}_{\mathrm{t}}$ is the homogenised macroscopic tangent modulus derived from the non-linear behaviour of the microscale structure.

Coupling the equivalent property at the microscale to the macroscopic level engages determination of the homogenised constitutive tensor at the microscopic level.

2.5.2.1 Microscale homogenisation

There are two ways of achieving the homogenised macroscopic constitutive tensor from the equivalent response of microscale constituents. The common approach of micromechanics is direct FEA on the microscale composite or application of mean homogenisation method on the RVE. Computed results of the former method is very accurate since stresses and strains through the RVE is analysed in detail whilst contrariwise, is computationally expensive (Perdahcioğlu and Geijselaers 2011).

a) Two scale homogenisation

Equivalent properties of material at a RVE is derived following the transformation problem according to Eshelby's theory of inclusion embedded in an equivalent continuum matrix (Eshelby 1957). In an infinite, homogeneous, isotropic elastic medium, the inclusion undergoes deformation, but due to the constraint imposed by its surroundings (i.e., matrix), this will only be an arbitrary homogeneous strain. The transformation problem involves a sequence of imaginary cutting, straining and welding operations of the microstructure. The inclusion is cut off and removed from the matrix, after which, an unconstrained transformation is allowed to take place. Surface tractions is applied onto the inclusion to restore its original form, thereafter, it is put back into the matrix and rejoin across the cut. The inclusion now has some stress but it is zero in the matrix. The surface traction applied is effectively integrated as a layer of distributed body force along the interface between the matrix and the inclusion. To eliminate the unwanted interface stress, an opposing external body force is applied. During the stress elimination, elastic property is derived for the elastic field generated by this counteracting force. The constitutive modulus at the microscale is associated with the macroscale problem to define the the homogenised elastic property/ constitutive modulus ($\bar{\mathrm{C}}$). Responses in the RVE are updated for extracted macroscale strain ($\bar{\varepsilon}$), and constitutive modulus is iterated.

b) Mean field homogenisation (MFH)

Mean-field method of homogenisation (MFH) is an analytical homogenisation approach that executes approximation of the volume-averaged stresses and strains within the RVE (Ogierman and Kokot 2013). Besides local stress and strain, thermodynamic and physical properties such as, mass, specific internal energy, specific entropy and dissipation are also averaged out (Suquet 1985).

For stress and strain field (*f*) in the microscale composite, according to MFH, the average functions $\left(\langle f \rangle\right)$ in ω are defined

$$\langle f \rangle = \frac{1}{V}\int_{\omega} f(\boldsymbol{x})\, d\boldsymbol{x} \qquad \text{(Beran 1965; Tian et al. 2019)} \qquad \mathbf{(2.26)}$$

The statically acceptable range of averaging follows the condition, for which the criterion for an elasticity problem is postulated as:

$$\Delta\bar{\mathrm{C}} = \tilde{\sigma}\,\tilde{\varepsilon} - \frac{1}{V}\int_{V} \sigma\,\varepsilon\,\mathrm{d}V \approx 0 \qquad \text{(Wojciechowski 2018)} \qquad \mathbf{(2.27)}$$

$\tilde{\varepsilon}$ is a symmetrical second rank tensor also called homogenised strain tensor and $\tilde{\sigma}$ is the homogenised stress tensor, both are independent on x (Kanit et al. 2003; Oller et al. 2005). $\tilde{\varepsilon}$ and $\tilde{\sigma}$ are derived as volume averages of microscale stress and strain fields, and given by

$$\tilde{\varepsilon} = \frac{1}{V}\int_{V} \varepsilon\, dV$$

$$\text{(Suquet 1985; Tian et al. 2019)} \qquad \mathbf{(2.28)}$$

$$\tilde{\sigma} = \frac{1}{V}\int_{V} \sigma\, dV$$

The homogenisation procedure at the microscale involved by imposing boundary conditions. The boundary conditions applied on the RVE is governed by the Hill-Mandel condition such that the homogenised material is energetically equivalent to the original heterogeneous material (Böhm et al. 2010; Javili et al. 2017; Peng and Yu 2018).

$$\tilde{\sigma}\,\tilde{\varepsilon} = \frac{1}{V}\int_{V} \sigma\,\varepsilon\,\mathrm{d}V \tag{2.29}$$

The RVE is assigned two types of boundary conditions at its boundary, i.e., homogeneous boundary conditions (HBC) and periodic boundary conditions (PBC) (Al Kassem 2009). Kinematic Uniform Boundary Conditions (KUBC) and Static Uniform Boundary Conditions (SUBC) are the two types of HBC in which former induces strain through RVE, while in SUBC, the RVE experiences imposed stresses (Kanit et al. 2003; Shahzamanian et al. 2022). The boundary condition should also ensure the element maintains the cubic shape upon deformation, effectively preventing the emergence of stress concentration (Shahzamanian et al. 2022).

Briefly defining the three boundary conditions the following way in order to calculate the effective properties of the composite ω:

a) **Kinematic Uniform Boundary Condition** (KUBC)

Kinematic uniform boundary condition (KUBC) refers to a boundary condition where the displacement of the boundary points is constrained to be uniform. Within boundary $\partial\omega_u$, the displacement u imposed at a location x is such that:

$$u = \tilde{\varepsilon}\,.\,x \quad \forall x \in \partial\omega_u \quad \text{(Hashin 1983)} \tag{2.30}$$

b) **Static Uniform Boundary Conditions** (SUBC)

Static uniform boundary conditions (SUBCs) involve imposing constraints on the points of the boundaries such that they experience uniform forces or tractions. For SUBC, the traction vector t prescribed at the boundary $\partial\omega_q$:

$$t = \tilde{\sigma}.\,n \;\forall x \in \partial\omega_q \quad \text{(Hashin 1983)} \tag{2.31}$$

where, n is the vector normal to $\partial\omega_q$ at x

c) **Periodic Boundary Conditions** (PBC)

The Periodic Boundary Conditions (PBC) simulates the deformation of the material beyond an RVE, or in other words, an infinite lattice is created by repeating the RVE throughout space. The PBC therefore prescribes the opposite pairs of edges and surfaces on the boundary of ω, in such a way they deform congruently under a specified loading history. Consider the boundary $\partial\omega$ fragmented into two opposing parts, $\partial\omega^{-1}$ and $\partial\omega^{+1}$ such that normal vectors (n) at these boundaries satisfies $n^{-1} = -n^{+1}$ and

$$\varsigma_{\partial\omega^{+1}} \cap \varsigma_{\partial\omega^{-1}} = 0 \text{ and } \varsigma_{\partial\omega^{+1}} \cup \varsigma_{\partial\omega^{-1}} = \partial\varsigma \text{ (Tian et al. 2019)} \qquad (\mathbf{2.32})$$

where, ς is a model parameter such as displacement, temperature, velocity, etc., and $\partial\varsigma$ is the implemented change in model parameter.

Involving displacement as the model parameter, the additional condition for selected boundary condition is the local strain ($\boldsymbol{\varepsilon}(u)$), which composes of average strain ($\tilde{\varepsilon}$) and fluctuation field ($\boldsymbol{\varepsilon}(u^*)$) (Suquet 1985).

$$\boldsymbol{\varepsilon}(u) = \tilde{\varepsilon} + \boldsymbol{\varepsilon}(u^*) \text{ and } \left\langle \boldsymbol{\varepsilon}(u^*) \right\rangle = 0 \qquad (\mathbf{2.33})$$

According to Eq. (**2.33**), the fluctuation field vanishes at the boundary for KUBC, periodic for PBC, and is interpreted as an integral constraint on the fluctuation field for SUBC (Álvarez-Barrientos et al. 2021; Wojciechowski 2018).

2.6 Summary of literature review

A summary of the literature review is categorised as follows:

a. Concrete block pavement has been an alternative of pavements that promises a better performance than conventional flexible pavement because it can withstand heavy and slow moving traffic. Other benefits include faster construction and easier to maintain. A summary on the literature review on concrete block pavements are as follows:
   - The behavior under vehicle trafficking is greatly influenced by the block shape, block size, block arrangement pattern, bedding layer composition, bedding layer thickness and support strength. However, there has been incidents of CBP failure, which are due to improper supports, degradation of bedding sand, loss of jointing sands, which aggravated to a pavement failure. Structural and functional failure includes rutting, unequal settlement, elephant footprint, horizontal creep and ravelling, and block

cracking, spalling, chipping, abrasion wear, joint sand loss respectively. It has been addressed that delay in propagation of failure to the surface requires following strict construction practices while using adequate materials that do not disintegrate under vehicular stress.

- The structural analysis of concrete block pavement has been simulated using software computational effort by 2D, axisymmetric or multi-layered elastic modelling. The surface layer is modelled as discrete rigid blocks resting on a spring bed, elastic blocks resting on an elastic bedding layer or it is homogenised to an equivalent composite layer.
- Unlike conventional pavements, concrete block pavement upper layers undergo progressive stiffening, i.e., stiffening due to blocks interlocking, blocks wedging in sand layers and sand residual compaction. Depending upon the stage of progressive stiffening, the granular layers are either considered to behave elastically or elasto-plastically.
- Experimentally, the pavement is subjected to static or dynamic load, replicating the intensity and types of loading. Static loading can be conducted repetitively or one-time. Repetitive loading accelerates the long term behavior of the pavement and a one-time application of a load will mimic the pavement behavior during the early stage of service life.

b. Geocells has been a common option of reinforcing marginal quality materials. Geocell stabilisation is an advanced engineering technique used to enhance the structural integrity and load-bearing capacity of soil and various construction projects. It involves the deployment of three-dimensional cellular structures, typically made of high-strength materials such as polyethylene, which are placed on the soil surface and then filled with appropriate infill materials like aggregate, soil, or concrete. These interconnected cells create a network that effectively confines the infill material, preventing it from shifting or settling. Geocell stabilisation is employed in various applications, including road and pavement construction, slope protection, erosion control, and retaining wall support, to provide improved stability, reduce soil erosion, and extend the lifespan of infrastructure projects. This innovative technique offers both cost-effective and environmentally-friendly solutions to a wide range of geotechnical challenges. A summary on the literature review on concrete block pavements are as follows:

- The influence of geocell stabilisation is motivated by the geocell size and its geotextile. Geocell aspect ratio shows the higher its value, better the stiffness. Denser the geocell in the geocell mat, greater is the beam effect. Stiffer geotextile that makes the geocells, better is the confinement effect.
- The influence of geocell on layer strength enhancement also depends upon the location of the layer and magnitude of stress it receives. This is explained by the confinement effect that activates according to the pressure it receives on the geocell walls.
- There are three ways of modelling the geocell reinforced layers. The enhancement in layer strength is considered as an apparent cohesive strength that is included to the shear strength of the infill material. Secondly, reinforced layer is considered homogeneous and consists of a material of enhanced stiffness. Thirdly, the layers are modelled discretely and the overall behavior is a result of their interaction.

c. Homogenisation of a composite layer can be done at a scale of the engineering part (macroscopic scale) or at the constituent scale (microscopic scale). Finding the equivalent material of the composite can be achieved by micromechanics, i.e., the study of the mechanical behavior of materials at a very small scale, typically at the level of individual grains, fibers, or particles within a material. It involves the analysis and modeling of the interactions and properties of these microstructural elements to understand and predict the overall mechanical properties of the material.

Initially, it requires choosing the representative volume element (RVE) of the part. The stages of homogenisation initiates by introducing the macroscopic strain as a driving field for the RVE. With implementation of proper boundary conditions, the equivalent material property is calculated and coupled with the macroscopic response. The equivalent property is determined in two ways: two-phase homogenisation according to Eshelby's theory of inclusion and mean field homogenisation.

2.7 Motivation for the present study

The motivation identified from the research gaps identified from the review of the existing literature are as follows:

- The bedding layer is located in a highly stressed zone of the concrete block pavement. When approximating the level of stress with a flexible pavement response at the base (IRC 2018b), the bedding layer of the block pavement may be strained to approximately 0.01-0.12 %, that it has behaved non-elastically and possibly has undergone plastic deformation (Likitlersuang et al. 2013). Therefore, there is the need to address enhancement the stability of the pavement by enhancing the bedding layer strength. In heavy and slow trafficked section, bedding layer has been recommended for chemical stabilisation method by mixing lime or concrete. However, the bedding sand can also be strengthened by another stabilisation method, i.e., mechanical stabilisation by reinforcing bedding sand within geocell. The stability of bedding layer is expected to enhance due to confinement effect of stiff geocells and beam effect of the interconnected geocells. Researches on this remedy has mostly been implemented in base and sub-base pavement layers. It is commonly known that the effect of geocell stabilisation is influenced by the cell sizes and materials. Denser and deeper the geocell mat, the stiffness of the layer increases. Therefore, the idea of stabilising the bedding layer expecting an enhanced overall behaviour of the pavement, motivates the present study in conducting structural analysis on the interlocking block pavement by embedding various sizes of geocells within the bedding layer.
- Due to progressive stiffening, the stability of concrete block pavement improves with its service life. In other words, in the initial period, the blocks wedge into the bedding layer, interlocks about each other, and continuing compaction of the underlying layers. It is during this period, that unexpected heavy loads may lead to uneven settling of the bedding layer causing early rutting and localised settlement. Therefore, this motivates the structural analysis of the ICBP, by simulating behaviour during the initial stage of service life. This will also show the effect of confinement on early life pavement behaviour. To analyse the pavement behaviour at such a pavement age, a non-repetitive static plate load test is conducted.
- According to literature, Category A blocks when laid in a herringbone pattern provides the best resistance to deformation. Despite the commendation, the present study will determine the magnitude of influence of bedding layer stabilisation in the concrete block pavement with Category A block arranged in herringbone pattern.
- Simulation of concrete block pavement requires a hard run on software computations. Due to the complexity in the geometry of the surface components, earlier studies

attempted to structural analysis of concrete block pavement by considering 2D models, axisymmetric models or multi-layered elastic models. It is also common to homogenised the surface layer to an elastic, homogeneous, isotropic layer. However, due to the difference of the surface section along the depth and surface, the behaviour of the surface may not be isotropic. Therefore, this motivates homogenisation of the surface layer at the constituent level, and implementing micromechanics.

Chapter 3. Experimental Methodology

3.1 General

This chapter outlines the experimental methodology employed in the study to assess the effect of geocell stabilisation on the bedding layer of the ICBP. It begins with the presentation of a flow chart and relevant details regarding the laboratory investigations. A detailed discussion on the selection of materials and test method is also included.

3.2 Experimental Methodology

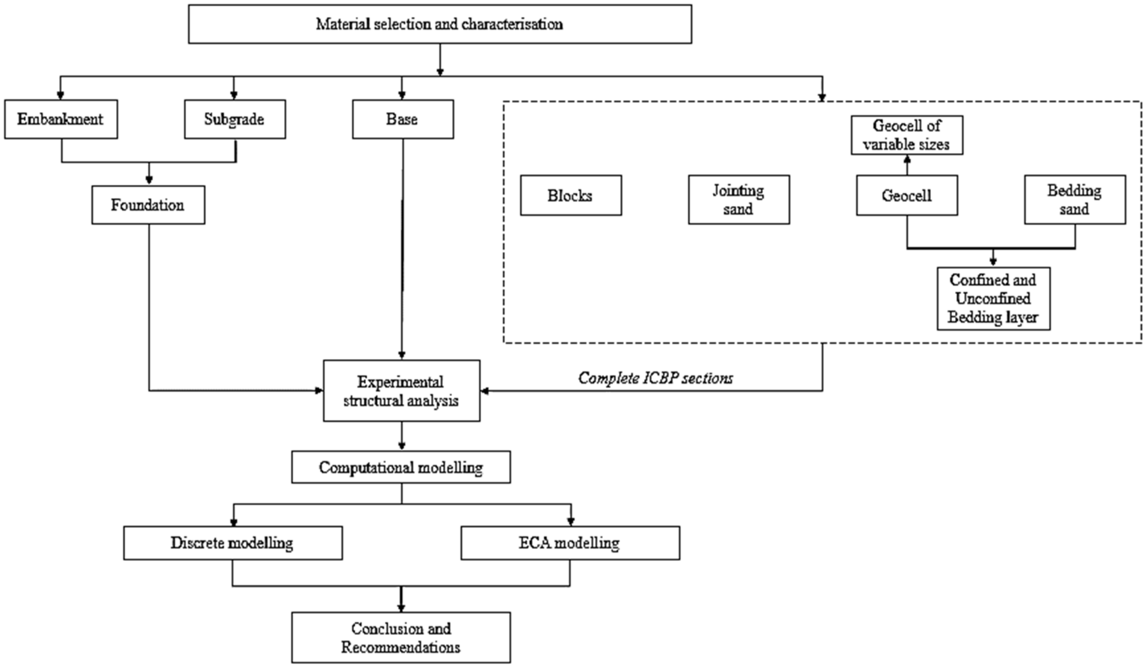

Figure 3.1: Flow chart representing the experimental and simulating background

The scope of the study is divided into three stages, as described in Section **1.4**. The schematic representation of the research methodology adopted for fulfilling the scope of study is shown in **Figure 3.1**. Granular materials and concrete blocks are procured locally while geomaterial which has to be tailored to specific geocell opening sizes. Physical tests according to specifications to determine their adoption for ICBP construction are conducted. Then the materials are compacted into the embankment, subgrade, base, bedding layers and surface layer. Experimental investigation of structural properties of the pavement sections are assessed by static plate load test on the foundation (subgrade and embankment), base and ICBP sections.

The structural properties of the layers are determined from computational modelling using discrete method and equivalent composite approach (ECA).

3.3 Material selection and characterisation

The fundamental structure and groundwork of the ICBP share similarities with traditional flexible pavement. The materials chosen for the foundation, including the embankment, subgrade, and base, adhere to the specifications outlined by the Ministry of Road Transport and Highways, Government of India (MoRTH). The selection of bedding materials and concrete blocks follows the guidelines set by the Indian Roads Congress (IRC) and the Bureau of Indian Standards (BIS) respectively. Meticulously, materials are selected that they suit the construction of a pavement handling commercial traffic. Therefore, the test pit contents include embankment, subgrade, base, bedding layer and surface layer consisting blocks and jointing sand.

3.3.1 Foundation soils

The foundation soils include materials of embankment and subgrade layers. Embankment constitutes of a silty soil of low plasticity (ML soil), that is sourced from the banks of Brahmaputra River. The laboratory obtained physical properties of embankment and subgrade soil is listed in **Table 3.1**.

The requirement of a subgrade soil according to MoRTH (MoRTH 2013) is the density, which is higher than that of the embankment soil. Referring **Table 3.1**, the silty soil could not be used as subgrade material because it did not meet the minimum density requirement.

Table 3.1: Physical properties of embankment soil and subgrade soil.

Layer	Property	Results	Specification Limits
Embankment (MoRTH 2013)	a. Soil Type b. Maximum Dry Density c. Optimum moisture content d. Soaked and Unsoaked CBR	ML Soil (BIS 1970) 1.613 g/cm^3 12.8 % 4.61 % and 13.25 %	- 1.5499 g/cm^3 (Min.) - -
Subgrade (MoRTH 2013)	a. Soil Type b. Maximum Dry Density c. Optimum moisture content d. Soaked and Unsoaked CBR	SP soil (BIS 1970) 1.834 g/cm^3 8.8 % 7.96 % and 27.69 %	- 1.7845 g/cm^3 (Min.) - -

To fulfil the specified requirements, different proportions of manufactured sand (aggregate bin of stone dust) are added with the river soil and individual density is determined. The maximum dry density for different stabilised river soil is given in **Figure 3.2**.

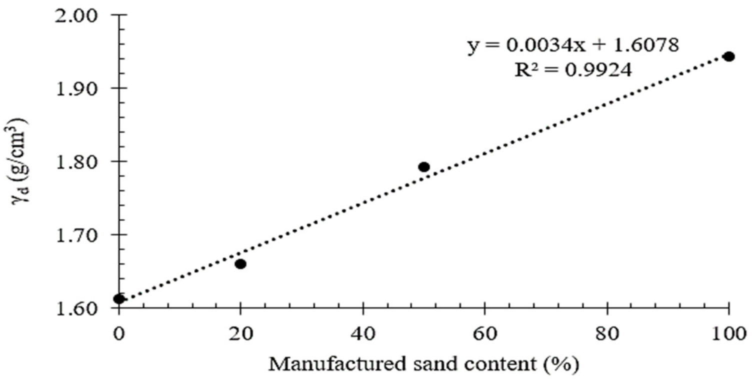

Figure 3.2: Maximum dry density of different manufactured sand contents

As shown in **Figure 3.2**, MDD of subgrade soil increases with larger proportion of river sand replaced by manufactured sand. A sand content at 50 % by weight of subgrade material, is marginally meeting the minimum density required. A replacement with manufactured sand by 60 % by weight of river sand is sufficient and will ensure the minimum density achieved in test pit. Gradation of the three soils, i.e., embankment soil, manufactured coarse grained soil and blended subgrade soil are shown in **Figure 3.3**.

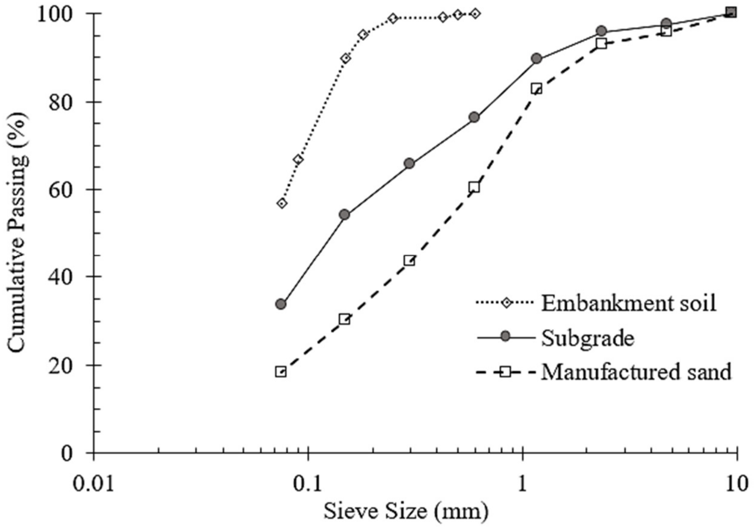

Figure 3.3: Gradation of embankment soil and subgrade soil.

3.3.2 Base material

Base composes of Wet Mix Macadam (WMM), of gradation according to specification (IRC 2012). Blending of aggregates three bins procured from Mandakata quarry, Assam such that to fit the IRC specified gradation of Grading-2 is shown in **Figure 3.4**

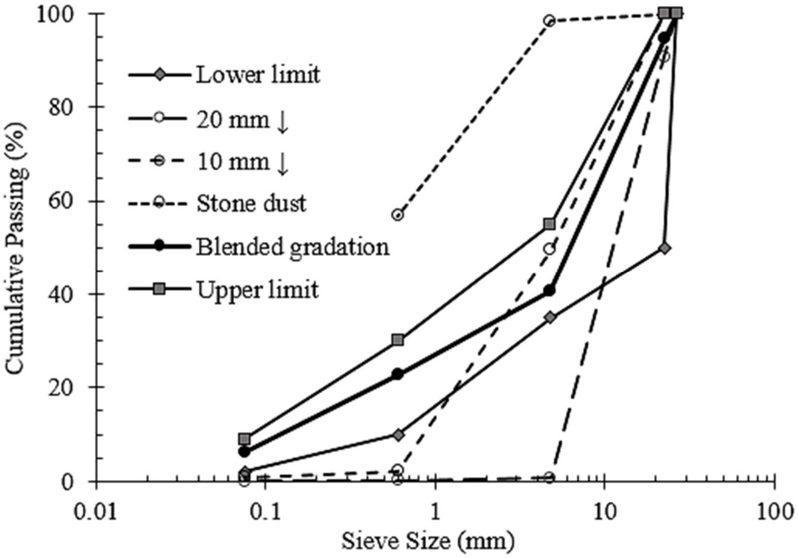

Figure 3.4: Gradation of base material

Blended proportion of aggregates from bin 20 mm down (20 mm ↓), 10 mm down (10 mm ↓) and stone dust are 58 %, 2 % and 40 %, respectively. The physical properties of base materials used are given in **Table 3.2**.

Table 3.2: Physical properties of base material

Layer	Property	Results	Specification Limits
Base (IRC 2012; MoRTH 2013)	a. Type	WMM-Grading 2	-
	b. Maximum Dry Density	2.217 g/cm^3	-
	c. Optimum moisture content	5.46 %	-
	d. Soaked and Unsoaked CBR	192.4 % and 206.7 %	30% (Min.)
	e. Impact Value	21.81 % 29.54 %	30 % (Max.) 35 % (Max.)

	f. Combined Flakiness and Elongation Index g. Water Absorption	1.6 %	2 % (Max.)

3.3.3 Surface and bedding layers

The sands that are placed into the joints and bedding layer of ICBP are selected according to block pavement specifications (IRC 2004, 2018a). Sharp sand particles for bedding is preferred, therefore, bedding sand is sieved from manufactured sand that is procured from Mandakata, Assam with finer fractions contributed by Brahmaputra River soil. The gap in between blocks is filled with sand that is finer than bedding sand, the size appropriate of free flowing within the spaces. Since sands for the joints be clean washed and dry, the sand used has been sieved and blended with Meghalaya and Brahmaputra river, Assam sands. Following the specified gradation accordance to the Indian Roads Congress, the materials are sieved and blended to mid-point of gradation ranges, as shown in **Figure 3.5** and **Figure 3.6**.

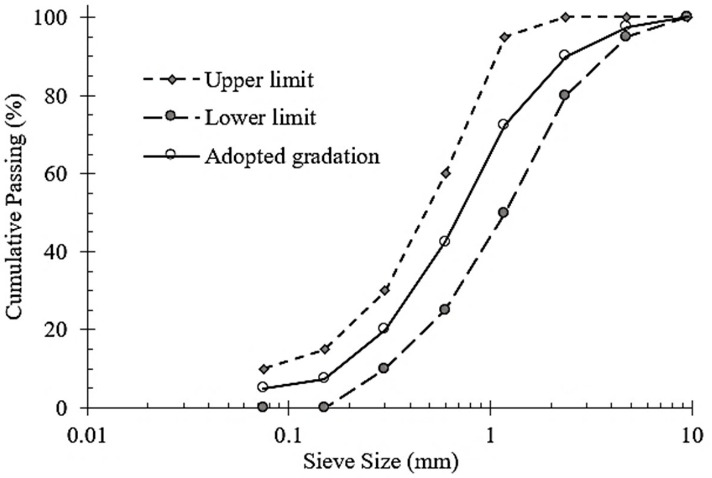

Figure 3.5: Bedding Sand gradation

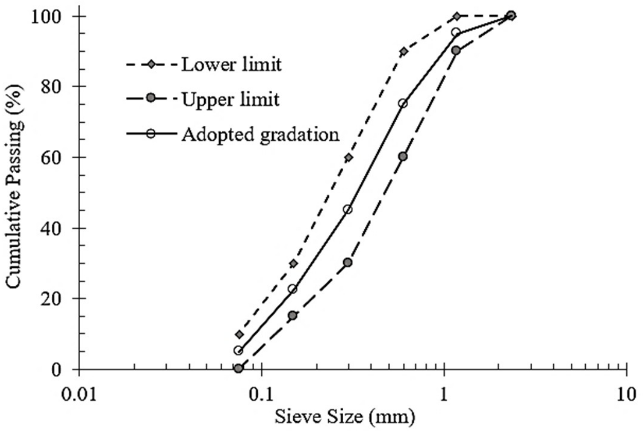

Figure 3.6: Jointing Sand gradation

Concrete blocks have been locally procured from the nearest block casting factory located in Mirza, Assam. The block thickness and concrete grade are selected as specified for lanes bearing commercial traffic, and the shape is interlocking on all sides (IRC 2004, 2018a). The physical properties of sands for the joints and bedding layer, and concrete blocks are given in **Table 3.3**.

Table 3.3: Physical properties of surface and bedding layer materials

Layer	Property	Results	Specification limits
Bedding Sand (IRC 2004, 2018a)	a. Gradation	As per specification	-
	b. Maximum Dry Density	1.972 g/cm^3	-
	c. Optimum moisture content	10.47 %	-
	d. Water Absorption	1.2 %	2 % (Max.)
Jointing Sand (BIS 1983; IRC 2004, 2018a)	a. Gradation	As per specification	-
	b. Maximum Density	1.6993 g/cm^3	-
	c. Minimum Density	1.023 g/cm^3	-
Concrete Blocks (BIS 2006; IRC 2004, 2018a)	a. Shape class	Category A	-
	b. Concrete grade	M40	-
	c. Length (L)	263 mm	-
	d. Width (W)	133 mm	-
	e. Thickness (T)	80.65 mm	-
	f. Plan Area	27755.5 mm^2	-
	g. L/W	1.977	-
	h. Aspect Ratio	3.26	-
		4.54 %	6 % (Max.)

	i. Water Absorption		

3.3.4 Geocells

Readily available geocells comes in limited sizes as they are primarily designed for inner pavement layers. However, the sizes of the geocell openings that can be implemented in the bedding layers will vary in the range that the confinement is substantial enough to have a significant impact yet small enough that it can accommodate infill comfortably at an ease of compaction. Smaller the aspect ratio and opening size and larger the depth, geocells improves the soil stiffness better. Panda (2006) observed for the range of block thickness, block shape and laying pattern, the pressure detected at the lower side of bedding layer completely dissipated at distances of 250-350 mm from the loading plate while Arjun Siva Rathan et al. (2022a) observed the difference in deflection dissipates at 400 mm. Therefore, the maximum opening is fixed to a size of 350 mm, and the lowest size is decided by the possibility of sealing the geocells.

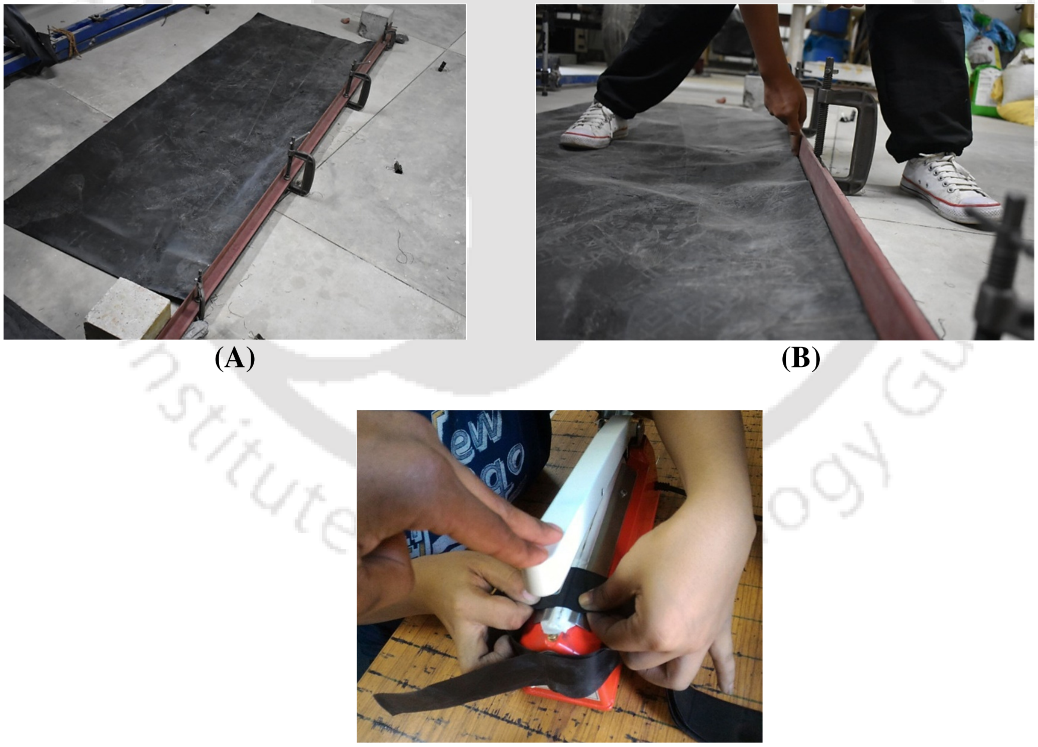
(A)
(B)
(C)

Figure 3.7: Geocell preparation: (A) clamped HDPE sheets, (B) sheet trimming, and (C) seam sealing

The geocells are trimmed from an HDPE sheet, with depth controlled cutting by clamping the sheet in between two 40 mm angle sections (See **Figure 3.7 (A)** and **Figure 3.7 (B)**). The strips are then manually sealed by heat bonding, using a 220 V/ 400 W hand sealing machine (See **Figure 3.7 (C)**). The geomaterial is a 0.32 mm thick HDPE sheet that is procured from K. K. EnviroTech Pvt. Ltd., Kolkata. Properties of the HDPE sheet is given in **Table 3.4**.

Table 3.4: Physical properties of the geomaterial

Layer	Property	Results
HDPE sheet (ASTM 2018, 2019; IRC 2019; ISO 2019)	a. Thickness	0.32 mm
	b. Tensile strength	83.553 MPa
	c. Elongation at break	171 %
	d. Seam strength	10.248 MPa

As seen in **Figure 3.8**, the strips are sealed to pocket sizes 350 mm × 350 mm, 250 mm × 250 mm, 150 mm × 150 mm and 80 mm × 80 mm and trimmed to a fixed 40 mm depth, which is within the 30-50 mm bedding layer depth (IRC 2004).

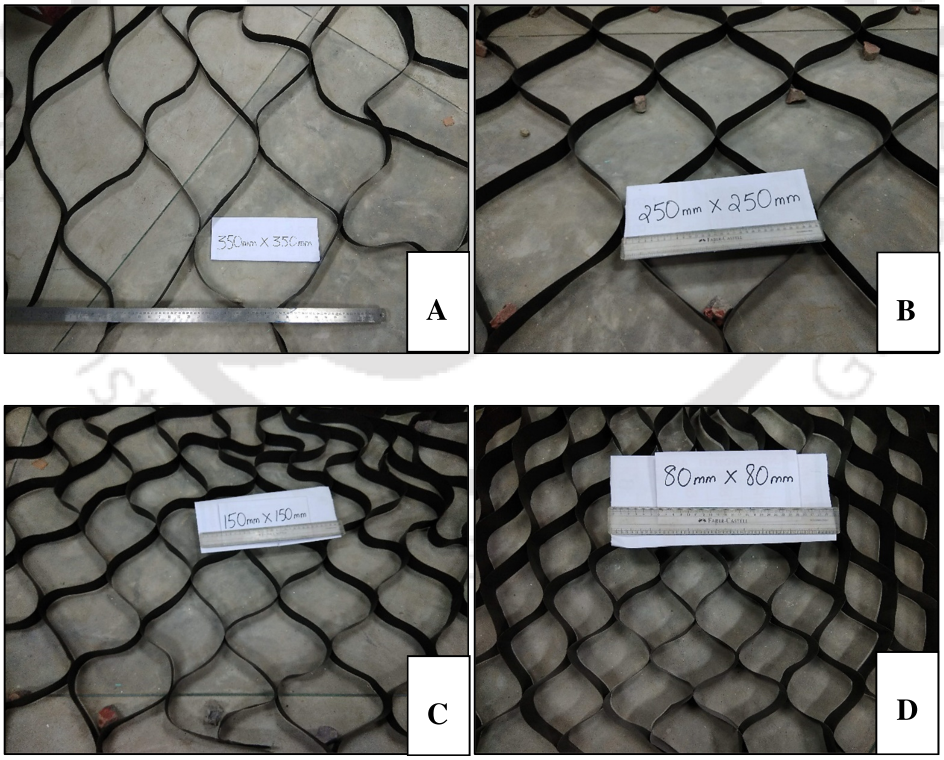

Figure 3.8: Geocells of openings (A) 350 mm × 350 mm, (B) 250 mm × 250 mm, (C) 150 mm × 150 mm, and (D) 80 mm × 80 mm.

3.1 Layers construction and load testing

Concrete block pavement comes with different blocks sizes and shapes, and laying pattern. Individual block is seated on a levelled layer of graded sand before uniformly compacting the surface with vibrating compactor. Base and subgrade are constructed similar to the conventional pavements.

3.1.1 Foundation

River soil is compacted in 10 layers to a total depth of 1300 mm, in which each soil layer is compacted in lifts (loose lift thickness ≤ 250 mm), achieving the in-situ density (≥ 95% of laboratory maximum dry density) and water content (2% ≤ w ≤ 1%) as per MoRTH requirements (MoRTH 2013). Atop the embankment, the subgrade is a mechanical stabilised soil, constituting manufactured sand and silty soil in percentage proportion 60:40. The subgrade is compacted in 5 layers to a total thickness of 748 mm and achieving the MoRTH requirements (MoRTH 2013) for in-situ density (≥ 97% of laboratory maximum dry density) and water content (2% ≤ w ≤ 1%). **Figure 3.9** shows vibratory compaction of the foundation material and for every compacted layer density is checked by sand replacement method (BIS 1974).

(A) (B)

Figure 3.9: Construction of the foundation: (A) compaction (B) density check

3.1.2 Base

Base layer is compacted to an average thickness of 338 mm in two lifts (recommended lifts ranging 75-250 mm), and achieving minimum 98% of the maximum dry density and water content adjusted within ± 2 % from optimum content (IRC 2015; MoRTH 2013).

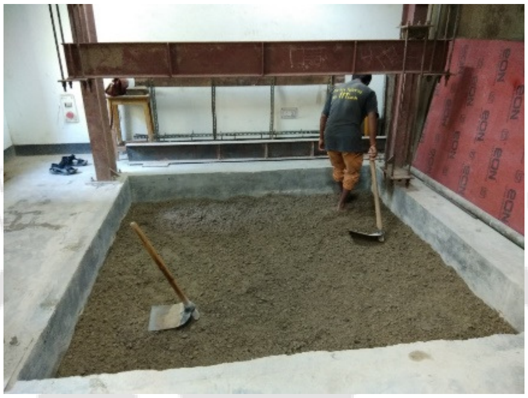

Figure 3.10: Laying of the base material

3.1.3 ICBP

Not making the bedding sand a correction for base surface unevenness, the surface level of base is levelled to a profile variation within a tolerance of ± 20 mm (MoRTH 2013). Thereafter, following IRC guidelines of bedding layer preparation, bedding sand is loosely spread to a 25-50 mm thickness and controlled by screed guides along the path such that the final compacted level is catered to a final design level. As per construction of bedding layer, sand is evenly spread out to a loose thickness of about 30-50 mm and blocks are compacted onto it to achieve an expected compacted bedding depth of 25-40 mm (IRC 2004). The level of compaction that is recommended such that the bedding layer reduces in thickness, is approximately a densification of 50 % to 80 % relative to loose sand density. Unlike the underlying pavement layers, the level of compaction is not specified to achieve a targeted density. Therefore, to present a uniform construction of bedding layer for all the pavement sections that the study is including, the densest density for a 40 mm compacted thickness is considered. The quantity of bedding sand that is to be filled into the test pit is the weight that if compacted to a 100% of maximum dry density, the thickness is 40 mm.

It is also essential that water content of sand be neither too dry nor wet because moisture content of the sand influences the sand workability during compaction. Indian Road Congress specified a 6-8% water content (IRC 2004, 2018a). In the densest condition of sand, the particles are closely packed with a maximum particle contact and this is achieved as maximum dry density at optimum water content (OMC). Therefore, for maximal workability, maximum dry density and OMC are considered for the bedding sand.

The sand is spread loosely into a uniform layer and avoiding anyone stepping on it. Supposedly, the sand is subsequently compacted with plate vibrators. However, in present study, the blocks are directly placed and lightly tapped onto the sand surface, thereafter a plate compactor is run on the block surface bedding sand and jointing sand compaction. The reason in which pre-compaction of bedding layer prior block placement is avoided due to two reasons:

a. Compaction within the test pit engages running the plate vibrator in circles and diagonally across the test pit surface. There is differential settlement because the machine pushes materials around rather than uniformly compacting the material under its base.
b. Attempting to compact the sand into a uniform bed results in moisture loss from the material.

There is four pavement sections with five different bedding layers, i.e., unconfined bedding layer, and confined bedding layer with geocell of openings 350 mm × 350 mm, 250 mm × 250 mm, 150 mm × 150 mm and 80 mm × 80 mm. The first pavement section taken is with confined bedding layer with geocell 150 mm × 150 mm. As shown in **Figure 3.11**, the geocells are spread out and placed with a cell centrally located in alignment with respect to centre of test pit. **Figure 3.12** shows hand-mixing material for the bedding layer using shovels, prongs and hoes, while adding water to a content additional of optimum content to counter water loss during mixing, laying and spreading. For unconfined layer, sand is screed out evenly, while as seen in **Figure 3.13**, moist sand quantity is calculated before pouring into each cell. After filling in the material into the pit, material is screed to level using a straight wooden block as shown in **Figure 3.14**.

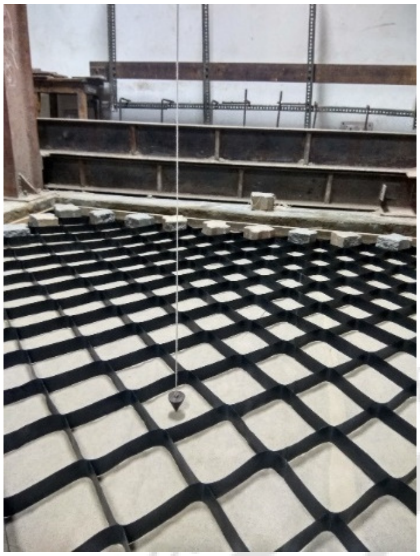

Figure 3.11: Alignment of geocell

Figure 3.12: Hand mixing of bedding sand

Figure 3.13: Filling in bedding sand

Figure 3.14: Leveling bedding layer

Figure 3.15: Block arrangement

Figure 3.16: Compaction on ICBP

Atop the loose sand, blocks are placed taking care of the joint width that blocks are neither tightly butted against each other that may cause block edges spalling nor too wide for blocks interaction during compaction. The Category A blocks are arranged in 90˚ herringbone pattern in reference to the test pit walls, and the arrangement is fixed by starting from the same corner for every section (See **Figure 3.15**). As seen in **Figure 3.16**, plyboard sheets covering the whole test area is used for initial compaction such that the blocks are not differentially compacted that can lead to a non-uniform bedding sand density. 15 rounds of compaction each in circular and diagonal direction is required to reach the possible maximum compaction level. At regular intervals the level of surface is checked by using a Vernier callipers (See **Figure 3.17**) and compaction is continued till the 15th round, when block edges start chipping and spalling even before achieving targeted 40 mm thickness. As observed with geocell opening 150 mm × 150 mm, the small geocell opening inhibits easy flow of sand into the cells, and instead excessively stressing the blocks, causing them to chip along the edges and corners.

A uniform compaction over the surface is followed attempting to maintain an even surface and uniform 2.0 - 4.0 mm joint width. After complete rounds given, joints are measured using a Vernier callipers (See **Figure 3.18**). The joint widths are measured at locations selected after generating random coordinates. One corner of the test area is fixed as the origin of coordinates, after which two axis values are randomly generated and the point is located on the surface. 15 points are located for each surface. Thereafter, dry jointing sand is brushed into the gaps and two additional rounds of compaction is continued (See **Figure 3.19**).

As seen in **Figure 3.20**, density of the compacted bedding layer using the sand replacement method, is tested at locations that are randomly selected. Compacting the bedding sand into geocells with smaller openings proves challenging, contributing to the exacerbation of block failures in pursuit of surface settlement. Considering the compaction challenges, the geocell with 80 mm × 80 mm openings is omitted from the study.

Figure 3.17: Surface Profile checking

Figure 3.18: Joint width measurement

Figure 3.19: Jointing sand filling

(A) **(B)**

Figure 3.20: Bedding layer density determination (BIS 1974): (A) Sand Pouring cylinder, and (B) test spots

3.1.4 Load Test

The experimental investigation of pavement sections is conducted in in-house testing facility, consisting of a 2.5 m × 2.5 m × 2.5 m test pit, and a loading structure of a 50 kN reaction frame. Loading is applied onto a 17 mm thick and 300 mm diameter rigid metal plate, using a 100kN hydraulic pump. Load is read out from a proving ring that is placed in between loading plate and hydraulic pump. Surface deformation measured using plunger type dial gauges, is taken at distances radially from the loading centre, i.e., plate centre, at 150 mm, 300 mm, 600 mm, 900 mm and 1200 mm on either side of plate. The dial gauges are fixed onto a girder that is rested on the floor, taking precautions that the dial gauges are in close proximity to the loading centreline and avoiding contacting the loading frame. ICBP is prepared in the test pit consisting of subgrade, base, bedding layer, concrete blocks and jointing sand.

Plate load test is also conducted on the granular layers and ICBP with arrangement as shown in **Figure 3.21** and **Figure 3.22** respectively. The aim of plate load test on the support layer surfaces is to determine the material properties of each layer from in-situ tests. The maximum loads for the plate load test on the base and foundation surfaces are predicted based on the vertical stress reaching each surface when a 40 kN load is imposed on the pavement surface.

The stresses reaching the underlying layers are computed using the MEPDG tool, IITPAVE, specifically designed for flexible pavement design. To assess the layer's response to this stress level, a load is directly applied to a circular, rigid plate with a diameter of 300 mm, positioned on the layer. To achieve a static loading condition, plate load test is carried on the base with gradual application of 27.28 kN load. Although the estimated load to be applied onto the foundation is less than 10 kN, however, the given load here is 30 kN. Plate load test is not conducted on the embankment due to limiting depth where the reaction frame can be arranged.

Figure 3.21: Plate load test on a granular layer

Figure 3.22: Plate load test on ICBP

Structural capacity of pavement layers is conducted using static plate load test. A load equal to half the standard axle load on dual wheels, i.e., 40 kN is applied onto a loading plate, that is placed on the pavement layer surfaces of ICBP. The load is slowly and gradually applied until the fixed peak load is reached. Peak loads for plate load test on base and subgrade surfaces are estimated from vertical pressure reaching their surfaces respectively when a 40 kN load is applied to the pavement surface.

Chapter 4. Numerical Analysis

4.1 General

The upcoming sections will delve into specific numerical techniques adopted in this study, illustrating their relevance and efficacy to bridge theoretical constructs and practical implementation. The goal is not only to offer a thorough understanding of these methods but also to highlight the wider impact of numerical analysis in advancing knowledge and application in the present study.

4.2 Analysis details

Two FEA schemes are implemented using the Abaqus/CAE software, in which the implicit and explicit analysis are engaged. Load given during plate load test in test pit sections, is applied gradually, in which it can be assumed as static loading in computational simulation. For such an experimental loading condition, an implicit structural analysis of the pavement system is suitable. The flowchart of the implicit analysis is shown in **Figure 4.2**. It begins with the geometry description, in terms of 3D or 2D part and for each material property is defined according to the mechanical constitutive theories required. Prior to load application, the layers mechanically interact according to the normal and tangential interaction behavior or relative constraint of motion defined. The outer surface of the layers is constrained against bulging to imitate the containment of the material within the test pit.

For foundation and base-foundation simulation, static analysis using implicit solver is engaged. The simulation is run for the period of 0.1 second and run in maximum increment steps of 100, with each increment timing at minimum of 1×10^{-20} second and maximum of 0.1 second. The analysis is run till the solution is converged by the system and outputs are written. The simulation outputs are then compared with the experimental response of the pavement system. Once the solution converged within acceptable limits, the FEM model is assumed predictable of the in-situ model.

It is encountered that with the ICBP sections consisting of all the layers encounter convergence problems. The reason may be due to contact nonlinearity at the surface layer. contact linearity can be caused by numerous contacting regions within the layer, that it results in complicated solution which implicit analysis cannot execute. Since, debugging with implicit solver did not resolve to execute solutions, therefore, the pavement system is analysed in explicit approach.

In explicit analysis, to execute a static loading condition, the simulation is targeted for a quasi-static condition. The flowchart of computational simulation in Abaqus/CAE for an explicit analysis is shown in **Figure 4.3**. Referring the flowchart, solution convergence through the earlier adopted solver of implicit analysis is not accomplished, which therefore, requires a bypass for iteration using an explicit solver.

Quasi-static condition is achieved in explicit analysis under the energy balance throughout most of the analysis such that kinetic energy of the deforming system shall not exceed 1-5 % of its internal energy. The energy balance for the simulation has been verified and plotted as shown in **Figure 4.1**.

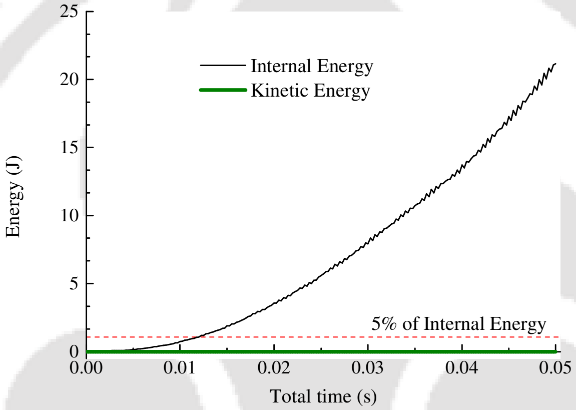

Figure 4.1: Energy balance for quasi-static analysis

For explicit analysis, three factors are improved such that the simulation is achieved the quasi-static condition, and they are simulation period, mass scaling and loading rate. Including a technique to attain quasi-static condition during analysis of ICBP sections, arbitrary frequency variations of load is to be given throughout a simulation. To increase the stability of simulation at each time increment, the material density of the jointing sand model is artificially increased by a factor of 100 such that to achieve the minimum target time increment of 1×10^{-6} second. Along with the former factors, the period is essential such that within this total time, solution converges. The time such that the quasi-static condition is achieved for ICBP sections without and with geocells in the bedding layer is set at 0.04 second and 0.05 second, for ICBP with unconfined and confined bedding layer respectively. The outputs written are compared with experimental responses and executed once results are acceptable, otherwise the model definition is iterated till desired results are achieved.

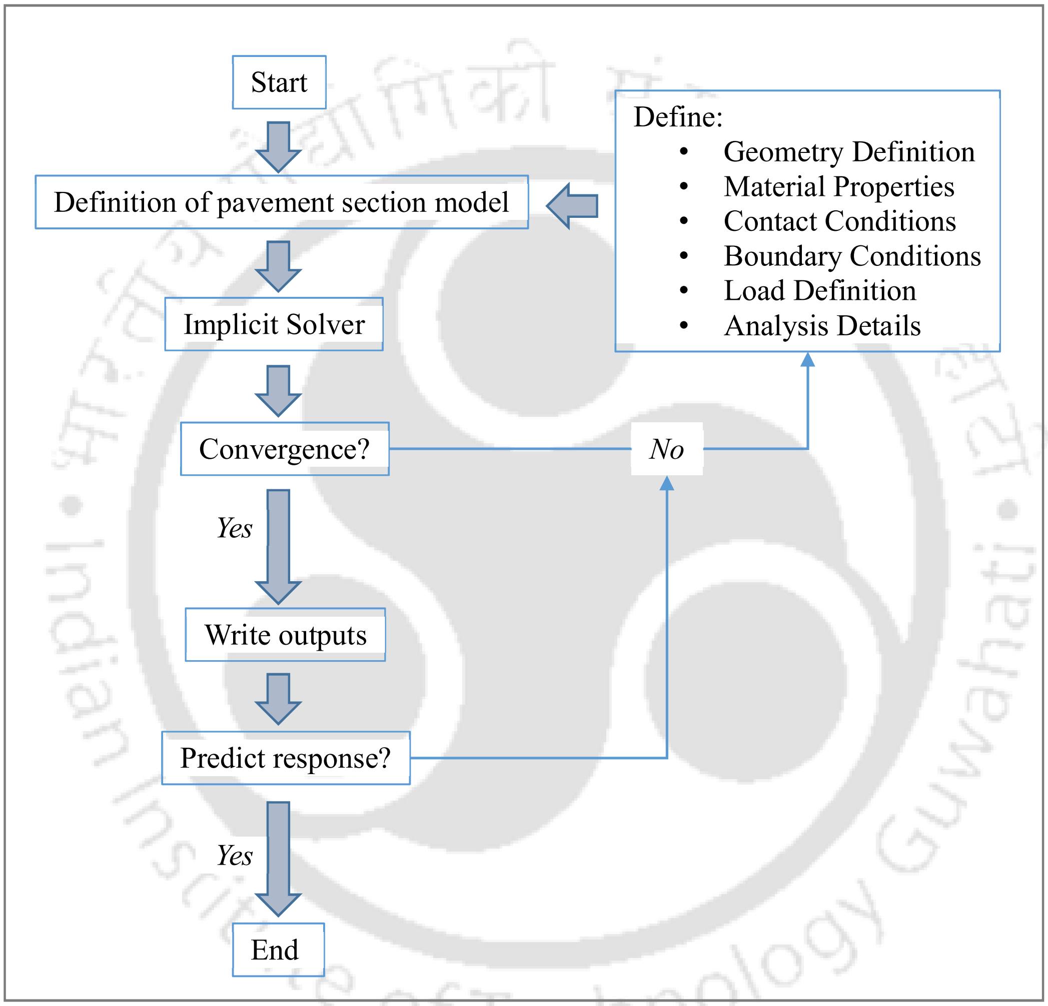

Figure 4.2: Flowchart of FEA for static analysis

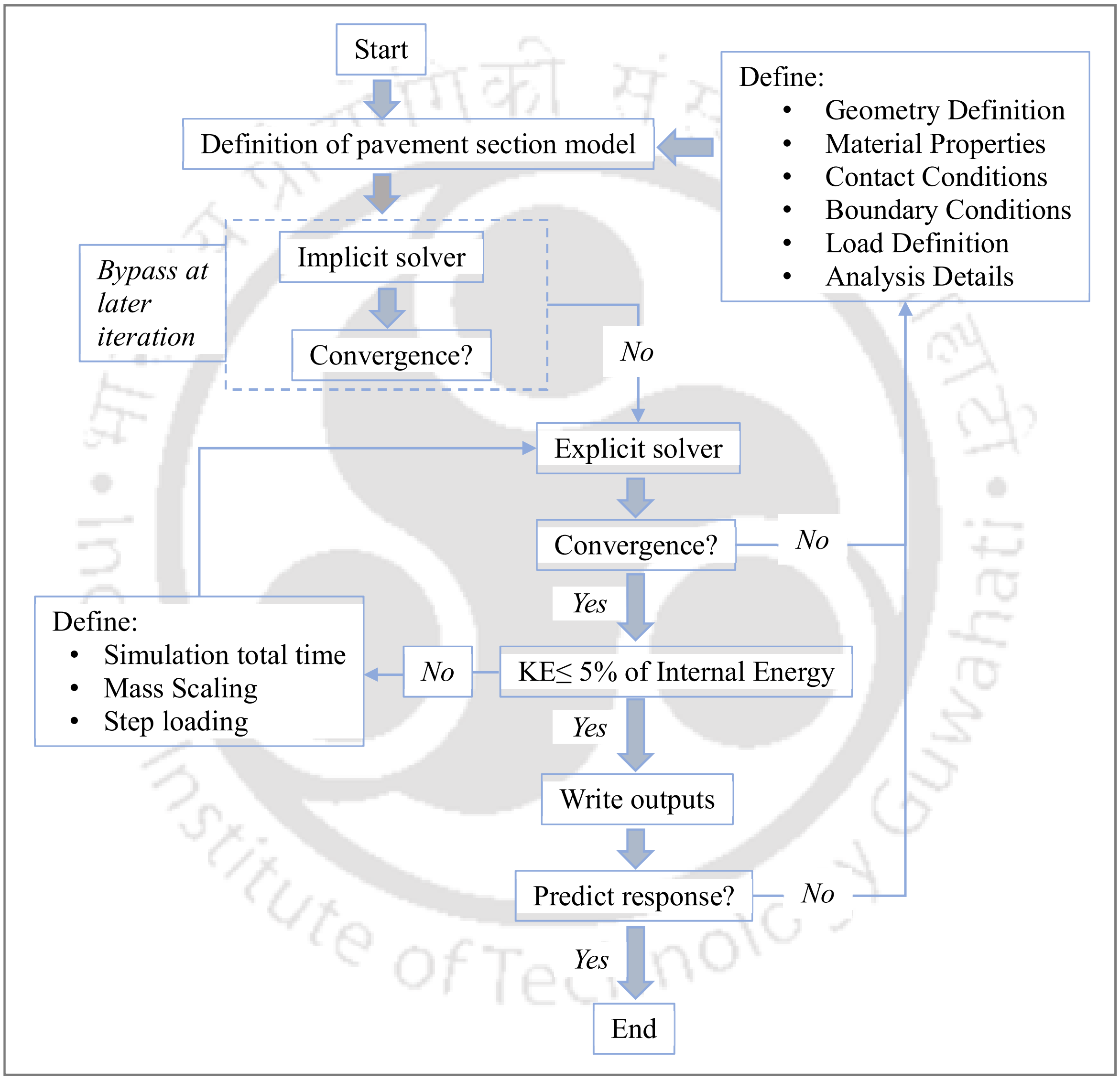

Figure 4.3: Flowchart of FEA for quasi-static analysis

4.3 Micromechanical analysis for homogenisation

The initial step prior to replacement of the composite ICBP surface with a homogenised layer is customising the fundamental volume of the composite, i.e., the Representative Volume Element (RVE). At a macroscopic level (or whole part), the heterogeneous structure of the composite material is represented by a homogeneous medium with aeolotropic properties. Therefore, it is presumed the RVE phases of inclusion and matrix, are isotropic, uniform, and homogeneous in themselves. This makes the stress and strains through the composite minutely inhomogeneous, irrespective of the external loading. Hence, the representative volume of composite sample is chosen containing enough inclusions such the equivalent material properties represent the composite layer at a large scale size. Appropriate boundary conditions are applied such that equivalent material properties are computed. To begin with, the shape and size of the RVE directly influence the behaviour of the overall structure. Therefore, the shape of the RVE is chosen as a structure with periodic boundary conditions such that it is a generic structure that can be repeatedly assembled in space. Such that the strain field of the bounded RVE domain is macroscopically compatible, it is subjected to either uniform displacement boundary condition (KUBC) or uniform traction boundary condition (SUBC). The homogenised elasticity tensor of the volume element is then executed.

4.3.1 Generation of RVE and equivalent properties

The homogenisation approach for composite materials at the microscale/ constituent level involves micromechanics, which is the study of the mechanical behaviour of individual constituents of the composite material, *viz.*, inclusion and matrix. An Abaqus/CAE plug-in, *Micromechanics* (Simulia 2022) is considered for mechanical study of the composite at its fundamental level and execute the effective/ equivalent response. This is achieved by analysing a unit periodic cell that replicates the overall behaviour of the whole part, along with its components. The unit periodic cell, also called Representative Volume Element (RVE) is defined as the smallest material volume with an equivalent constitutive response. It also requires the RVE is a periodic structure such that this generic structure selected can be assembled repeatedly in space.

The 90° herringbone pattern has a complex arrangement of the constituents and the axis of symmetry is diagonal to the whole surface. Therefore, choosing the RVE for a surface where blocks are arranged at 90° herringbone pattern requires that periodic boundary condition can be applied. Primarily, the aim of choosing the RVE for the ICBP surface should be the periodic cell be small enough to consist sufficient blocks and jointing sand volume, such that the equivalent material properties that will be calculated will predict the behaviour of the homogenised part similar to the composite part (Beran 1965; Hill 1965). Moreover, RVE size should not be too large that it does not exhibit statistical homogeneity (Böhm et al. 2010; Drugan and Willis 1996; Hashin 1983; Shahzamanian et al. 2022). Therefore, after diligent exploration, the RVE of the surface layer of the ICBP considered in the present study is **Figure 4.4**.

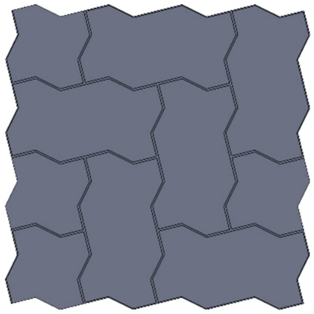

Figure 4.4: RVE of the ICBP surface layer

The RVE is subjected to uniform strain gradient boundary conditions. Subsequently, employing mean field homogenisation, the composite's equivalent properties are determined.

4.4 Analysis of ICBP with homogenised part

The complexity of rendering and assembling the concrete blocks to a required pattern can be eliminated by homogenising the layer material properties, with a motive that the complex composite geometry can be replaced by a uniform and orthotropic layer as shown in **Figure 4.5**.

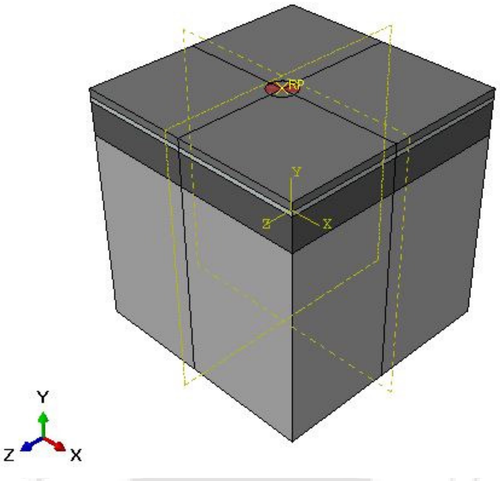

Figure 4.5: ICBP assembly with homogenised surface layer

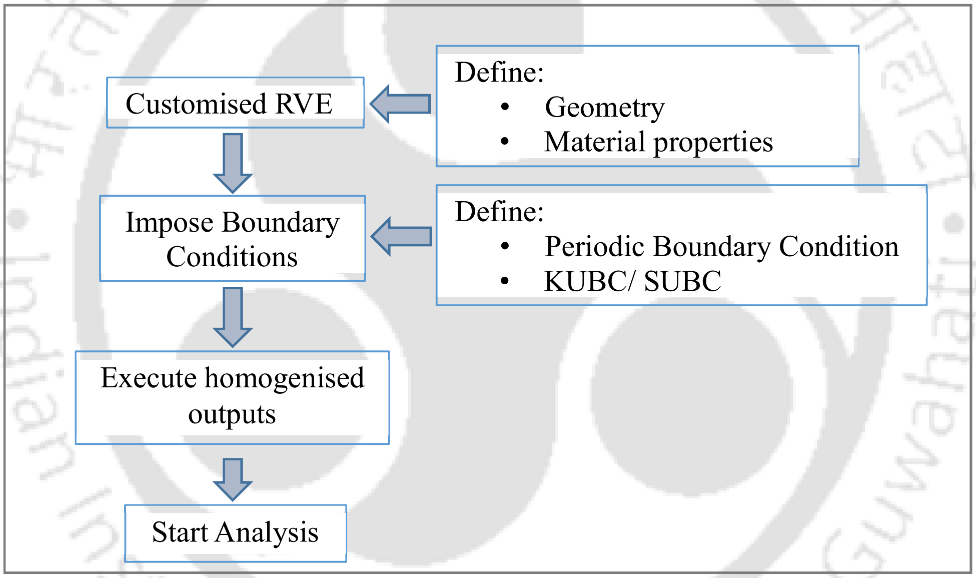

Figure 4.6: Flowchart of *Micromechanics* homogenisation (Simulia 2022)

The homogenisation of the composite to a simpler, uniform, and homogeneous layer follows the steps as given in **Figure 4.6**. Hence after, the surface layer of the ICBP sections is replaced by the uniform layer possessing the executed equivalent material properties. Such sections are then set up for pavement structural analysis, either with implicit or explicit type. For the present ICBP section, even with homogenised surface layer, explicit analysis conducted to achieve quasi-static conditions. However, the benefits are besides encountering less convergence problems due to meshing and contact errors, the primary benefit of homogenisation is shorter simulation clock-time, eventually cutting simulation cost.

4.5 Material Properties Idealisation

The material properties are adopted accordingly according to actual values or determined in laboratory. Concrete grade used for casting blocks is M40. The elastic modulus of blocks (E_c) is determined by Equation (**4.1**) which is derived from its relationship with the characteristic cube compressive strength of concrete (f_{ck})

$$E_c = 5700\sqrt{f_{ck}} \text{ (BIS 2000)} \qquad \textbf{(4.1)}$$

Density of block is achieved from its weight per volume, for which its volume is achieved by rendering. Both base and foundation densities are taken to the maximum bulk density values. Density of foundation is taken as a weighted value with respect to their depths. The sand in the joints is assumed to be fully compacted to their maximum density in dry condition. For simulation, the relative density of all bedding layers is taken as an average of 78.09% relative to the maximum dry density. The Poisson's ratios are considered from recommended values of Huang (2009). **Table 4.1** lists the material properties of the layers of the simulated ICBP.

Table 4.1: Part material properties

Loading Plate:	
Type	Rigid body
Mass	24.4 kg
Rotary Inertia	I_{xx} = 538.385 tonne-mm^2 and I_{yy} =I_{zz} = 271.498 tonne-mm^2
Concrete Blocks:	
Type	Deformable, elastic
Density	1.992 g/cm^3
Elastic Modulus	31622.7766 MPa
Poisson's ratio (v)	0.15
Jointing Sand:	
Type	Deformable, elasto-plastic (Mohr-Coulomb criterion)
Density	1.699 g/cm^3
Secant Modulus (E) determined at 50% the peak deviator stress	30.48 MPa
Angle of internal friction (ϕ)	40°
Cohesion (c)	Cohesionless
Dilation angle (ψ)	10°
Poisson's ratio (v)	0.3
Bedding Sand for unconfined bedding layer:	
Type	Deformable, elasto-plastic (Mohr-Coulomb criterion)
Bulk Density	1.7015 g/cm^3
Secant Modulus (E) determined at 50% the peak deviator stress	18.85 MPa

Angle of internal friction (ϕ)	34°
Cohesion (c)	Cohesionless
Dilation angle (ψ)	4°
Poisson's ratio (v)	0.23
Base	
Type	Deformable, elastic
Bulk Density	2.338 g/cm^3
Elastic Modulus	147.20 MPa
Poisson's ratio (v)	0.35
Foundation	
Type	Deformable, elastic
Bulk Density	1.8837 g/cm^3
Elastic Modulus	57.10 MPa
Poisson's ratio (v)	0.35

Bedding and jointing sands are considered as elastoplastic material with the elastic part being linearly elastic and plastic portion following Mohr-Coulomb criterion. The parameters of shear test are secant modulus of elasticity, angle of internal friction, cohesion value and dilation angle, which are determined after an unconsolidated-undrained triaxial test (BIS 2002). During permanent deformation, the plastic flow potential Deviatoric eccentricity for elliptical flow potential is calculated, $e_d = \frac{3-\sin\phi}{3+\sin\phi}$ (Menetrey and Willam 1995) and meridional eccentricity (e_m) of hyperbolic flow potential in the meridional plane is taken as a constant value of 0.1 (Simulia 2021; Superczyńska et al. 2016).

The generated equivalent properties of a homogenised surface layer, which include density and elastic properties are listed in **Table 4.2**.

Table 4.2: Properties of the homogenised ICBP surface layer

Properties	Value
Elastic Moduli	
E_{11}	15.747 MPa
E_{22}	14.598 MPa
E_{33}	27948.008 MPa
Shear Moduli	
G_{12}	6.124 MPa
G_{23}	10.033 MPa
G_{13}	8.678 MPa
Poisson's ratios	
v_{12}	-0.099
v_{23}	8.041 E-05
v_{13}	8.659 E-05

Equivalent density	1.763 g/cm^3

4.6 Model Geometry

All the layers are compacted within the area of 2500 mm × 2500 mm with varying depths considered from test pit measurement. During simulation of foundation and base-foundation systems, there is symmetry of the material volume about the loading center, which is also the centerline of the pit, therefore, a quarter of the full section is a model considered. The quarter volume of the foundation model and base-foundation model is illustrated in **Figure 4.7 (A)** and **(B)** respectively.

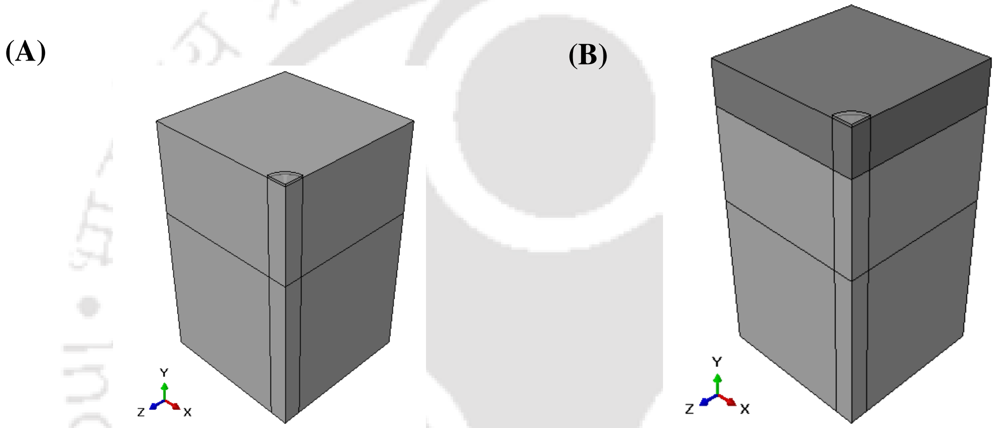

Figure 4.7: Assembly of (A) Foundation, and (B) Base-Foundation

For validation of foundation model only, the lateral boundaries of the foundation are expanded to 6.0 m from test pit center, and thickness is deepened to 6.0 m. In the case of base-foundation validation model, on this enlarged foundation, a base of same area but fixed thickness of 338 mm is laid. **Figure 4.8** shows the base and foundation layers enlarged to the desired size suitable for validation.

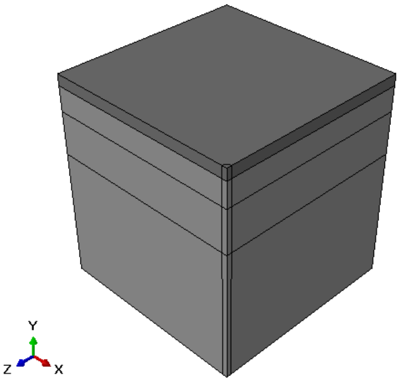

Figure 4.8: Validation model of the base-foundation

All granular strata of the ICBP, i.e., base and foundation, as shown in **Figure 4.9 (A)** and **(B)** respectively, are considered deformable and modelled as continuous layers. The loading plate is a very stiff part and is modelled as a rigid shell, whose body motion is defined at a reference node located at its center. Even though concrete of the blocks is comparatively and exceedingly stiffer than granular materials of the pavement, the blocks are considered deformable with very high stiffness value. Ignoring the principal advantage of representing the blocks as rigid bodies for computational efficiency, it is because calculation of moment of inertia for the block regarding its shape, size and orientation is arduous.

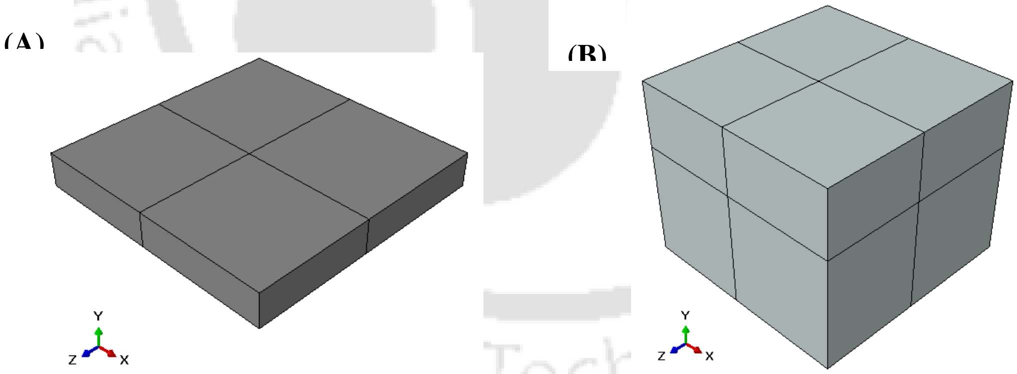

Figure 4.9: Geometric parts of (A) Base, and (B) Foundation

However, with respect to the blocks that are arranged in the 90˚ herringbone pattern, the surface cannot be sectioned into symmetrical fragments. Hence, the ICBP sections are modelled to the full size as shown in **Figure 4.10**.

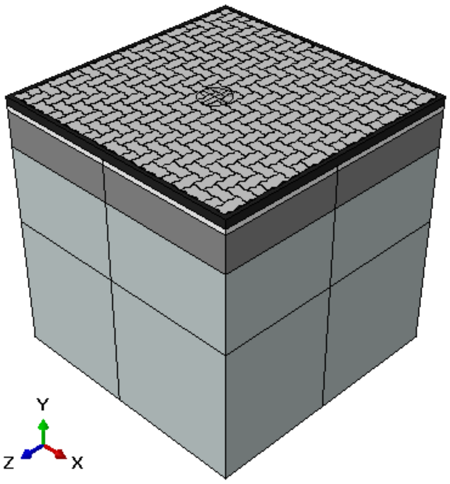

Figure 4.10: ICBP assembly with actual surface parts

The loading plate (**Figure 4.11 (A)**) is a circular shell with a diameter of 300 mm. The block size is taken as measurement as shown in **Figure 4.11 (B)** and **Figure 4.11 (C)** with a height of 80.65 mm, without considering the chamfer height of 0.4 mm. Jointing sand is filled to a height of 80.25 mm, to reach where the block chamfer starts. The plan of a full-sized block is shown in **Figure 4.12**. Volume of a single block is taken by multiplying the area of the plan area with the total height, without taking chamfer reduction. Area of block is obtained from rendered model.

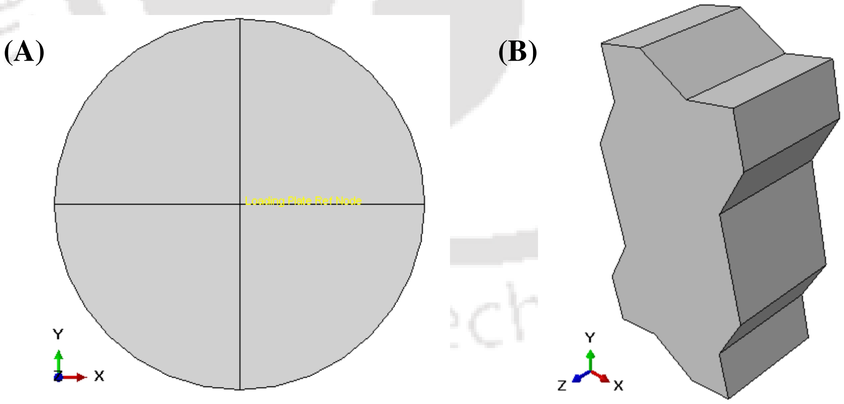

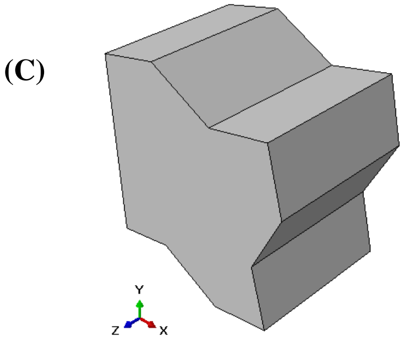

Figure 4.11: Model of (A) Loading plate, (B) Full-sized block, and (C) Trimmed block

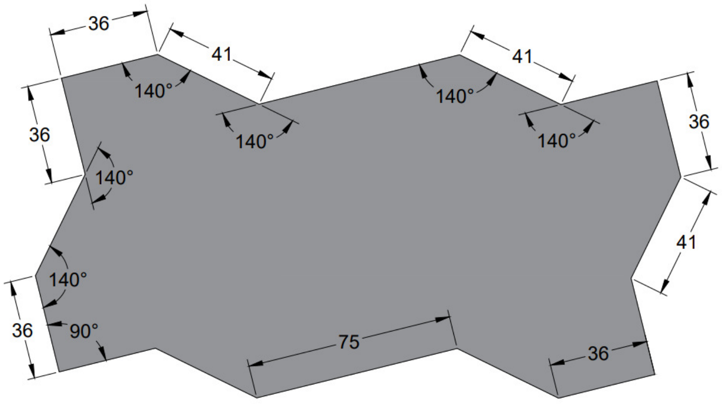

Figure 4.12: Plan of concrete block model

Jointing sand is a continuous bed as shown in **Figure 4.13 (A)**, that occupies the gaps between the blocks and the test pit boundary walls. Bedding layer, with and without geocells are considered a uniform and homogeneous layer, as shown in **Figure 4.13 (B)**. The measured thicknesses of the bedding layer, for which they are considered in the model, are 48.95 mm for unconfined bedding layer and 49.35 mm, 51.5 mm, and 54.7 mm, for confined bedding layer with geocell sizes 350 mm × 350 mm, 250 mm × 250 mm and 150 mm × 150 mm, respectively.

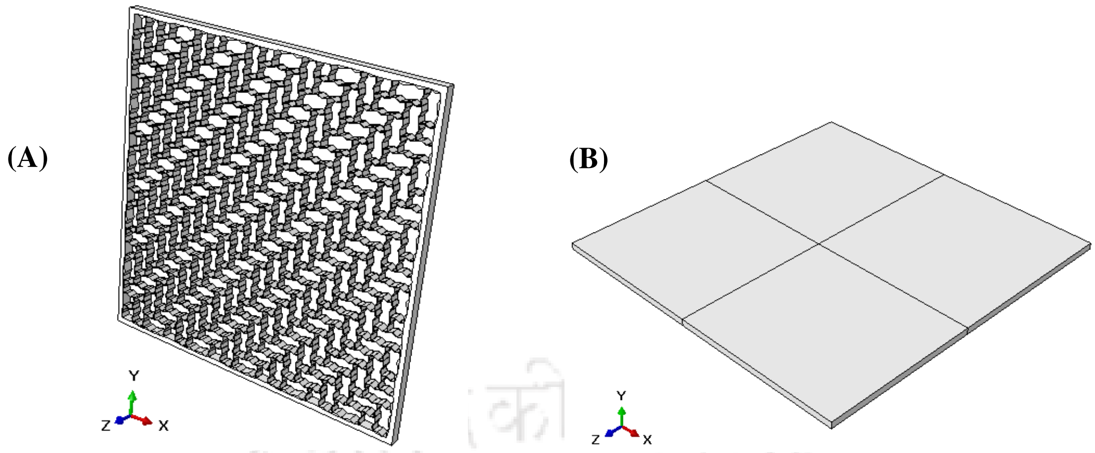

Figure 4.13:Geometric model of (A) Jointing sand and (B) Bedding layer

ICBP sections with homogenised surface layer, shown in **Figure 4.14 (A)**, in which the surface layer is replaced by the homogenised layer (**Figure 4.14 (B)**) while all underlying layers are like the ICBP with actual surface layer.

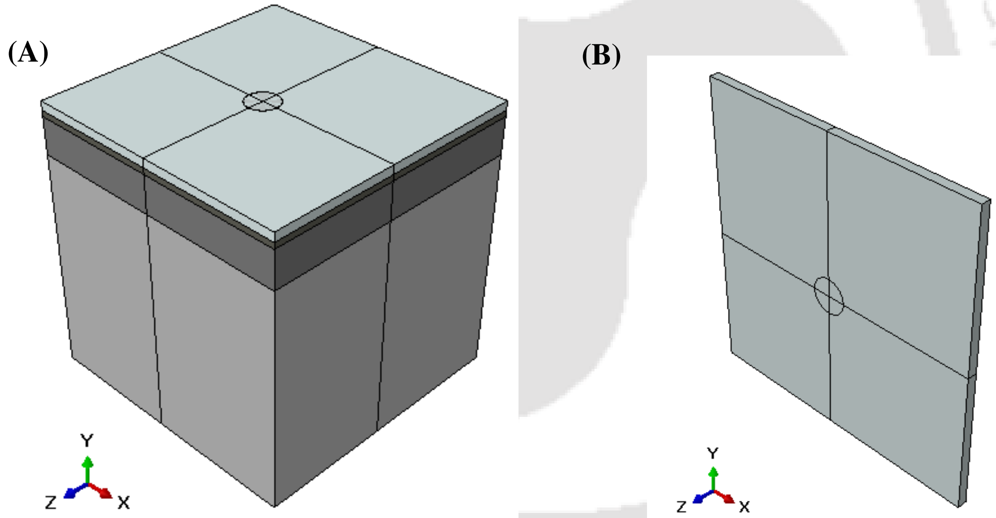

Figure 4.14: (A) ICBP with homogenised surface, and (B) Homogenised surface layer

4.6.1 Mesh detail

The fundamental aspect of FEM is discretisation of the complex and large geometries into a set of simple, interconnected elements. The accuracy and reliability of FEM simulation is directly affected by the element type, mesh size, and element quality. Currently, the choice of element type is based upon the geometrical dimension (1D, 2D or 3D) and element order (Linear element or quadratic element). The selection of the element type and mesh size for the present models is guided by the geometry dimension of the structure's part, types of analysis and solution convergence. The resolution of the FEM model and its level of accuracy can be increased by *h*- and *p*-refinements of the elements. To achieve accuracy, *h*-refinement discretizes the region into many elements while higher degree shape functions are used in *p*-refinement.

While for quality, the mesh is verified for the criteria and fitness check according to the values mentioned in **Table 4.3**.

Table 4.3: Mesh quality criteria

Selection Criterion	Hexahedral element	Quadrilateral element	Triangular element	Tetrahedral element	Wedge element
Smaller face corner angle	10°	10°	5°	5°	10°
Larger face corner angle	160°	160°	170°	170°	160°
Aspect ratio	10	10	10	10	10
Short edge	0.01 mm	0.01 mm	0.01 mm	0.01 mm	0.01 mm
Shape factor	N/A	N/A	0.01	0.0001	N/A

The 3D parts of the ICBP model are commonly modelled with hexahedral elements. However, blocks that consist of many sharp corners encounter inconsistent element related errors, and for which the domain is meshed with wedge elements. The loading plate modelled as a rigid part is meshed with shell rigid elements. Mesh details regarding the three models, i.e., foundation, base- subgrade and ICBP sections without and with geocell confinement are given in **Table 4.4** to **Table 4.8** respectively. **Table 4.4** and **Table 4.5** gives the mesh details of the foundation and base-foundation models respectively, for which iteration of foundation material and base material properties are conducted. **Table 4.6** shows the mesh details of the validation models of base-foundation and foundation. Finite elements of the foundation here, can be implemented with linear elements that have just a single integration point located at the element's centroid.

Table 4.4: Mesh detail of foundation model

Part	Element type	Element shape	No. of nodes	Geometric order	Element Name	Total no. of elements
Foundation	continuum	hexahedral	8	linear	C3D8	62826
Loading plate	rigid	quadrilateral	4	linear	R3D4	171
	rigid	triangular	3	linear	R3D3	18

Table 4.5: Mesh detail of base-foundation model

Part	Element type	Element shape	No. of nodes	Geometric order	Element Name	Total no. of elements
Base	continuum	hexahedral	8	linear	C3D8	28866
Foundation	continuum	hexahedral	8	linear	C3D8	62826
Loading plate	rigid	quadrilateral	4	linear	R3D4	158

Table 4.6: Mesh detail of foundation and base-foundation validation model

Part	Element type	Element shape	No. of nodes	Geometric order	Element Name	Total no. of elements
Base-foundation model						
Base	continuum	hexahedral	8	linear	C3D8	47580
Foundation	continuum	hexahedral	8	linear	C3D8R	172020
Foundation model						
Foundation	continuum	hexahedral	8	linear	C3D8R	172020

The density and distribution of elements throughout the foundation, base- foundation and base-foundation validation models can be visualised in **Figure 4.15 (A), (B)** and **(C)** respectively.

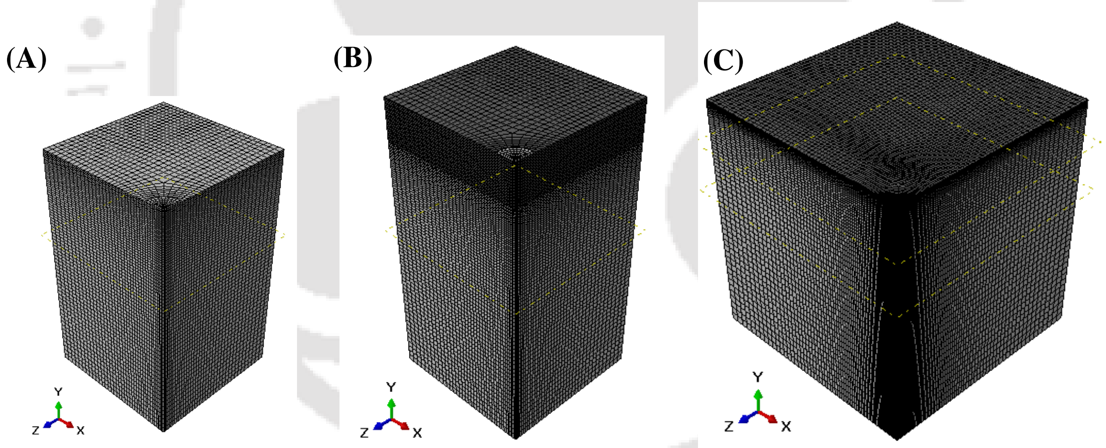

Figure 4.15: Meshes of (A) Foundation, (B) Base-Foundation, (C) Base-Foundation validation models

Meshing if the ICBP sections with actual surface layer are achieved upon an arduous effort of finding the mesh sizes that simulation solutions converge. However, for the sections with homogenised surface, meshing is done after mesh sensitivity check. **Table 4.7** gives mesh detail of the ICBP sections with actual surface that is laid on unconfined and confined bedding layer. Respectively, **Table 4.8** lists the mesh details of ICBP sections with a homogenised surface layer with unconfined bedding layer and confined bedding layer.

Table 4.7: Mesh detail of ICBP sections with actual surface layer

Part	Element type	Element shape	No. of nodes	Geometric order	Element Name	Total no. of elements
Blocks	continuum	hexahedral	8	linear	C3D8	4316
	continuum	wedge	6	linear	C3D6	22
Jointing sand	continuum	wedge	6	linear	C3D6	4567
Base	continuum	tetrahedral	10	quadratic	C3D10	9639
Foundation	continuum	tetrahedral	10	quadratic	C3D10	32855
Loading plate	rigid	quadrilateral	4	linear	R3D4	96
	rigid	triangular	3	linear	R3D3	32
Unconfined bedding layer						
Bedding layer	continuum	tetrahedral	10	quadratic	C3D10	10042
Confined bedding layer with geocell openings of						
350 mm × 350 mm	continuum	tetrahedral	10	quadratic	C3D10	9960
250 mm × 250 mm	continuum	tetrahedral	10	quadratic	C3D10	9986
150 mm × 150 mm	continuum	tetrahedral	10	quadratic	C3D10	14846

Table 4.8: Mesh detail of ICBP sections with homogenised surface layer with unconfined bedding layer

Part	Element type	Element shape	No. of nodes	Geometric order	Element Name	Total no. of elements
Unconfined bedding layer						
Surface layer	continuum	hexahedral	8	linear	C3D8	6798
	continuum	wedge	6	linear	C3D6	54
Base	continuum	hexahedral	8	linear	C3D8	26912
Foundation	continuum	hexahedral	8	linear	C3D8	161472
Loading plate	rigid	quadrilateral	4	linear	R3D4	324
	rigid	triangular	3	linear	R3D3	108
Bedding layer	continuum	hexahedral	8	linear	C3D8	3364
Confined bedding layer						
Surface layer	continuum	hexahedral	8	linear	C3D8	5120
	continuum	wedge	6	linear	C3D6	48
Base	continuum	hexahedral	8	linear	C3D8	17500
Foundation	continuum	hexahedral	8	linear	C3D8	102500
Loading plate	rigid	quadrilateral	4	linear	R3D4	288
	rigid	triangular	3	linear	R3D3	96
Bedding layer	continuum	hexahedral	8	linear	C3D8	2500

p- refinement of some parts of ICBP sections with actual surface layer is adopted such that solution converges. Simultaneously, simplifying the actual surface layer to a homogenised part reduces the complexity of meshing to execute the solution. As seen in **Figure 4.16 (A) and (B)**, the meshes adopted for each ICBP section type are considered to execute the simulation.

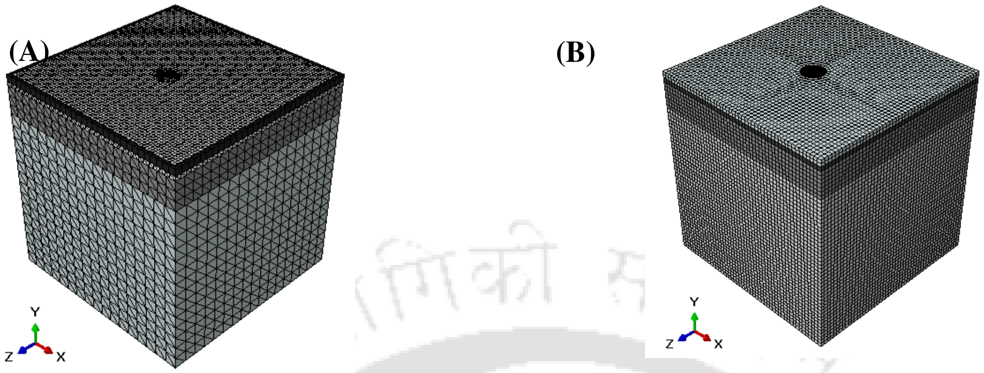

Figure 4.16: Meshes of ICBP sections with (A) Actual surface parts, (B) Homogenised surface layer

Detailed meshing of the parts of each of the ICBP sections, with actual surface layer and homogenised surface layer are given in **Figure 4.17** and **Figure 4.18** respectively.

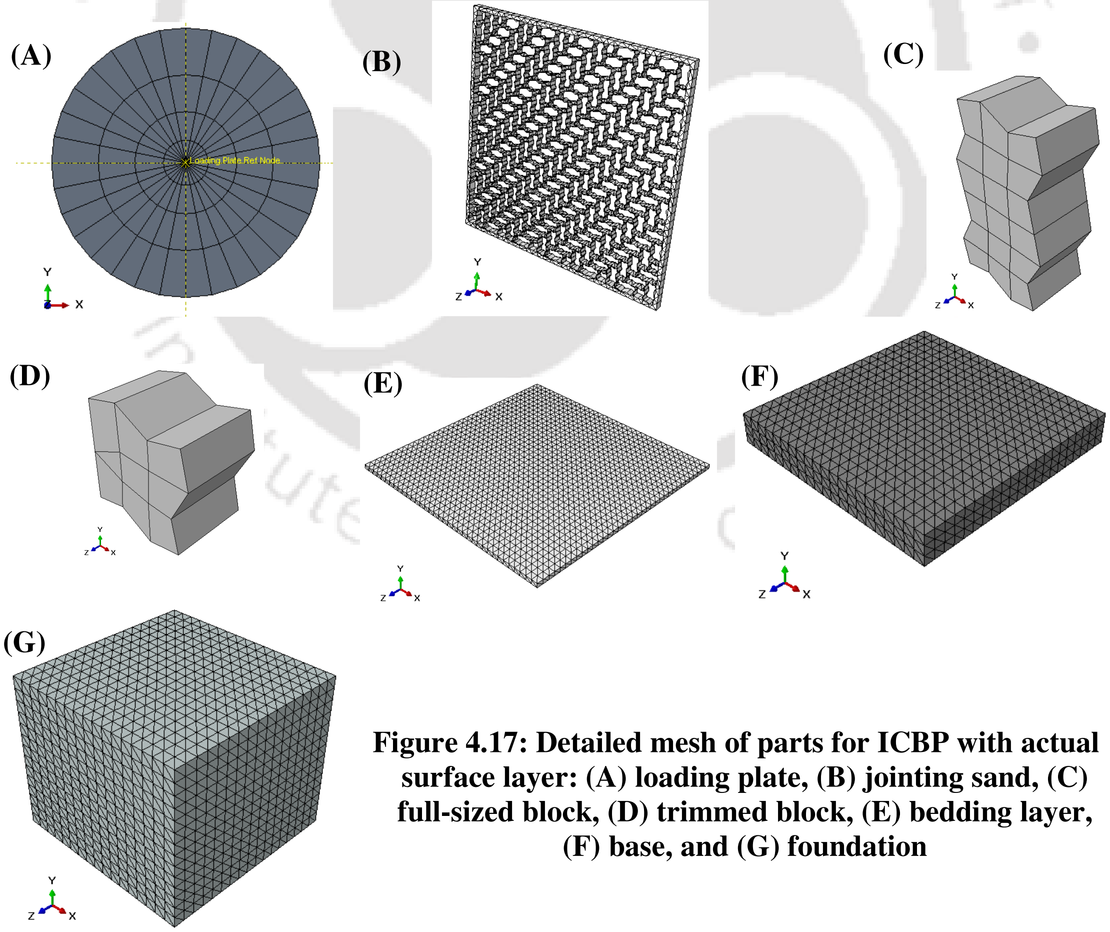

Figure 4.17: Detailed mesh of parts for ICBP with actual surface layer: (A) loading plate, (B) jointing sand, (C) full-sized block, (D) trimmed block, (E) bedding layer, (F) base, and (G) foundation

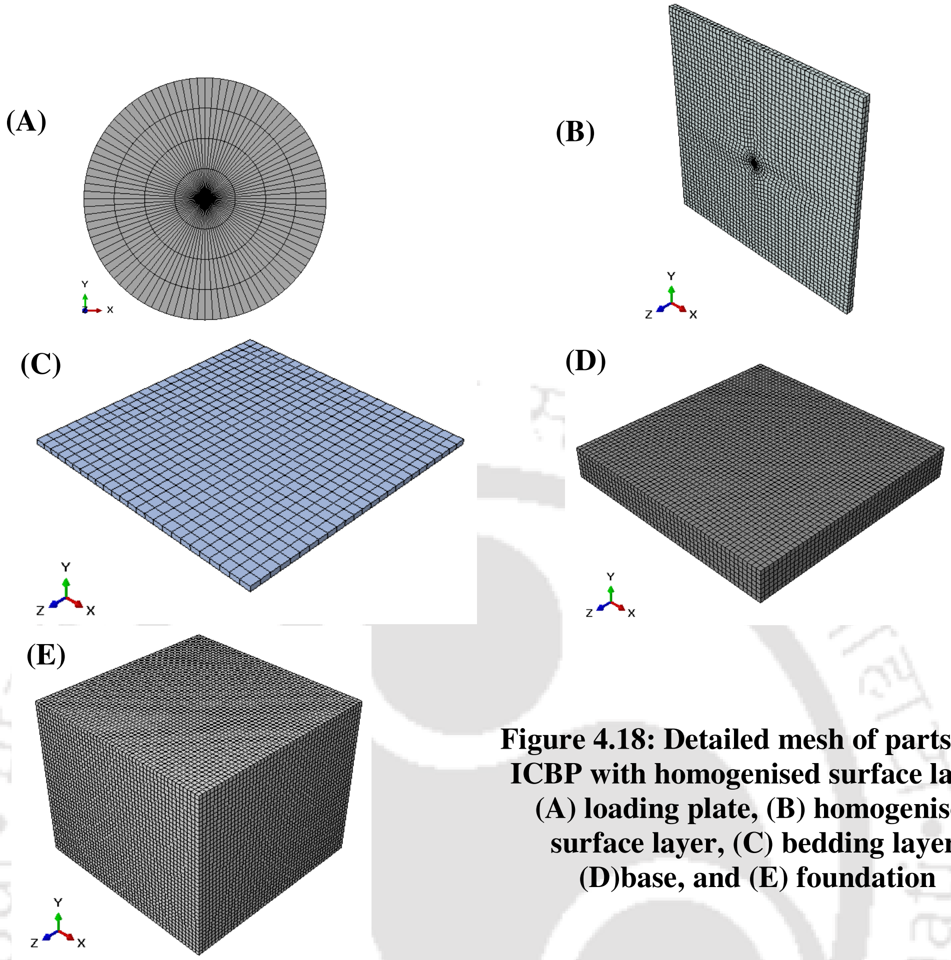

Figure 4.18: Detailed mesh of parts for ICBP with homogenised surface layer: (A) loading plate, (B) homogenised surface layer, (C) bedding layer, (D)base, and (E) foundation

4.6.1.1 Mesh sensitivity

Mesh sensitivity in foundation, base-foundation and ICBP sections is assessed by adjusting the mesh size and checked for sensitivity of the responses relative to mesh sizes. The meshes that have been listed in this section are considered after the sensitivity assessment. Results of mesh sensitivity test for the sections is discussed in Section **5.3.4**.

4.6.2 Interface Interaction

Interface interaction is implemented imitating practical situations, based on IRC recommendation and a reason for solution convergence. Following IRC assumptions that the layers of a flexible pavement are fully bonded (IRC 2018b), here subgrade and base are prevented from relative sliding. The interaction between the loading plate with the granular layers is assumed to be frictional with coefficient of friction, μ= 0.5. The frictional interaction is validated by calculating contact pressure $q(r)$ according to Equation (**4.2**) and FEM calculated values. is shown in **Figure 4.19**. The contact pressure between the two surfaces calculated by the two methods is plotted in **Figure 4.19**.

$$q(r) = \frac{pa}{2(a^2 - r^2)^{0.5}} \quad \text{(Huang 2009)} \qquad \mathbf{(4.2)}$$

Where, r is the distance from centre of plate to the point where pressure is measured and p is the average pressure applied, calculated as total load divided by contact area.

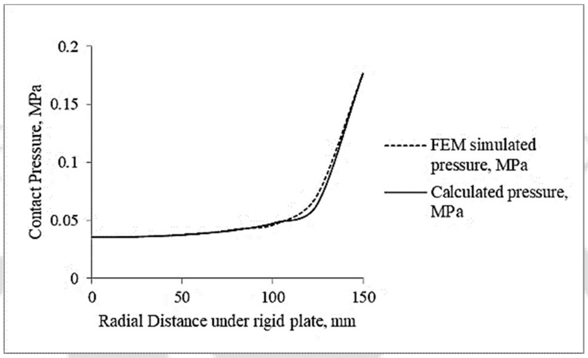

Figure 4.19: Validation of assumed frictional interface interaction

The interface frictional interaction between the parts of the ICBP sections are given in **Table 4.9**.

Table 4.9: Interface interaction

Layer-1	Layer-2	Interface interaction
ICBP with actual surface layer		
Base	Subgrade	Fully bonded
Base	Bedding layer	Fully bonded
Bedding layer	Jointing sand	$\mu = 0.25$
Block	Bedding layer	$\mu = 0.25$
Loading plate	Block	$\mu = 0.20$
Block	Jointing sand	Fully bonded
ICBP with homogenised surface layer		
Base	Subgrade	Fully bonded
Base	Bedding layer	Fully bonded
Homogenised surface	Bedding layer	$\mu = 0.25$
Loading plate	Homogenised surface	$\mu = 0.20$

The metallic loading plate and block surfaces experience lower frictional resistance compared to the granular layer, hence, frictional coefficient is taken a lesser value. In the upper layers of the ICBP section, which bear greater stress due to higher applied load, the interface, slippage at the interface will occur faster. For this reason, the frictional force resisting the motion of two surfaces in contact to the normal force pressing the two surfaces together is considered lesser. However, for the parts, blocks and jointing sand that are in the surface are not introduced to frictional interaction, but the interface is fully bonded, such that it only allows the jointing sand to encounter shear stress within its thickness. Moreover, for all interfaces, no layer material can penetrate each other.

4.7 Boundary conditions and Load Definition

Bottom of embankment touching the pit bottom is restrained against all movement, and the lateral walls of all layers are prevented from bulging out. Symmetry boundary conditions are applied onto the section surface of the foundation and base-foundation models. Load can either be applied as a uniform pressure onto the surface or a concentrated load acting at centre of the loading plate. Onto both the foundation and base-foundation surfaces, load is applied as a pressure distributed uniformly onto the circular loading plate. However, onto the ICBP sections, analysis works with a concentrated load applied vertically downwards at the loading plate centre. To attain quasi-static condition during analysis of ICBP sections, arbitrary amplitude/ frequency of load is implied throughout a simulation. In the case of ICBP with actual surface layer, load is gradually applied at 0.05 cumulative amplitude for every 0.002 second of the simulation step, while for ICBP with homogenised surface layer, the same amplitude is taken for every 0.0025 second.

4.8 Derivation of pavement response.

In stress analysis, Abaqus/CAE computes the fundamental response variables as the displacements of the nodes. Once these nodal displacements are identified, it becomes straightforward to determine the stresses and strains in each finite element. Consequently, to assess pavement response at specific locations, the variables are gathered from the nodes chosen within that region.

Chapter 5. Results

5.1 General

The chapter presents the entire findings from the study and is the product of substantial investigation and analysis. Results from research questions, tested hypotheses, or pursued objectives are presented in this important area. It analyses and interprets data in a systematic way with the goal of gleaning insights, seeing trends, and coming to reliable scientific findings. The value of raw data in the context of study aims is explained in depth by the subsections, which offer thorough explanations of the empirical evidence. These results advance the experimental understanding and open for more deliberations, conclusions, and suggestions.

5.2 Experimental findings

The experimental findings are divided into two categories: in-situ material testing and observation of experimental analyses. The goal of in-situ material evaluation is to confirm the construction's adherence to practical criteria. These tests include evaluating the density of granular layers such as embankment, subgrade, base, and bedding layers in-situ. Furthermore, the surface layer is examined to determine the uniformity of compaction, which is accomplished by checking the gap consistency between blocks. The in-situ density is determined after the sand replacement test in accordance with BIS guidelines (BIS 1974). Concurrently, experimental study findings from plate load tests on subgrade, base, and ICBP sections with different bedding layers have been documented.

5.2.1 In-situ material tests

The embankment is raised in lifts that are compacted to 10 layers, approximately of equal thickness (within 150-200 mm) to reach a total thickness of 1300 mm. Each layer of river soil is compacted to fulfil MoRTH criteria for density (≥ 95% of laboratory maximum dry density value of 1.613 g/cm^3) and water content ($2\% \leq w \leq 1\%$) (MoRTH 2013). **Table 5.1** shows the measured densities of the 10 layers, and the relative compacted density meeting the prescribed minimum density, with water content falling within the desired range around the optimal amount of 12.8 %.

Table 5.1: In-situ density of compacted embankment

Layer no. from top	In-situ ρ_d (g/cm^3)	*w* (%)	Relative density (%)	Difference of *w* from OMC (%)
1	1.550	13.4%	96	+0.6
2	1.569	13.9%	97	+1.1
3	1.554	13.5%	96	+0.7
4	1.548	13.1%	96	+0.3
5	1.574	10.9%	98	-1.9
6	1.559	11.1%	97	-1.7
7	1.563	12.4%	97	-0.4
8	1.568	11.5%	97	-1.3
9	1.544	11.9%	96	-0.9
10	1.568	11.6%	97	-1.2

No plate load test is conducted on the embankment as the arrangement is not suitable for surface at greater distance from the reaction frame. Therefore, subgrade soil is immediately compacted on the embankment. The subgrade is compacted in 5 lifts with each layer taken to loose thickness of 150-180 mm, and compacted till minimum density ($\geq$97% of laboratory maximum dry density value of 1.834 g/cm^3) is achieved within the specified water content (2% $\leq$ w $\leq$ 1%) (MoRTH 2013). The subgrade thickness is lifted with each layer added and compacted such as to meet a minimum total thickness of 500 mm, as mentioned by the IRC (IRC 2018b). **Table 5.2** shows the achieved densities of the 5 subgrade layers, and the relative compacted density to meet the prescribed minimum density, with water content falling within the desired range around the optimal amount of 8.8 %.

Table 5.2: In-situ density of compacted subgrade

Layer no. from top	In-situ ρ_d (g/cm^3)	*w* (%)	Relative density (%)	Difference of *w* from OMC (%)
1	1.779	7.07	97	-1.73
2	1.787	6.94	97	-1.86
3	1.794	7.27	98	-1.53
4	1.796	7.03	98	-1.77
5	1.788	7.44	97	-1.36

Two layers of base material are filled into the test pit to a loose thickness of about 250 mm. Within recommended lift ranging 75-250 mm, the layers are compacted to a total depth of 338 mm. The base thickness is taken higher than the recommended thickness of 250 mm for ICBP construction, but will cover the absence of the sub-base. The first reason sub-base is not provided because the purpose of the sub-base is primarily a drainage layer, however, the experiment is conducted in-house with no water seepage condition. Secondly, provision of sub-base layer will require to lay the subgrade at the lower depth, which will hinder plate load testing at limiting depth. The wet mix macadam material is compacted to meet the minimum density of 98% of the maximum dry density (maximum ρ_d = 2.217 g/cm^3) and water content tolerance of ± 2 % of OMC (IRC 2015; MoRTH 2013). The achieved densities and their respective water content are given in **Table 5.3**. The water content during compaction is maintained within the tolerance of 5.46 %.

Table 5.3: In-situ density of base

Layer no. from top	In-situ ρ_d (g/cm^3)	w (%)	Relative density (%)	Difference of w from OMC (%)
1	2.202	4.00	99.3	-1.46
2	2.182	3.90	98.4	-1.56

The minimum size of geocell openings can reduced till the size of the largest aggregate size (Kabiri Kouchaksaraei and Bagherzadeh Khalkhali 2020), however, small opening gives little space for easy filling and compaction of infill material. In the present study, the minimum size of the geocell for the bedding layer is limited to attaining density with the adopted construction. It is observed in **Table 5.4**, at same compaction effort given to the section with geocells of openings 150 mm × 150 mm, the ease of densification reduces with inclusion of smaller geocells. As density of bedding sand for confined and unconfined condition is targeted to be constant, attaining the level of density for bedding layer with smaller geocell openings without damaging the blocks is impossible.

Table 5.4: In-situ density for bedding layers

Bedding Layer	Average relative ρ_d (%)	Standard deviation (%)	Coefficient of variation (%)
Unconfined bedding layer	86.958	6.85	7.88
Confined with geocells 350 mm × 350 mm	83.040	5.77	6.95
Confined with geocells 250 mm × 250 mm	77.998	7.14	9.16
Confined with geocells 150 mm × 150 mm	64.359	8.08	12.56

Five test spots for each bedding layer are randomly selected for determination of density. The average relative density, density difference and variation for each set of bedding layer are listed in **Table 5.4**. At almost equal compaction levels, the relative dry densities of the bedding layers are in the range of 87-65%. For simulation, the relative density for all bedding layers is taken as an average of 78.089 % with a coefficient of variation of 12.63 % and a standard deviation of 9.86 %.

The uniformity of compaction over the surface is anticipated through the uniformity of joints. Consequently, following completion of compaction and preceding sand-filling into joints, the joint widths are measured using a Vernier Caliper. The averaged measurement of joints along each surface of the ICBP sections are presented in **Table 5.5**. For simulation purposes, a single joint width is selected, representing the average joint width across all bedding layers, amounting to 3.03 mm (rounded to 3.0 mm). The width deviation is recorded at 0.216 mm, with a coefficient of variation of 7.14%.

Table 5.5: Measured joint widths

ICBP with Bedding Layer	Average joint width (mm)	Standard deviation (mm)	Coefficient of variation (%)
Unconfined bedding layer	3.26	0.58	17.76
Confined with geocells 350 mm × 350 mm	3.09	0.59	18.99
Confined with geocells 250 mm × 250 mm	3.03	0.59	19.52
Confined with geocells 150 mm × 150 mm	2.74	0.46	16.84

5.2.2 Experimental structural analysis

Loads are gradually applied by positioning the loading plate on the surface and on the middle of the test pit. Dial gauges record vertical displacement across the width of the test pit. To capture deformation and plotting surface profiles, deflection profiles are collected at the center of the plate and at 300 mm, 600 mm, 900 mm, and 1200 mm on both sides of the plate. For foundation and base-foundation, **Figure 5.1** and **Figure 5.2** respectively show the averaged displacement recorded.

A total load of 30 kN is gradually applied onto the loading plate that is placed on the foundation surface, and dial gauge readings documenting for every 2.5 kN interval is recorded. In **Figure 5.1**, the surface profiles of foundation are presented as scaled displacement (δ_y) relative to the plate radius (a). Likewise, on the base, loads are gradually applied until reaching the maximum total of 27.28 kN. Dial gauge readings are recorded at every one-tenth increment of the total load. **Figure 5.2** shows the surface profile of the base, illustrating the progression of surface deformation at every load interval.

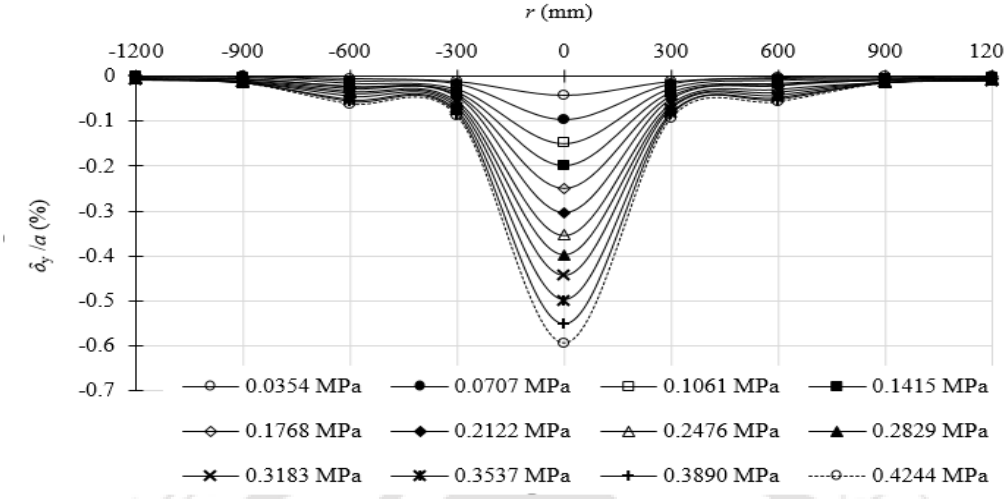

Figure 5.1: Surface profile of foundation at gradually increasing applied load

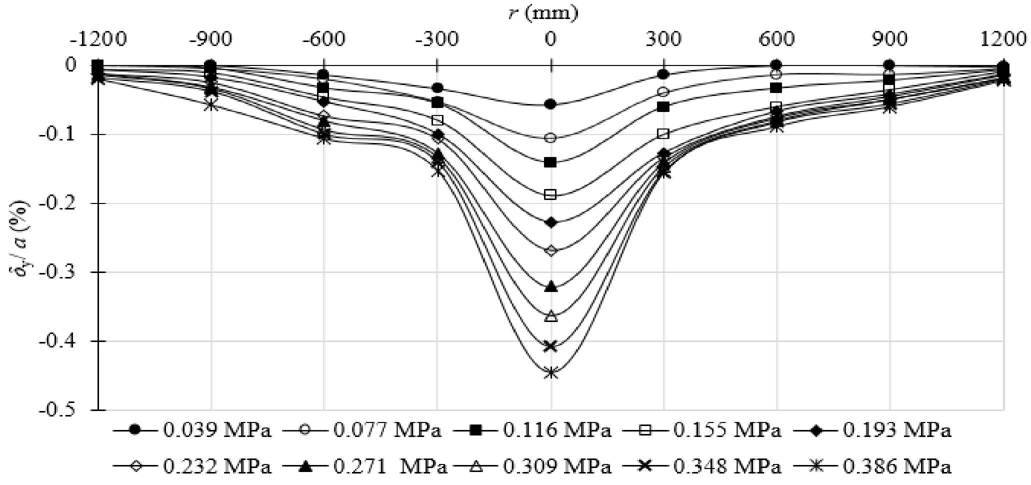

Figure 5.2: Surface profile of base at gradually increasing applied load

The applied loads on the base and subgrade are estimated using IITPAVE software, simulating the vertical stress levels under a 40 kN load on the pavement surface. However, the plate load test on the subgrade exceeds its requirement, as it only needs a maximum of 10 kN. Meanwhile, on the ICBP pavement layers, a load equivalent to half the standard axle load on dual wheels (40 kN) is gradually applied to a loading plate until reaching the predetermined peak load. The foundation and base have uniform granular layers, resulting in consistent reactions under the loading plate. Displacement values on both sides of the plate are averaged. Conversely, the ICBP surface experiences surface deformation due to block rotations, with each block moving relative to others under the imposed load. The responses of the pavement sections during plate load tests are illustrated in **Figure 5.3** to **Figure 5.7**.

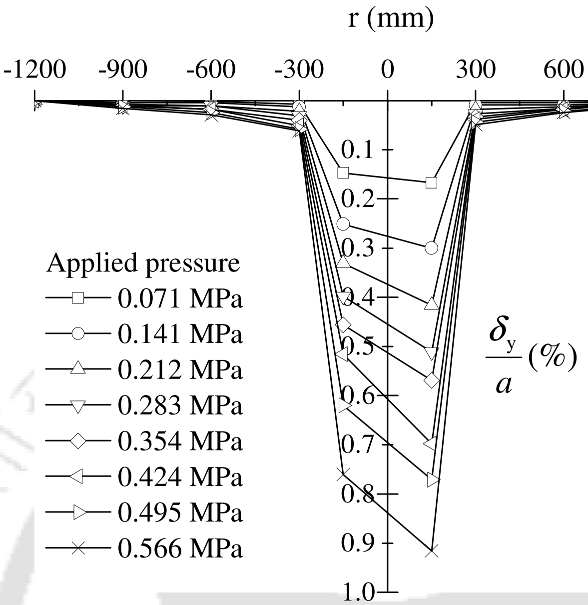

Figure 5.3: Surface Profile of ICBP with unconfined bedding layer

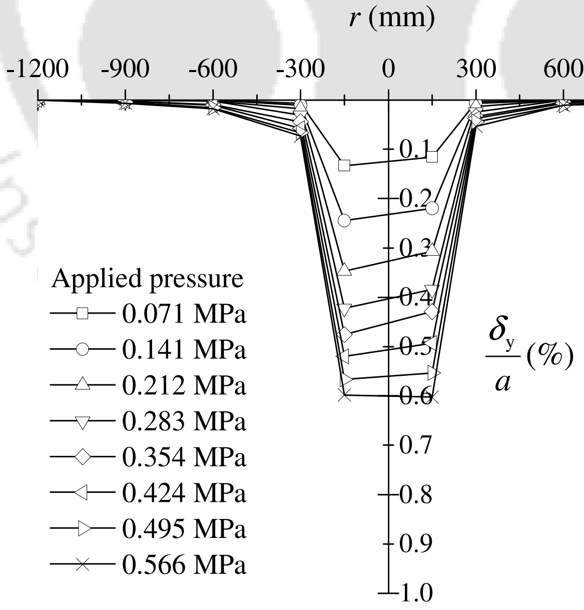

Figure 5.4: Surface Profile of ICBP with geocell (opening size 350 mm × 350 mm)

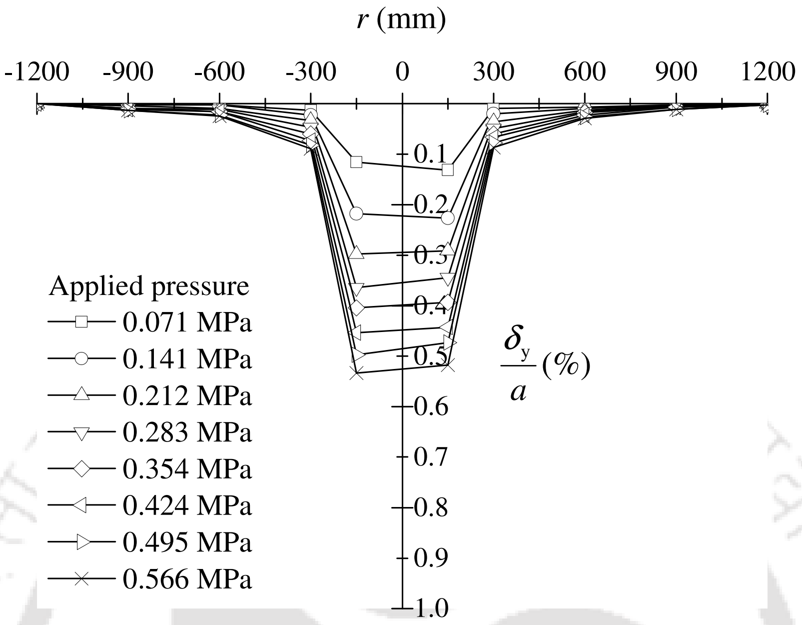

Figure 5.5: Surface Profile of ICBP with geocell (opening size 250 mm × 250 mm)

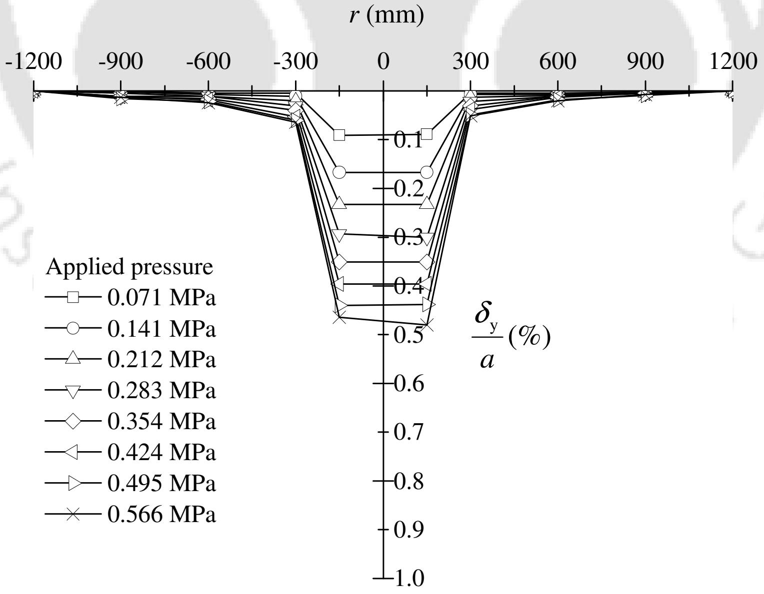

Figure 5.6: Surface Profile of ICBP with geocell (opening size 150 mm × 150 mm)

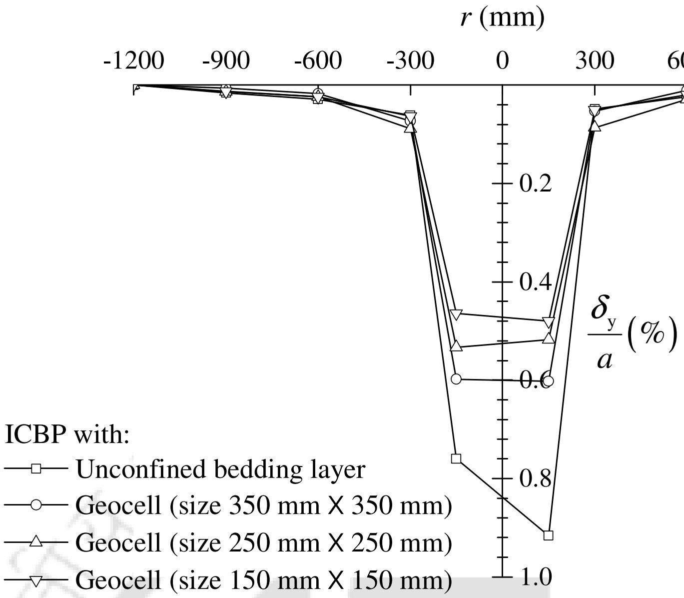

Figure 5.7: Surface profiles of ICBP sections at peak load

The presence of geocells within this bedding layer inhibits the early deformation of bedding layer and provision of geocells with smaller openings, strengthens the bedding layer to behave as a structural layer. The structural influence of confined bedding layer over the unconfined bedding layer is shown by shallower surface profiles as seen in **Figure 5.7**.

In addition to the frictional resistance between sand and the walls of the geocell, along with the passive resistance from neighbouring cells, the confinement effect, slab action, and tensioned membrane effect quickly come into play when the walls are in close proximity. The overall effect of these factors can be experimentally quantify by the response in terms of the displacement at the loading area. For geocells openings 350 mm × 350 mm, 250 mm × 250 mm and 150 mm × 150 mm, the average reduction of displacement measured on the loading plate are 27.77 %, 36.62 % and 43.21 % respectively, with the minimum reduction of the differential displacement of about 21 %.

5.3 Simulation results

Simulated investigation of the foundation, two-layered system of base-foundation, and ICBP sections are discussed herein. The prime objective of employing FEM in this study is to ascertain the material properties of replicated pavement sections. With availability of existing pavement models, the FEM models are then validated for quality of replication. In ICBP sections, findings of the two types of FEM models, i.e., the ICBP sections with an actual surface layer and with the homogenised surface layer, are verified with experimental observations.

5.3.1 Foundation

The foundation comprises the subgrade and the underlying embankment, consisting of two types of materials. The process of simulating the foundation entails determining the foundation layer condition incorporating behavior of subgrade-embankment as a composite layer. Within the scope of software analysis, the foundation material property is estimated by implementing FEM, and the results are validated through comparison with established foundation models.

5.3.1.1 Iteration of foundation structural property

Assuming the embankment and subgrade as elastic under present conditions of stress, the material properties of the embankment and subgrade determined is the equivalent elastic modulus ($E_{foundation}$). Since plate load test is not conducted on embankment, the foundation's elastic modulus is determined as an effective mechanical property of the two-layered foundation and an elastic modulus of an equivalent material that is compacted in to two layers. The two layers are simulated as two types of foundations: (i) Foundation-1 where $E_{foundation}$ is determined for a material that is uniform throughout, and (ii) Foundation-2 where $E_{foundation}$ is determined for the equivalent material when it is compacted into two layers, with thicknesses of actual subgrade and embankment. To simulate the experimental observations, iterated $E_{foundation}$ of the two foundation assumptions are given in **Figure 5.8**.

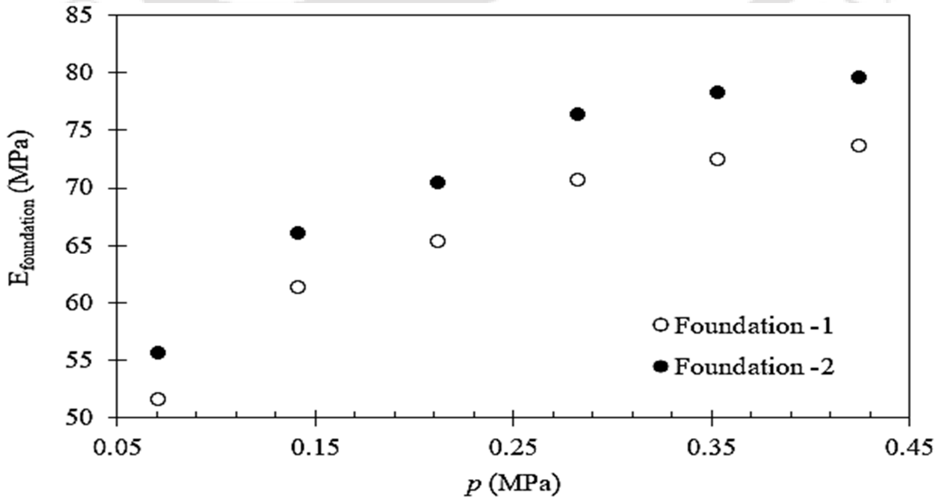

Figure 5.8: Iterated $E_{foundation}$ for assumed foundation conditions

The responses measured as vertical stress (σ_z) along the depth and vertical displacement (δ_y) of the surface corresponding to Foundation-1 and Foundation-2 are respectively illustrated in **Figure 5.9** and **Figure 5.10**. Even though Foundation-2 is stiffer, however as illustrated, the responses of both foundation types streams along similar curves.

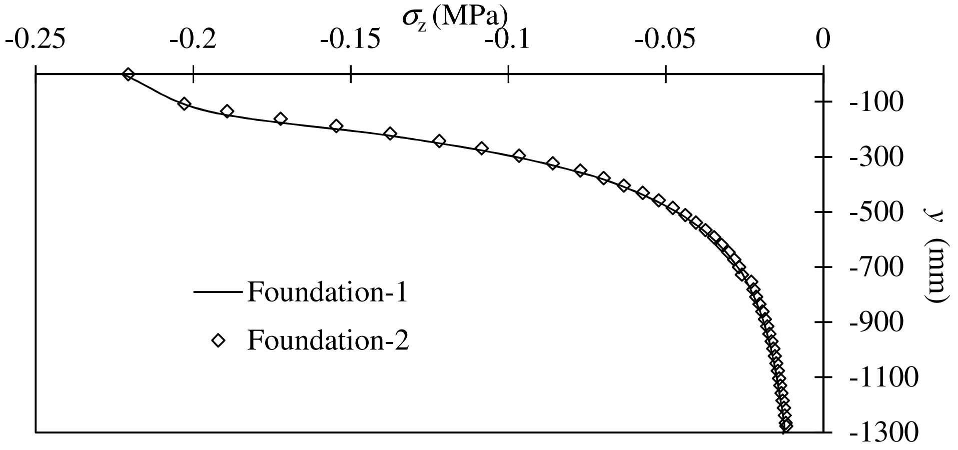

Figure 5.9: Vertical stress measured along the depth

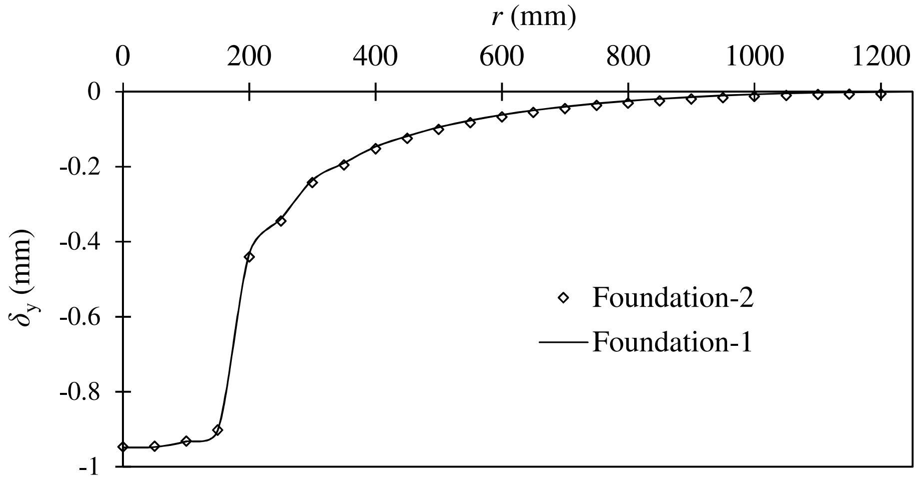

Figure 5.10: Surface profiles of the two assumed foundations

Considering IRC specification for subgrade whose material is different to embankment, design of flexible pavement is based on the combination of subgrade and embankment and their effective/ equivalent modulus (IRC 2018b). Therefore, for the present study, the elastic modulus of foundation is the effective/ equivalent foundation modulus.

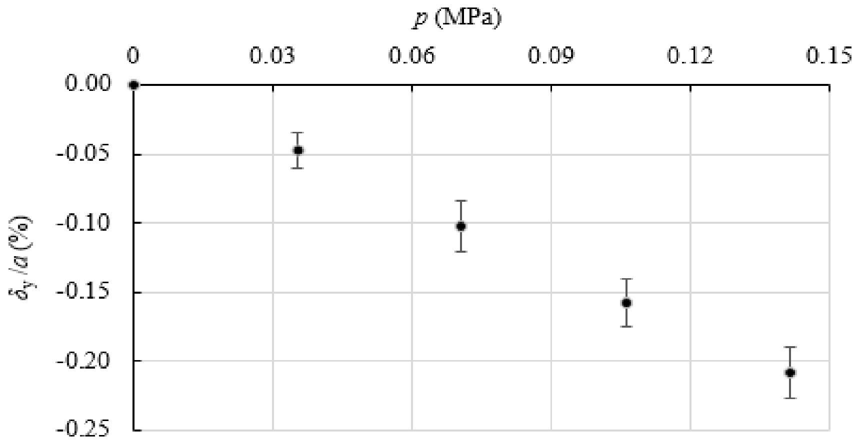

Figure 5.11: Cumulative displacement on a loaded foundation

The peak loads for plate load test on base and foundation surfaces are estimated from vertical stress reaching their surfaces respectively when a 40 kN load is applied to the pavement surface. The stresses reaching the surfaces of underlying layers are calculated using the MEPDG tool, IITPAVE, specifically developed for flexible pavement design. Therefore, to evaluate how the layer responds to this stress magnitude, a load is directly applied onto a circular, rigid plate of 300 mm diameter that is placed on the layer. Also, it is projected that no load exceeding 10 kN will cause the expected stress. **Figure 5.11** shows the cumulative displacement of loading plate as load is gradually increased till it reaches peak load. Consequently, using FEA on the test pit model of foundation, the effective elastic modulus of the foundation is iterated to assess the responses shown in **Figure 5.11**.

The equivalent elastic modulus of the foundation ($E_{foundation}$) is estimated to be 57.10 MPa. To validate the FEM model against existing foundation models, the test pit foundation size may be too small to assume it as a semi-infinite layer. Therefore, the foundation size is increased to a 12.0 m cube while maintaining the same boundary conditions. By subjecting the test pit model to a point load of 10 kN, the corresponding response is illustrated in **Figure 5.12**, and a comparison of the two foundation models reveals that the deformation in the enlarged foundation is more pronounced, attributed to the increased distance between wall restraints. To show the difference, RMSE, MAE and ME between the two surface profiles are calculated are of values 0.15 %, 0.091 %, and 0.078 %, respectively.

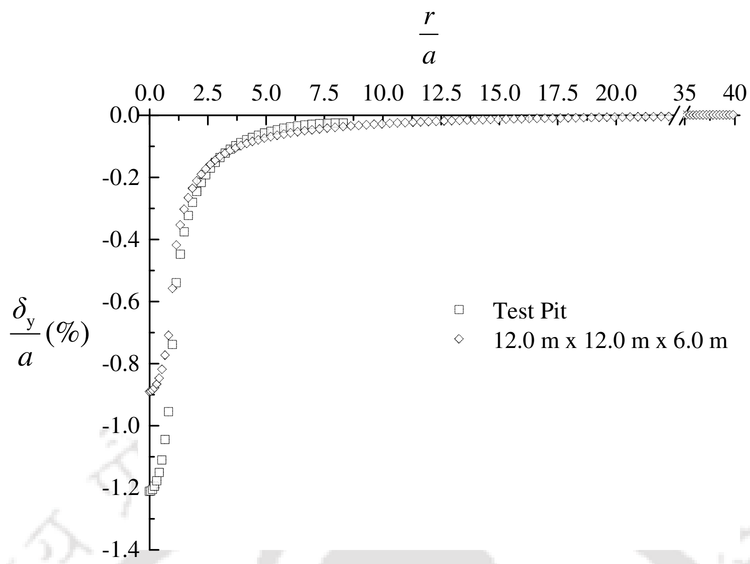

Figure 5.12: Surface profile of simulated foundation

5.3.1.2 Validation

The validity of the simulated foundation values is established according to the Boussinesq's theory, which is based on a concentrated load that is applied on the elastic and homogeneous half-space (Huang 2009). However, the stresses, strains and displacement resulting from the concentrated load are integrated to determine those arising from a circular loaded area. When load is applied over a circular loading area, critical stress, strain, and deflection is calculated under the circular area and along the axis of symmetry. Therefore, responses at any depth (*y*) measured along the axis of symmetry of the FEM foundation models; test pit size, and 12.0 m × 12.0 m × 6.0 m enlarged size are validated with Boussinesq's equations given in Equation (**5.1**) to Equation (**5.5**).

$$\text{Vertical Stress (MPa)}, \ \sigma_y = p\left[1-\frac{y^3}{\left(a^2+y^2\right)^{1.5}}\right] \qquad \textbf{(5.1)}$$

$$\text{Radial Stress (MPa)}, \ \sigma_r = \frac{p}{2}\left[1+2\nu-\frac{2(1+\nu)y}{\left(a^2+y^2\right)^{0.5}}+\frac{y^3}{\left(a^2+y^2\right)^{1.5}}\right] \qquad \textbf{(5.2)}$$

$$\text{Vertical Strain, } \epsilon_{\text{y}} = \frac{(1+v)p}{\text{E}_{\text{foundation}}}\left[1-2v+\frac{2vy}{\left(a^2+y^2\right)^{0.5}}-\frac{y^3}{\left(a^2+y^2\right)^{1.5}}\right] \qquad \textbf{(5.3)}$$

$$\text{Radial Strain, } \epsilon_{\text{r}} = \frac{(1+v)p}{2\text{E}_{\text{foundation}}}\left[1-2v-\frac{2(1-v)y}{\left(a^2+y^2\right)^{0.5}}+\frac{y^3}{\left(a^2+y^2\right)^{1.5}}\right] \qquad \textbf{(5.4)}$$

$$\text{Vertical displacement (mm), } \delta_{\text{y}} = \frac{(1+v)pa}{\text{E}_{\text{foundation}}}\left\{\frac{a}{\left(a^2+y^2\right)^{0.5}}+\frac{1-2v}{a}\left[\left(a^2+y^2\right)^{0.5}-y\right]\right\} \qquad \textbf{(5.5)}$$

Calculated responses and simulated responses are calculated when the foundation is subjected to a concentrated load 10 kN acting at the centre of the surface area. The calculated responses, i.e., vertical stress, radial stress, vertical strains, radial strains and vertical displacement along the centreline of loading are recorded. The responses of the three models, i.e., test-pit sized FEM model, enlarged FEM model and half space foundation model are then plotted and compared in **Figure 5.13** to **Figure 5.17**.

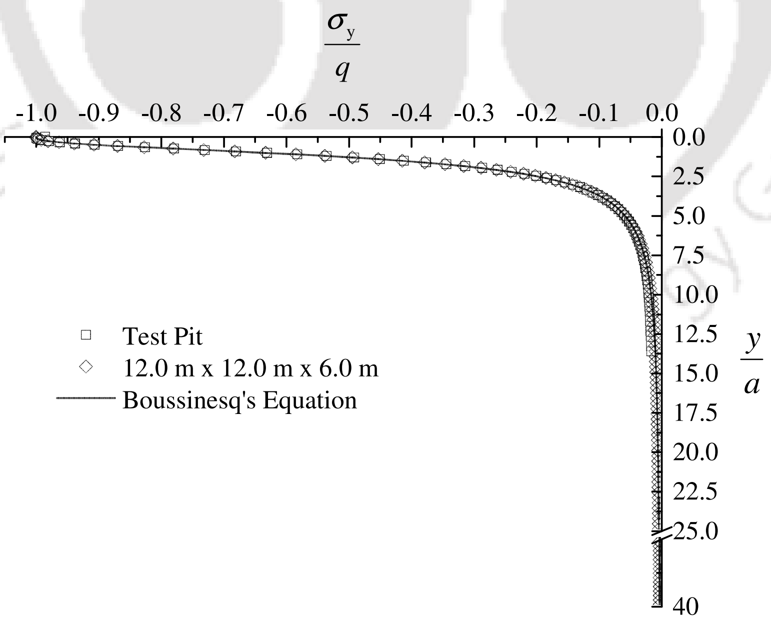

Figure 5.13: Vertical stress calculated for through the foundation depth

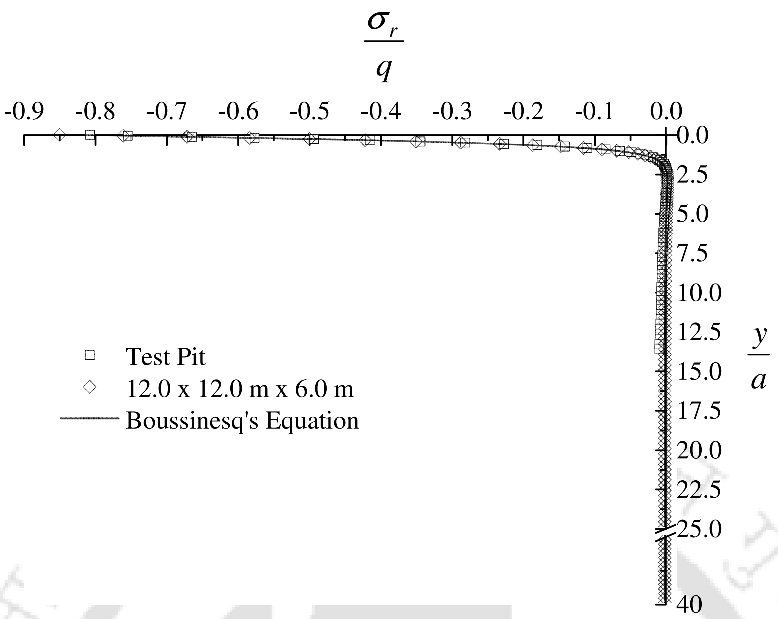

Figure 5.14: Radial stress calculated for through the foundation depth

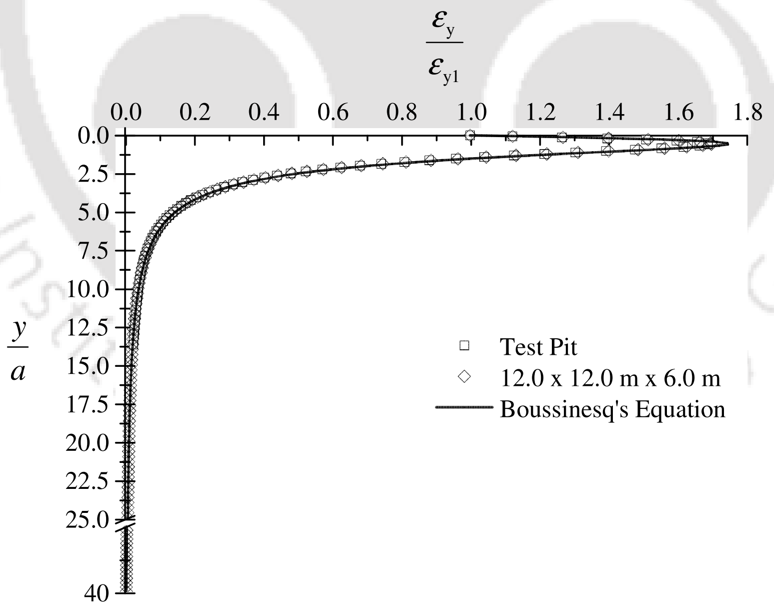

Figure 5.15: Vertical strain calculated for through the foundation depth

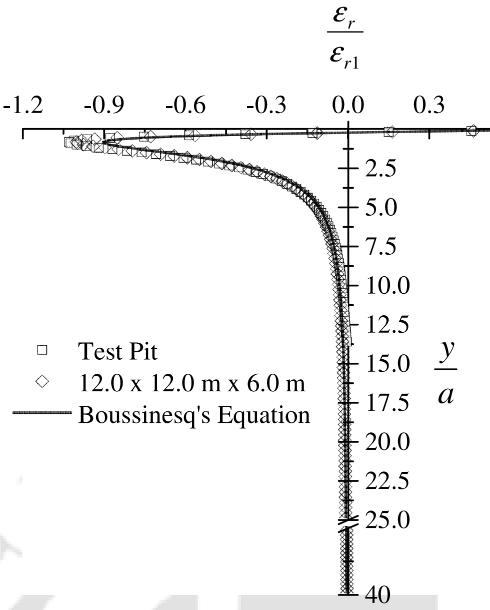

Figure 5.16: Radial strain calculated for through the foundation depth

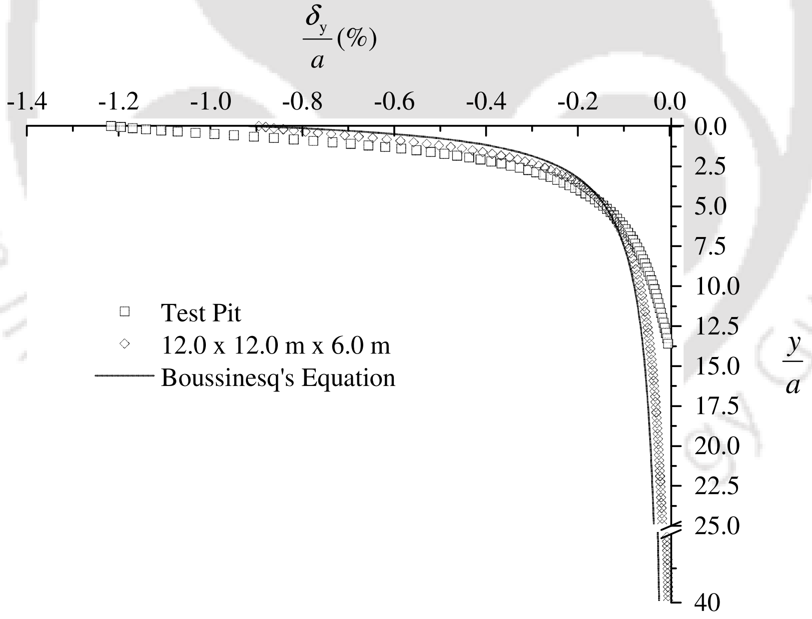

Figure 5.17: Vertical displacement calculated for through the foundation depth

For all stress and strain values, the response curves follow similar paths while the displacement values of test pit diverge to zero near test pit bottom. **Table 5.6** provides a comparison of the greater differences among the responses of the three models, in which errors are calculated for $\frac{\delta_y}{a}$ values.

Table 5.6: Comparison of FE analysed displacements with Boussinesq's equation

	Along the depth		
Foundation model	MAE (%)	RMSE (%)	ME (%)
2.5 m × 2.5 m × 2.048 m	0.125	0.181	0.096
12.0 m × 12.0 m × 6.0 m	0.029	0.044	0.006

5.3.2 Two-layered system

The material property of the base is also iterated using FEM. Iteration is performed on the plate load test response of the two–layered section consisting of the base and foundation. Within the scope of software analysis, the material property is predicted, and results are validated with established multi-layered pavement design tools.

5.3.2.1 Iteration of base structural property

Estimated peak loads for plate load test on base is derived from the vertical stress reaching the base upon the action of a 40 kN load on the pavement surface. The approximated pressure on the circular area of 300 mm corresponds to a load approximately 30 kN is subsequently applied to the base. Experimental observation depicted in **Figure 5.18**, involves the cumulative displacement of the plate recorded at regular load intervals until it reaches 27.28 kN.

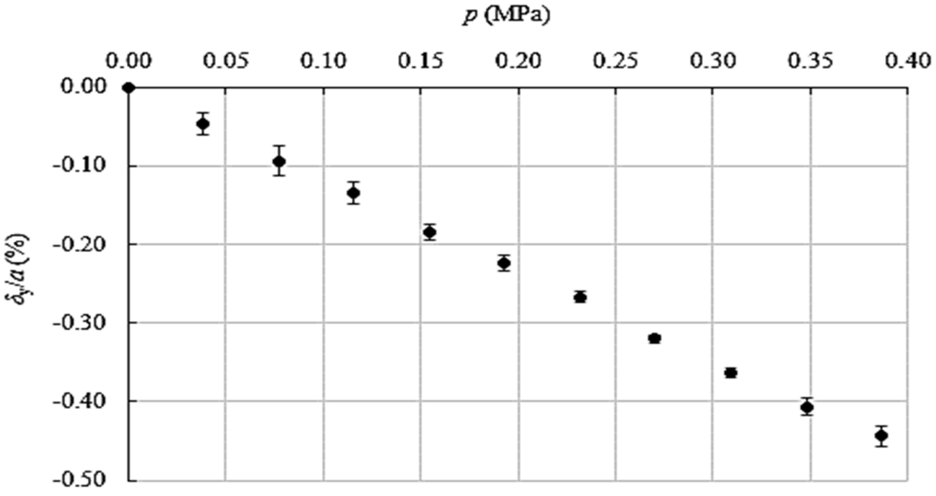

Figure 5.18: Cumulative displacement on a loaded base-subgrade

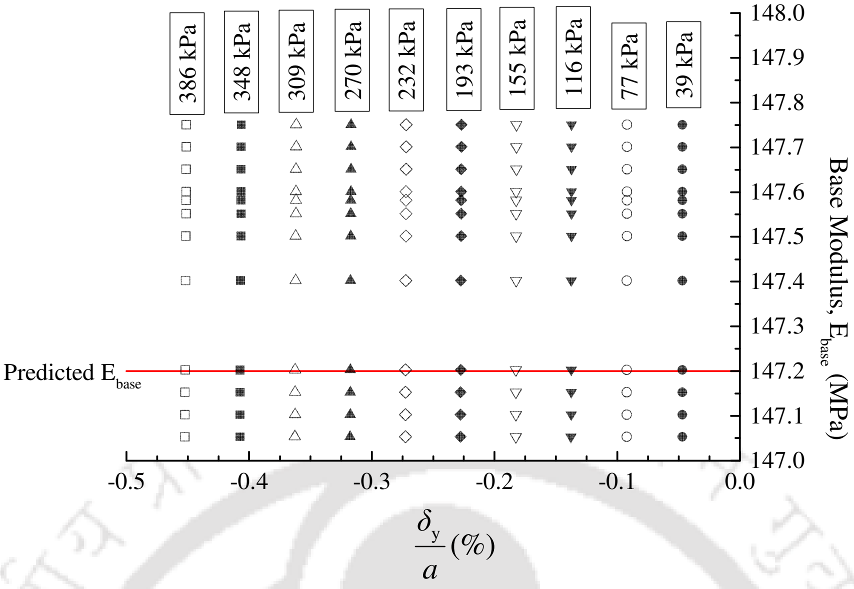

Figure 5.19: Predicting E_{base}

The precise geometry of the two layered system, i.e., base and foundation are utilised to iterate the elastic modulus of the base (E_{base}). As depicted in **Figure 5.19**, the iterated modulus shows a linear response the system showed towards applied load. It also shows sensitivity of the system response is minimal over the wide range of moduli considered. Therefore, a specific E_{base} is selected over the modulus range by implementing the Bland-Altman plot (Altman and Bland 1983). The Bland-Altman plot, also known as the difference plot, will graphically compare the agreement between the observed experimental response with simulated response.

The response here is the scaled plate displacement, i.e., $\frac{\delta_y}{a}$, and the difference between the two models' responses are plotted against their mean values. Simulated measurements are quantified whether they are acceptable if their differences fall between the limits of agreement. The two limits of agreement are the lower limit of agreement (LOA) and upper limit of agreement (UOA) which are defined by a 95 % prediction interval of the value of the difference, and they are computed by the Equation (**5.6**).

$$\text{Limit of agreement} = \text{Mean difference} \pm (1.96 \times \text{Standard Deviation of differences}) \qquad \textbf{(5.6)}$$

At E_{base}= 147.20 MPa, there is an agreement between the two measurements and as shown in **Figure 5.20**, the values are evenly scatter towards the mean of the differences, i.e., Bias.

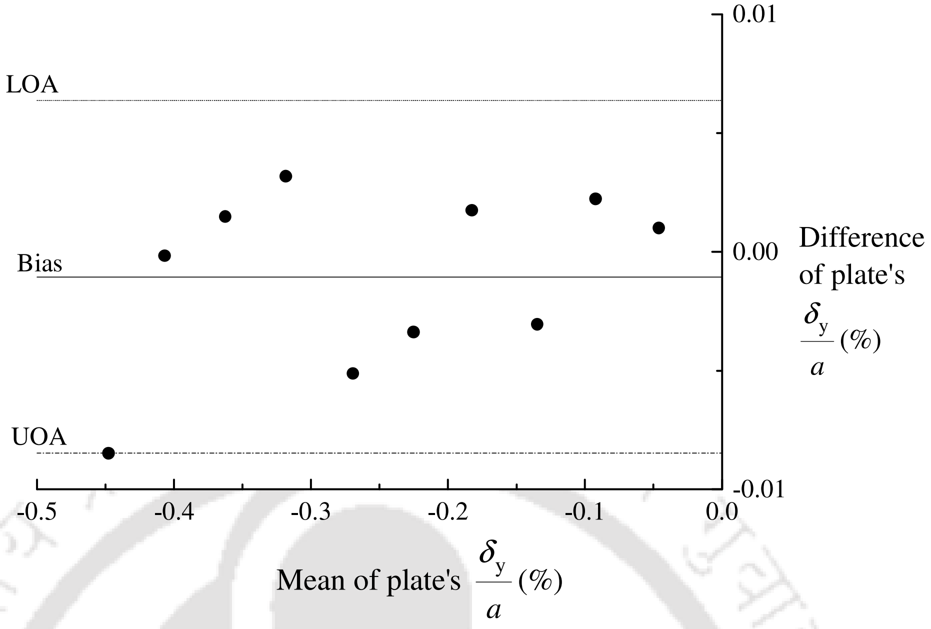

Figure 5.20: Bland Altman plot of predicted E_{base}

5.3.2.2 Validation

Validation of the simulated base-foundation is conducted by comparing its responses with generated stresses, strains, and displacements of IITPAVE software, a mechanistic-empirical model for flexible pavement design (IRC 2018b). IITPAVE is based on the design concept for a linear elastic foundation half-space, comprising semi-infinite linear elastic layers overlying the elastic half-space foundation, with complete bonding between the layers at the interfaces. An FEM model of the base-foundation which is considered for validation is an enlarged test-pit sized model of dimensions, 12.0 x 12.0 m x 6.338 m. The foundation size is the same taken for foundation validation. The boundary conditions of the validation model are the same as that of the test pit model, while loading condition is a concentrated load of 27.28 kN acting at a point at the centre of the surface area.

Responses of the two models, i.e., IITPAVE calculated model and FEA model (FEA Calculated) are recorded. **Figure 5.21** to **Figure 5.25** show the values of vertical stress, radial stress, vertical strains, radial strains and vertical displacement along the centreline of loading. Surface profiles of the two two-layered systems are presented in **Figure 5.26**. For all stress and strain values, the response curves show similarity, whereas there are notable differences in the displacement values and surface profile.

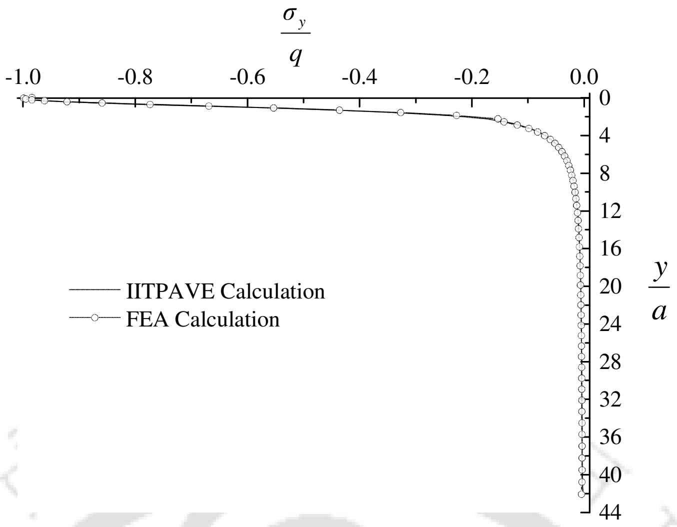

Figure 5.21: Vertical stress calculated through the two-layered depth

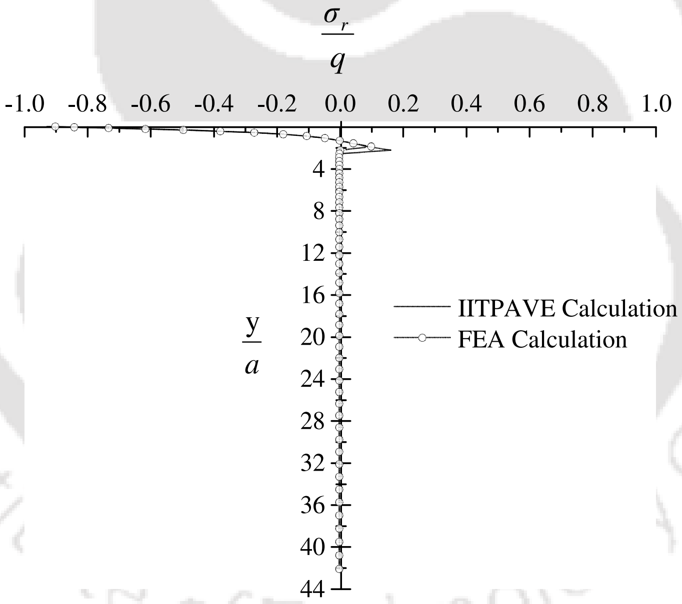

Figure 5.22: Radial stress calculated through the two-layered depth

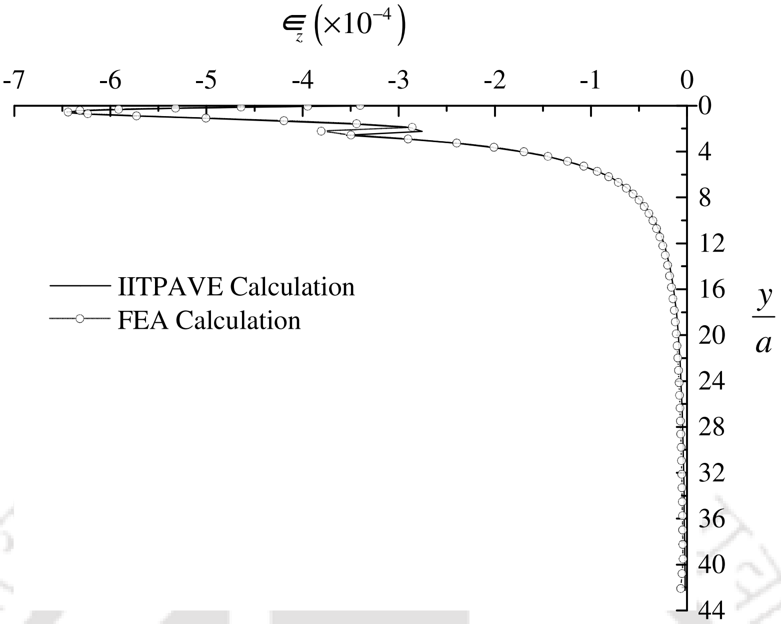

Figure 5.23: Vertical strain calculated through the two-layered depth

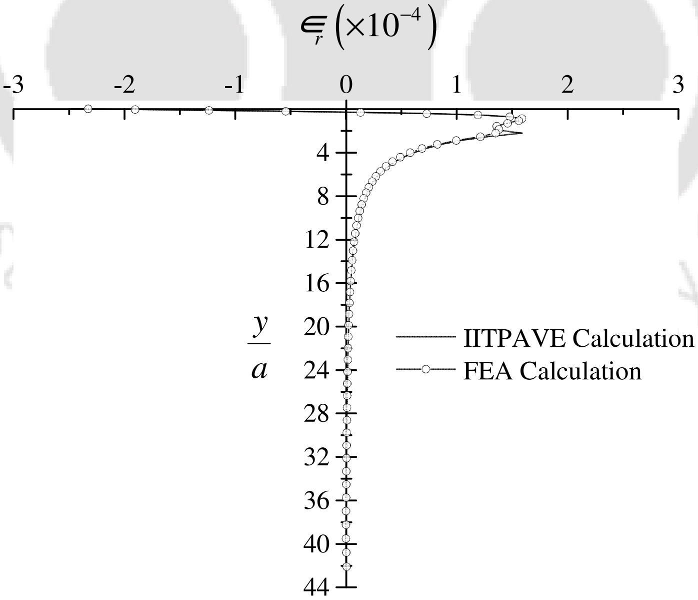

Figure 5.24: Radial strain calculated through the two-layered depth

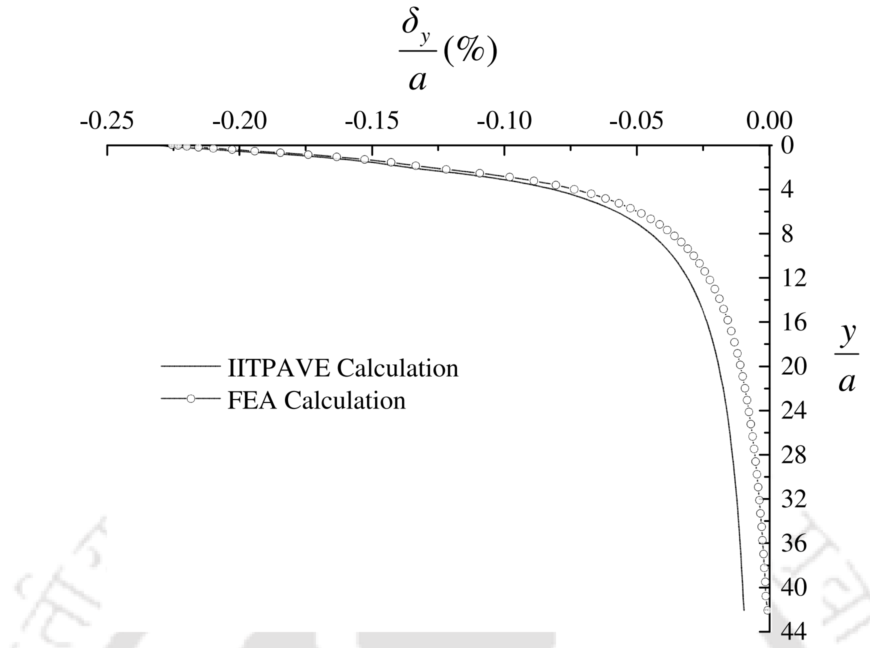

Figure 5.25: Vertical displacement calculated through the two-layered depth

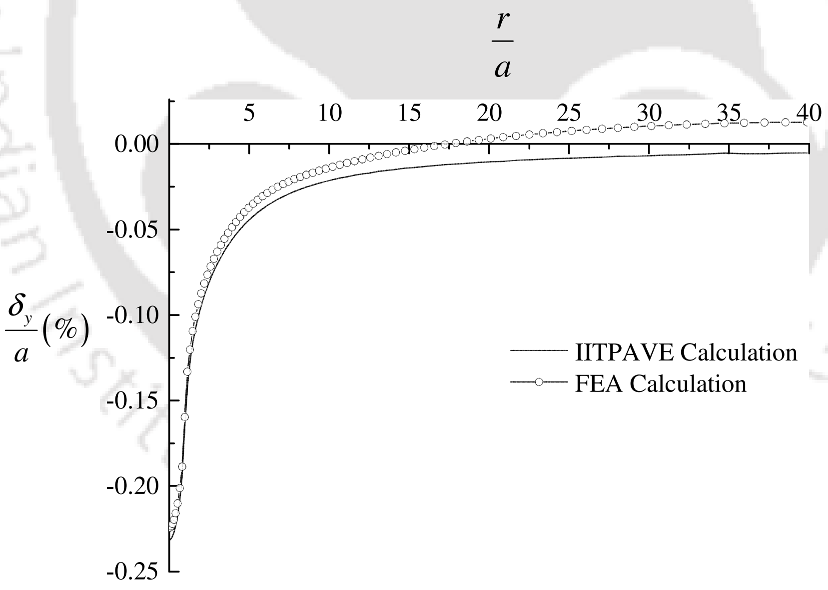

Figure 5.26: Surface profiles of the two-layered models.

Table 5.7 shows comparison of the greater differences among the responses of the two models, in which errors are calculated for vertical displacement values.

Table 5.7: Comparison between FEM model and IITPAVE results

	Along the depth			Radially from loading centre		
Layer	MAE (%)	RMSE (%)	ME (%)	MAE (%)	RMSE (%)	ME (%)
Base-foundation	0.008	0.008	-0.008	0.010	0.011	-0.010

5.3.3 ICBP sections

As seen in **Figure 5.7**, the inclusion of geocells within the bedding layer fortifies the layer, causing a delay in surface deformation. The improved stiffness of confined bedding layer is experimentally shown as reduced vertical displacement. Subsequently, the bedding layers' properties will be estimated with FEM. Three approaches that motivate establishment of the equivalent property of the confined bedding layers are employed and they are:

a. Surface layer and bedding layer constitutes a single uniform and homogeneous layer.
b. Material property of bedding layer is estimated as an increased shear strength due to the "apparent cohesive strength" imposed by geocells inclusion.
c. The surface layer is taken to its actual part geometries while bedding layer, with or without geocells is a uniform and homogeneous layer. Later, the surface layer is homogenised using micromechanics, and attempted to replace.

5.3.3.1 Iteration of bedding layer composite property

The stiffness values of the bedding layers can be assumed three ways. The first approach considers the surface layer and bedding layer as one uniform and homogeneous layer. The approach that assumes the whole part as one uniform layer with a single sets of material properties is macroscopically assuming the whole part as continuous, neglecting the slab action of the surface layer. The slab behaviour of the ICBP surface layer is caused by the blocks rotations, which undergo knocking, wedging and supporting against each other for load transfer and stress dispersion across and into the pavement depth. However, for all ranges of Poisson's ratios and moduli, considering the surface and bedding layer as one uniform layer is not sufficient to predict the actual ICBP behaviour in which required $\frac{\delta_y}{a}(\%)$ is 0.827 %. **Table 5.8** shows the $\frac{\delta_y}{a}(\%)$ of simulated ICBP with unconfined bedding layer, considering different boundary conditions and material properties.

Table 5.8: Replication of ICBP behaviour with a uniform surface layer

Boundary condition of lateral walls of surface layer and bedding layer	v	Equivalent elastic modulus (MPa)	$\frac{\delta_y}{a}(\%)$
Restrained against bulging	0.32	177	0.564
		160	0.585
Restrained against all movement	0.32	3540	0.255
		1770	0.308
		885	0.365
		177	0.564
		160	0.585
	0.33	177	0.561
	0.40	177	0.540

In second approach, the bedding layer is assumed to be an elastic-plastic material following Mohr-Coulomb failure criterion, but strength improvement is estimated as an apparent cohesive strength (c') (Rajagopal et al. 1999). Secondly, the bedding layer is considered as a homogeneous layer with an increased stiffness, and material property to be iterated is the layer elastic modulus.

Improvement in shear strength (s) by introducing apparent cohesive strength (c') (Rajagopal et al, 1999) is given in following Equation (**5.7**).

$$s = c' + \sigma \tan \phi \qquad \textbf{(5.7)}$$

Here, σ is the normal stress to the failure plane and ϕ is angle of internal friction. When simulating the confined bedding layer, the inclusion of a stiffer material to represent an apparent cohesive strength (c') becomes insignificant when c' exceeds 0.7 MPa, as the plate displacement remains constant.

Thirdly, discrete modelling is considered in which the ICBP is incorporated to its actual constituent geometry, however, the confined bedding layer is assumed uniform and homogeneous throughout. When the bedding sand is not confined within geocells, it exhibits elasto-plastic characteristics. The elasto-plastic behaviour of the bedding sand is simulated considering the Mohr-Coulomb failure criterion. However, the presence of geocells within this bedding layer inhibits the early deformation of bedding layer. Provision of geocells renders the implementation of elasto-plastic behaviour insufficient, the behaviour of the geocell-reinforced layer is then iteratively determined based on its elastic modulus.

The trial elastic moduli of the confined bedding layers vary from 60 to 900 MPa. As shown in **Figure 5.27** to **Figure 5.29**, the equivalent elastic modulus of each confined bedding layer (E_{ebl}) is estimated and plotted against the mean square error between experimental and simulated surface profiles. The fluctuating E_{ebl} indicates a variability of the simulation outcomes which may be due to the computational algorithms. However, the elastic modulus has to be selected as one of the trial values. Within the program aspects, the E_{ebl} are subjected to a perturbation check to verify the values are not erratic to slight changes. With perturbation check for the elastic modulus within the range considered, the complex physical system will be analysed for erratic responses to small changes of the material property of the bedding layer. The validity of the chosen modulus is confirmed by verifying pavement model responses for the selected elastic modulus and within a perturbation range of ± 0.3 MPa.

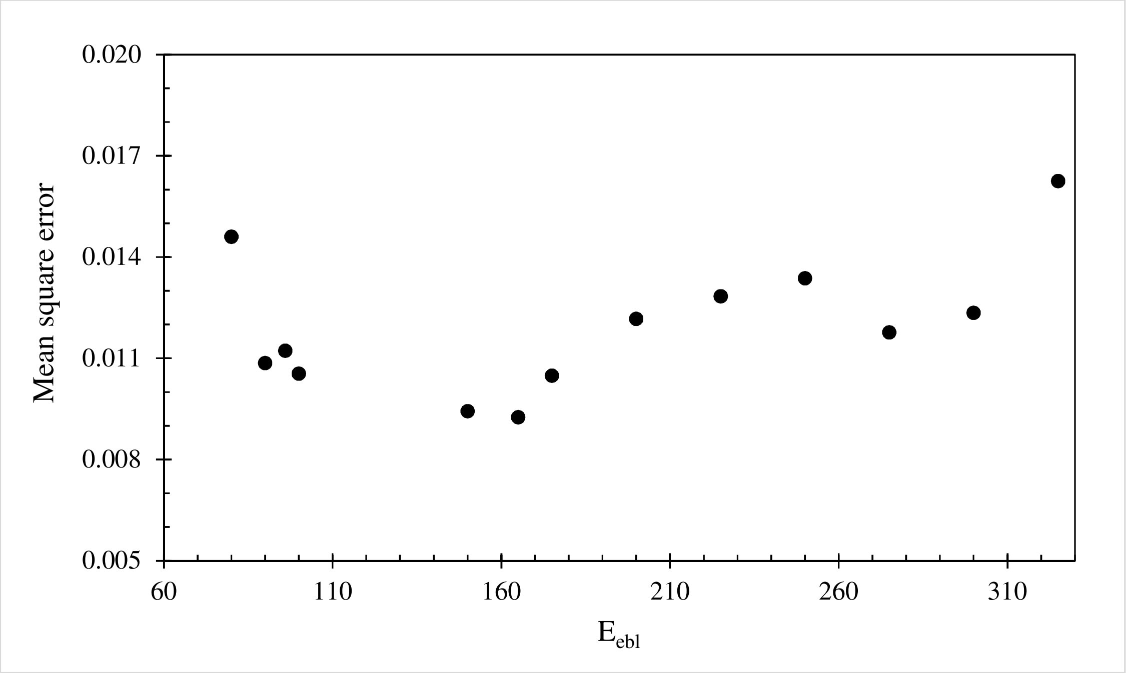

Figure 5.27: MSE for E_{ebl} of confined bedding layer (geocell size 350 mm × 350 mm)

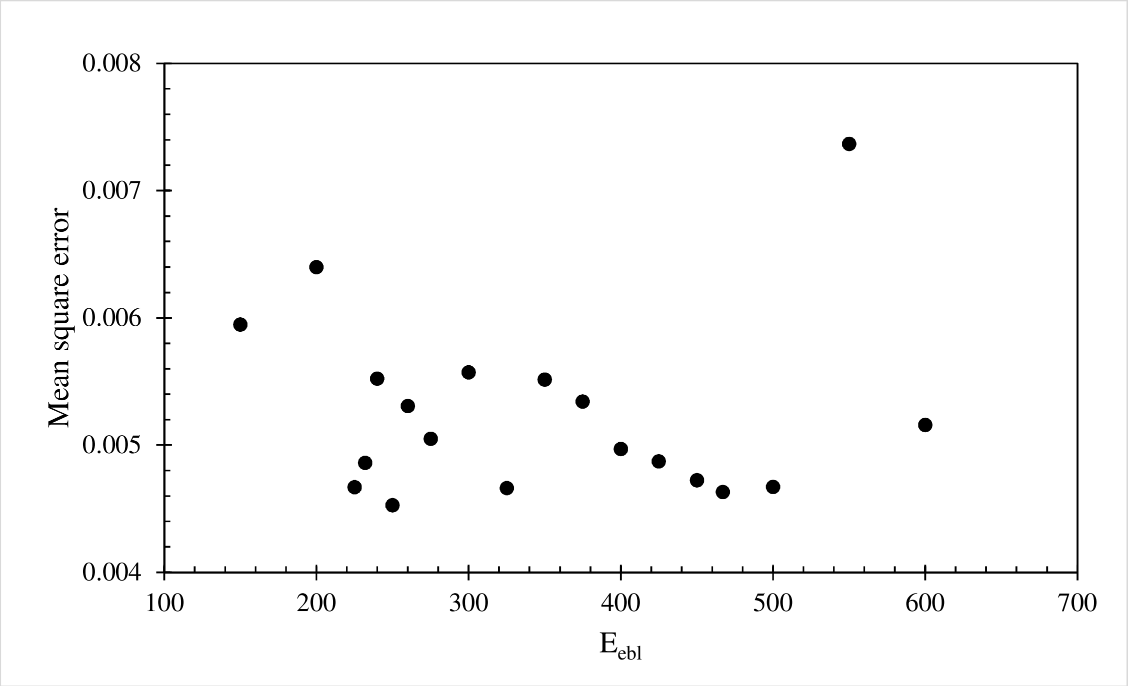

Figure 5.28: MSE for E_{ebl} of confined bedding layer (geocell size 250 mm × 250 mm)

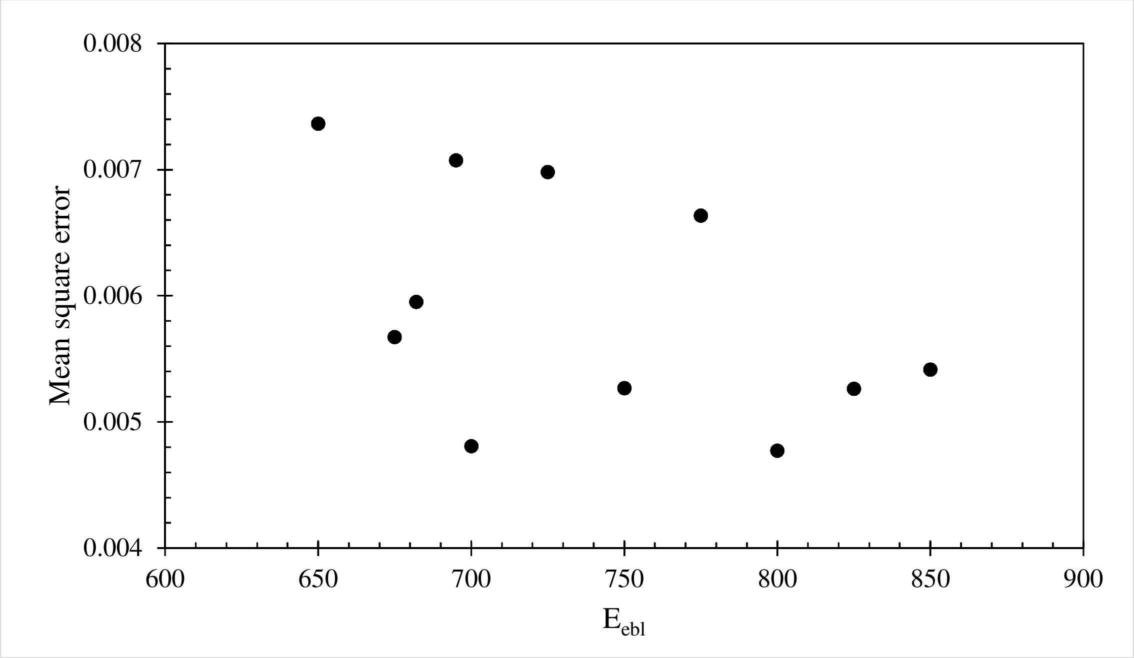

Figure 5.29: MSE for E_{ebl} of confined bedding layer (geocell size 150 mm × 150 mm)

After perturbation check of moduli in the range of 60 to 900 MPa, achieved E_{ebl} for geocells with opening sizes 350 mm × 350 mm, 250 mm × 250 mm and 150 mm × 150 mm are 96 MPa, 250 MPa and 700 MPa, respectively. The error and standard deviation of the plate $\frac{\delta_y}{a}$ values within the perturbation range are listed in **Table 5.9**.

Table 5.9: Achieved E_{ebl} of confined bedding layers

Geocell opening size	RMSE (%)	Standard Deviation (%)
350 mm × 350 mm	0.058	0.0007
250 mm × 250 mm	0.041	0.0001
150 mm × 150 mm	0.048	0.0006

The unconfined bedding layer encounters plastic deformation at the level of stress induced by the 40 kN static load. However, geocells incorporated within the bedding layer serve to delay the early plastic deformation, enhancing the ICBP stiffness and ability to withstand higher stress before succumbing to permanent deformation. The influence of geocell inclusion and dependence on geocell sizes is quantify by a modulus of improvement factor (MIF), which is a factor of the elastic modulus of geocell reinforced layer to that of an unconfined layer. MIFs of the four bedding layers are shown in **Figure 5.30**.

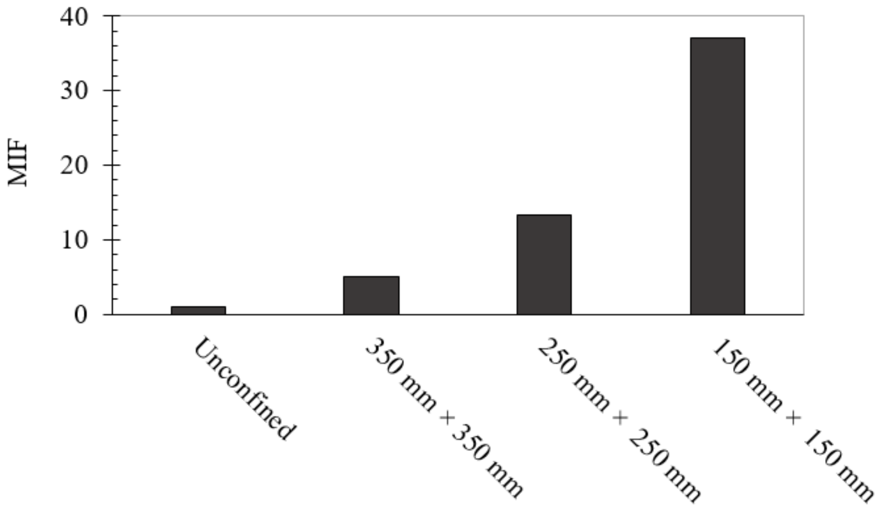

Figure 5.30: MIF of bedding layers

The improvement to stiffness of the bedding layer with inclusion of geocells is corroborated by MIF>1. The influence of the geocells considered in the present study, has shown there is an improvement to the layer stiffness in terms of the increased elastic modulus value and preventing premature permanent deformation of the bedding sand.

5.3.3.2 Homogenisation the ICBP surface layer

An approach has been considered that involves treating the bedding layer, blocks, and jointing sand as a single, uniform, and elastic layer. According to the responses given in **Table 5.8**, the simulated $\frac{\delta_y}{a}(\%)$ for the uniform surface layer do not meet the experimental acquired value of 0.827 %. This attempt to make the entire layer uniform has revealed that the resulting stiffness is too high to accurately predict experimental observations. Since homogenising the entire surface layer into a uniformly isotropic elastic behavior proves inadequate, determining the equivalent property of the composite requires implementing homogenisation at the constituent scale. The advantage of material property homogenisation at the constituent is the ability to execute the response of the system, by focusing the material behavior at the refined scale. Thereafter, the complex actual surface is replaced by the uniform, orthotropic elastic layer, and with the same underlying layers, simulation of the ICBP sections is conducted. The responses of the ICBP with the homogenised surface layer and ICBP that is discretely modelled to its actual geometries are presented in **Figure 5.31** to **Figure 5.38**. **Figure 5.31** to **Figure 5.34** illustrate the vertical displacement which is measured from bedding layer surface and along the centreline of loading.

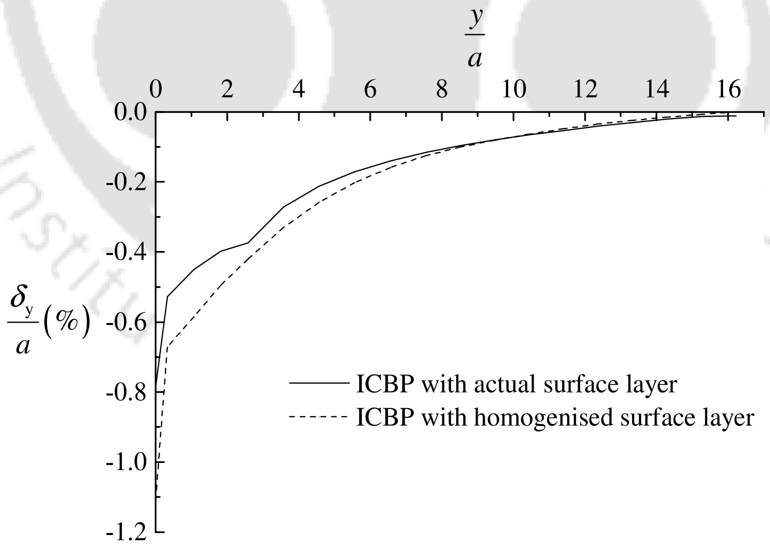

Figure 5.31: Displacement along the depth of simulated ICBP with unconfined bedding layer

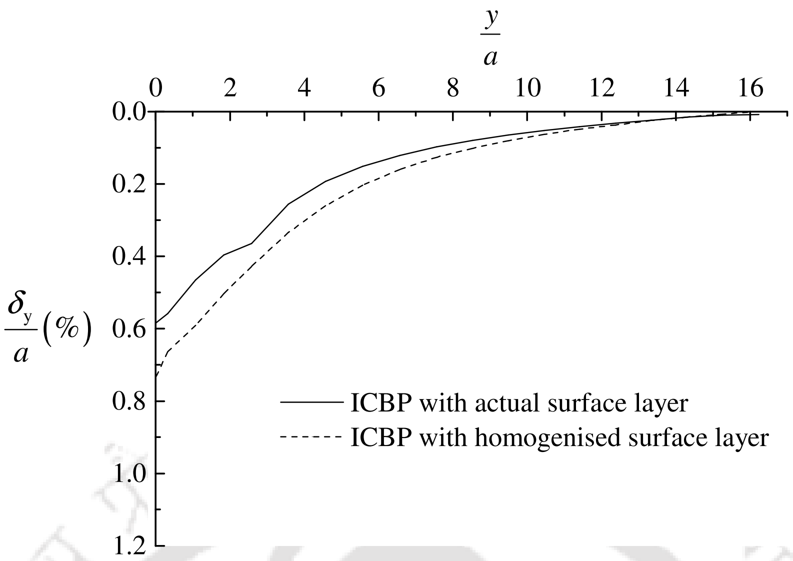

Figure 5.32: Displacement along the depth of simulated ICBP with confined bedding layer (geocell opening size of 350 mm × 350 mm)

The displacement values under homogenised surface are greater showing the ICBP actual surface layer is slightly stiffer than the homogenised counterpart. Under the same path, **Figure 5.35** to **Figure 5.38** entails the vertical stress.

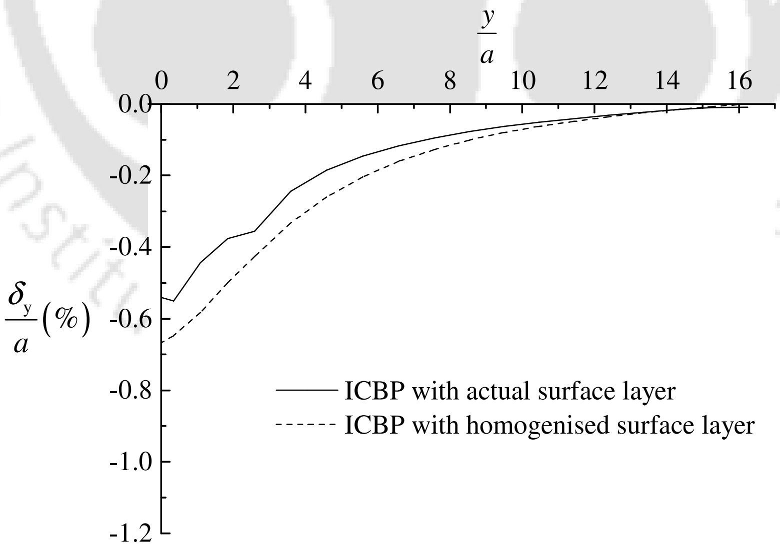

Figure 5.33: Displacement along the depth of simulated ICBP with confined bedding layer (geocell opening size of 250 mm × 250 mm)

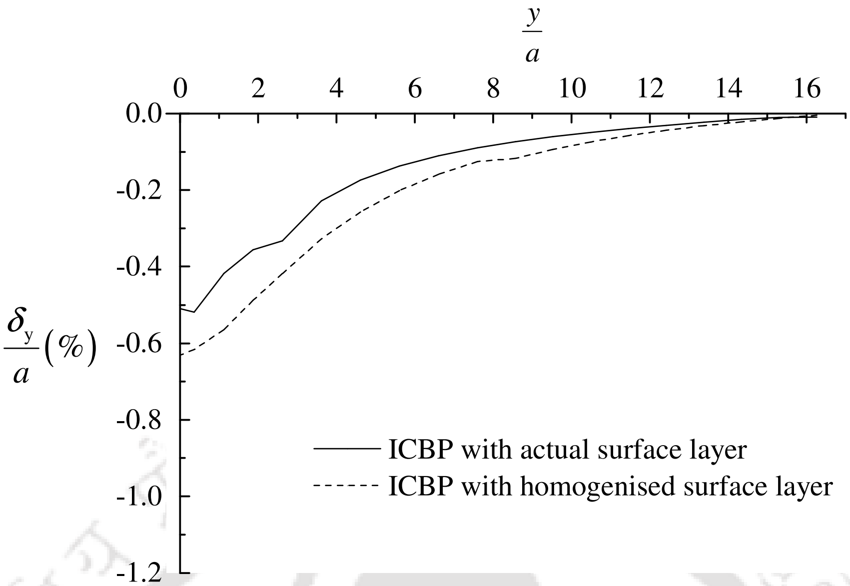

Figure 5.34: Displacement along the depth of simulated ICBP with confined bedding layer (geocell opening size of 150 mm × 150 mm)

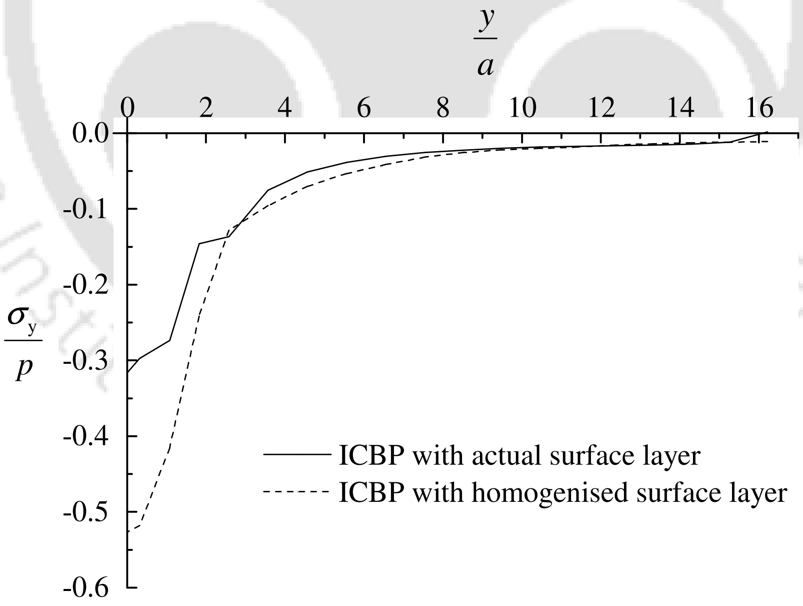

Figure 5.35: Vertical stress along the depth of simulated ICBP with unconfined bedding layer

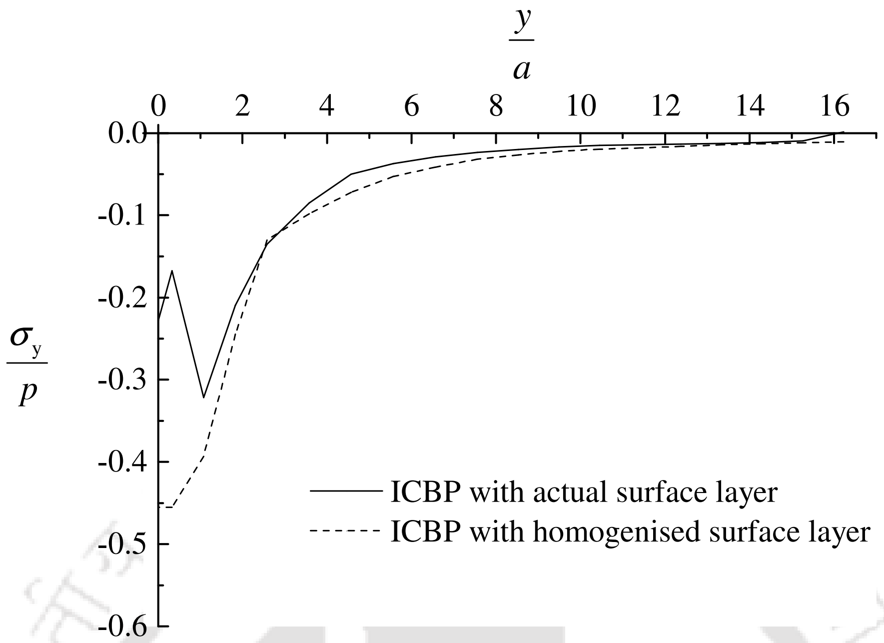

Figure 5.36: Vertical stress along the depth of simulated ICBP with confined bedding layer (geocell opening size of 350 mm × 350 mm)

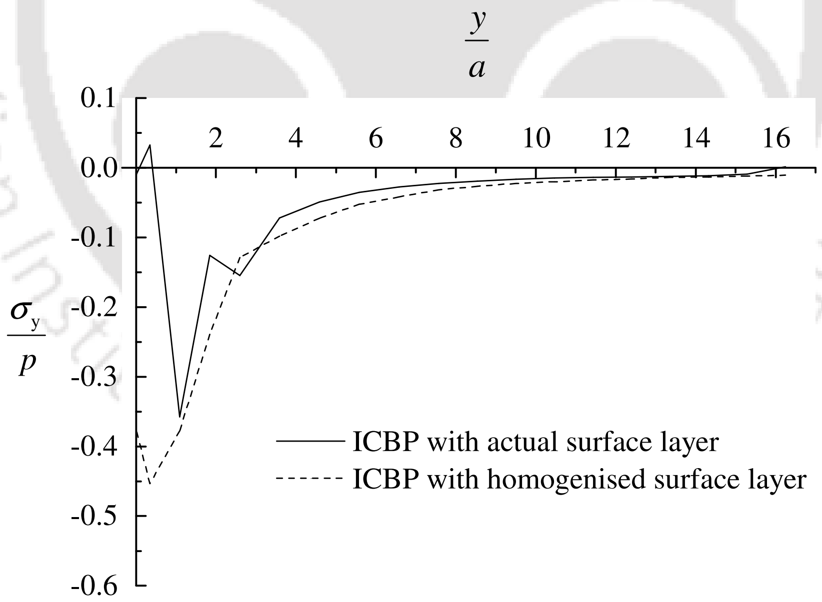

Figure 5.37: Vertical stress along the depth of simulated ICBP with confined bedding layer (geocell opening size of 250 mm × 250 mm)

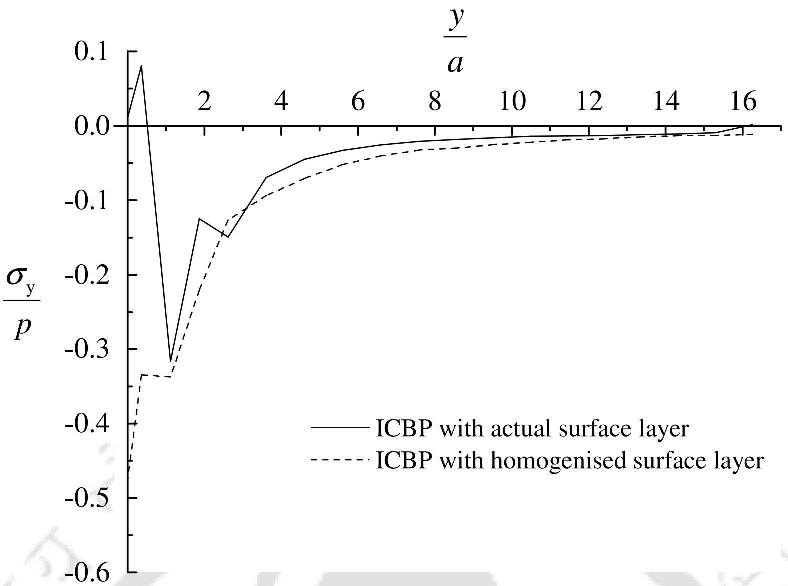

Figure 5.38: Vertical stress along the depth of simulated ICBP with confined bedding layer (geocell opening size of 150 mm × 150 mm)

There is a smooth transition of displacement, in which the slope of the curves for the displacement under the surface layers are trailing similarly. The gap between the two displacement curves may be accounted from a computational perspective, which may be contributed by the irregular distribution of the constituents within the RVE.

However, the stress formulated at the mesh nodes are highly sensitive to the displacement value. This can be seen by the spikes of stress curves under the actual surface layer, while the stress under the homogenised surface is gradually changing. The variability in plots of vertical stress, may be contributed by the irregular deformation of layer of block units compared to the uniform deformation of a continuous homogenised bed. In other words, the homogenised layer smoothly transfers the stress downwards while the interlocking behaviour of blocks may cause spiked stressing in location where blocks breach the bedding layer. Sometimes the blocks under and around the loading region rotate excessively and punch into the bedding layer.

Surface profiles compiled for simulated ICBP sections are shown in **Figure 5.39** to **Figure 5.42**. As presented in **Figure 5.39**, the uneven surface profile of the actual surface shows the block interlocking that is activated under loading.

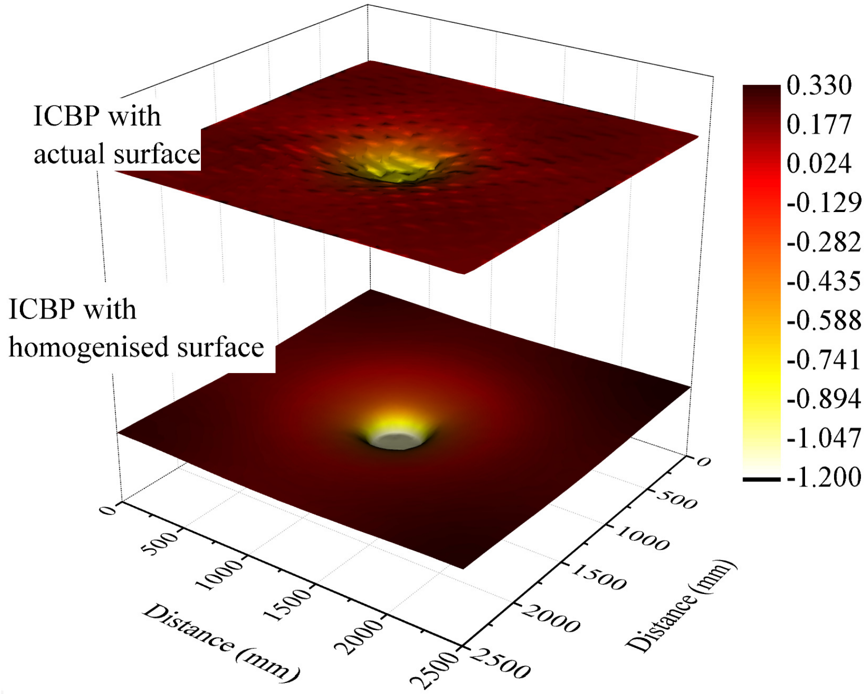

Figure 5.39: Surface profiles of the simulated ICBP with unconfined bedding layer

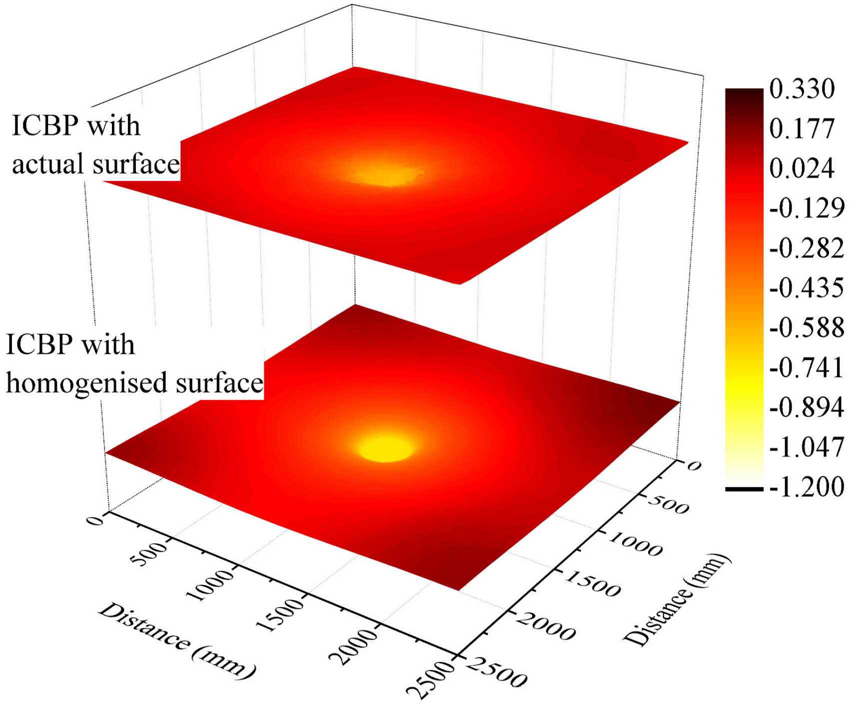

Figure 5.40: Surface profiles of the simulated ICBP with confined bedding layer (geocell opening size of 350 mm × 350 mm)

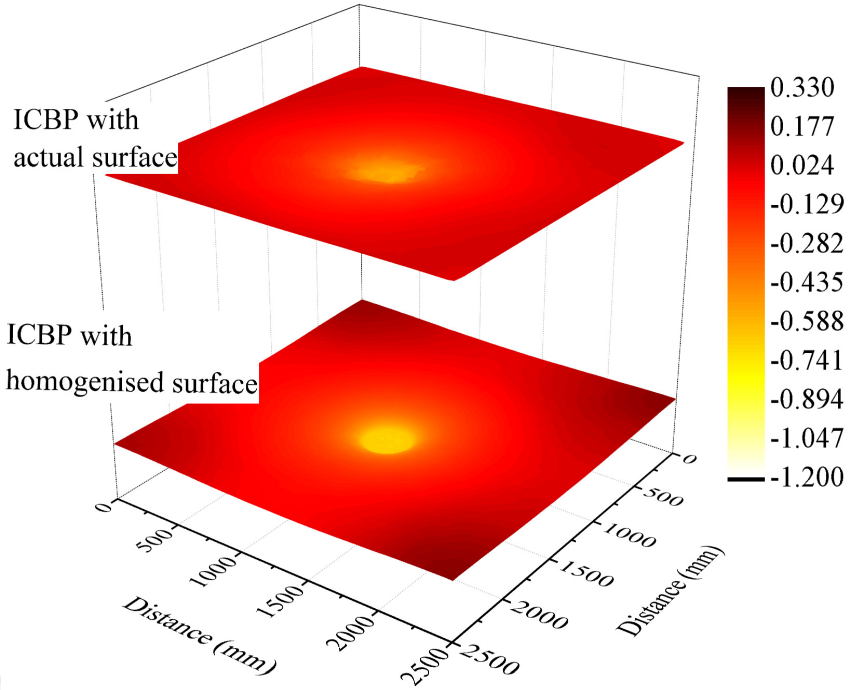

Figure 5.41: Surface profiles of the simulated ICBP with confined bedding layer (geocell opening size of 250 mm × 250 mm)

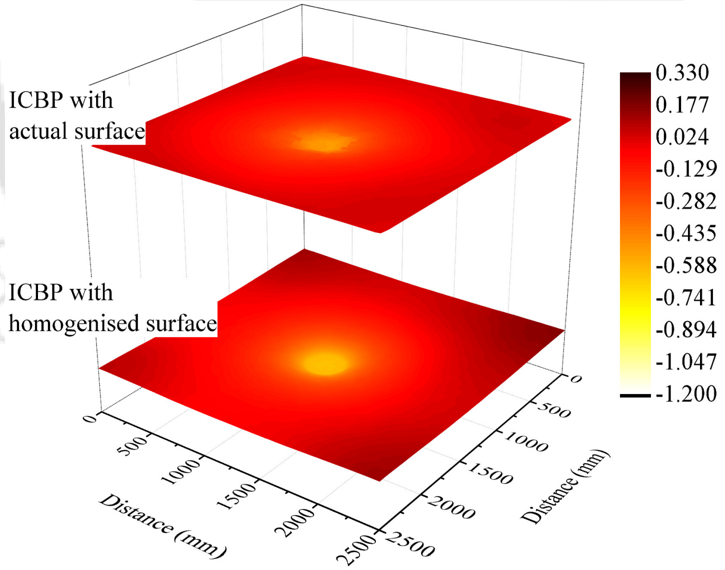

Figure 5.42: Surface profiles of the simulated ICBP with confined bedding layer (geocell opening size of 150 mm × 150 mm)

The high stiffness of the bedding layers prevents excessive deformation on the surface of the ICBP, and with higher stiffness value, the surface is flatter.

5.3.3.3 Verification

The behaviour of concrete block pavement is influenced by loading conditions, loading area, size of test section, block dimensions and shape, block arrangement, joint width, bedding layer thickness, material properties and pavement age. The present study is similar to the study conducted by Taheri et al. (2021) in loading conditions, block dimensions and shape, block arrangement, joint width, and pavement age while the differences are enlisted in **Table 5.10**.

At same applied pressure, the average loading plate's $\frac{\delta_y}{a}$ recorded in existing literature is smaller by 0.305 % in comparison with value obtained in present study.

Table 5.10: Verification of present findings with existing values

Study		**(Taheri et al. 2021)**	**Present Study**
Test Section size		2.0 m × 2.0 m ×0.71 m	2.5 m× 2.5 m× 2.5 m
Loading plate size (mm)		450	300
E (MPa)	Blocks	2000	31622.7766
	Jointing Sand		30.48
	Unconfined Bedding layer	70	18.85
v	Blocks	0.30	0.15
	Jointing Sand		0.3
	Unconfined Bedding layer	0.35	0.23
c (MPa)	Blocks	-	-
	Jointing Sand		Cohesionless
	Unconfined Bedding layer	0.00392	Cohesionless
ϕ (deg.)	Blocks	-	-
	Jointing Sand		40°
	Unconfined Bedding layer	32°	34°
Bedding layer thickness (mm)		30	48.95

The difference may be contributed due to the variation in surface layer stiffness in which shearing about the joints is not considered by the existing study (Noda et al. 2009). Additionally, stress is distributed into a wider area of pavement with a bigger loading plate, along with confinement effect of closer walls, the resistance to deformation is greater

(Mampearachchi and Gunarathna 2010; Panda and Ghosh 2002a). Moreover, a thinner bedding layer is more stable against sand collapse (Panda and Ghosh 2002a).

Investigation is required to ascertain whether the simulation aligns with its intended purpose, thereby ensuring the developed model fulfills the experimental interpretation. To address the quality, efficiency, and correctness of replicating the ICBP sections, the results of the two types of simulation models, i.e., ICBP with actual surface layer and ICBP with a homogenised surface layer are compared with experimental findings and in relation to one another.

The surface profile results shown in **Figure 5.3** to **Figure 5.7** are the averages of displacement recorded at three locations. Here, vertical displacement readings are measured across the width of the test pit. For verification of these experimental results, two more locations are randomly selected in area on surface away from the three initial locations. The same load values are applied onto the loading plate at the two locations, viz., Location 1 and Location 2, and in these two locations only displacement on plate is measured. The deviation measured between the experimental averages with the two location findings are listed as $\frac{\delta_y}{a}$ in **Table 5.11**.

Table 5.11: Verification of experimental results

		Location 1			Location 2		
	Location on plate	MAE (%)	RMSE (%)	ME (%)	MAE (%)	RMSE (%)	ME (%)
Unconfined bedding layer	Left	0.020	0.025	0.0003	0.030	0.039	0.008
	Right	0.077	0.087	-0.078	0.080	0.101	-0.066
Confined bedding layer with geocell opening size							
350 mm × 350 mm	Left	0.071	0.081	-0.072	0.042	0.047	-0.034
	Right	0.014	0.019	0.012	0.042	0.046	-0.042
250 mm × 250 mm	Left	0.011	0.020	-0.010	0.064	0.076	0.064
	Right	0.038	0.041	0.0007	0.087	0.106	0.087
150 mm × 150 mm	Left	0.030	0.037	0.027	0.035	0.045	0.035
	Right	0.035	0.048	-0.035	0.028	0.034	0.028

Similarly, the simulated results are validated with the two location findings to ensure uniformity in execution of FEM models. **Table 5.12** listed the differences in scaled displacement values, $\frac{\delta_y}{a}$ between experimental records at the two locations and the simulated results of ICBP sections with actual surface layer. Similarly, comparison is calculated for ICBP sections with a homogenised surface layer and scaled deviations are listed in **Table 5.13**.

Table 5.12: Validation of ICBP with actual surface layer

	Location 1		Location 2	
	Left	Right	Left	Right
Bedding Layer	**MAE (%)**		**MAE (%)**	
Unconfined Bedding Layer	0.033	0.020	0.060	0.120
Confined bedding layer with geocell of opening size				
350 mm × 350 mm	0.060	0.013	0.073	0.066
250 mm × 250 mm	0.026	0.033	0.120	0.120
150 mm × 150 mm	0.013	0.100	0.020	0.013

Table 5.13: Validation of ICBP with homogenised surface layer

	Location 1		Location 2	
	Left	Right	Left	Right
Bedding Layer	**MAE (%)**		**MAE (%)**	
Unconfined Bedding Layer	0.340	0.293	0.313	0.193
Confined bedding layer with geocell of opening size				
350 mm × 350 mm	0.233	0.133	0.100	0.186
250 mm × 250 mm	0.140	0.113	0.046	0.026
150 mm × 150 mm	0.153	0.246	0.146	0.133

Table 5.14: Comparison of simulated and experimental ICBP sections results.

	ICBPs with actual surface			ICBPs with homogenised surface		
Bedding Layer	**MAE (%)**	**RMSE (%)**	**ME (%)**	**MAE (%)**	**RMSE (%)**	**ME (%)**
Unconfined Bedding Layer	0.106	0.173	0.066	0.160	0.193	0.086
Confined bedding layer with geocell of opening size						
350 mm × 350 mm	0.080	0.120	0.066	0.120	0.146	0.113
250 mm × 250 mm	0.073	0.100	0.053	0.113	0.140	0.106
150 mm × 150 mm	0.073	0.106	0.060	0.120	0.146	0.113

To assess the accuracy of the FEM models in replicating experimental observations, the comparison between simulated results with experimental findings is illustrated in **Table 5.14**.

The comparison focuses on the maximum differences in adjusted vertical displacement, $\frac{\delta_y}{a}$ recorded across the surface.

Quantifying the replication of the discrete surface by an equivalent uniform and homogeneous material, the average differences between the adjusted vertical displacement, $\frac{\delta_y}{a}$ and vertical stress, $\frac{\sigma_y}{p}$ between the FEM models that are shown in **Figure 5.31** to **Figure 5.34** and **Figure 5.35** to **Figure 5.38** respectively, are calculated, and given in **Table 5.15** and **Table 5.16**.

Table 5.15: Comparison between the simulated displacement measured along the depth

Bedding Layer	MAE (%)	RMSE (%)	ME (%)
Unconfined Bedding Layer	0.053	0.093	0.046
Confined bedding layer with geocell of opening size			
350 mm × 350 mm	0.046	0.066	0.046
250 mm × 250 mm	0.046	0.066	0.046
150 mm × 150 mm	0.053	0.073	0.053

Table 5.16: Comparison between the simulated vertical stress measured along the depth

Bedding Layer	MAE (%)	RMSE (%)	ME (%)
Unconfined Bedding Layer	3.53	8.84	3.53
Confined bedding layer with geocell of opening size			
350 mm × 350 mm	3.53	8.84	3.53
250 mm × 250 mm	5.30	14.14	5.30
150 mm × 150 mm	7.07	14.14	5.30

5.3.4 Mesh sensitivity

Mesh sensitivity in foundation is assessed by adjusting the mesh size by specifically selecting the range 0.1 to 0.6 times the global element size. Global element size is a default element size specified for the part.

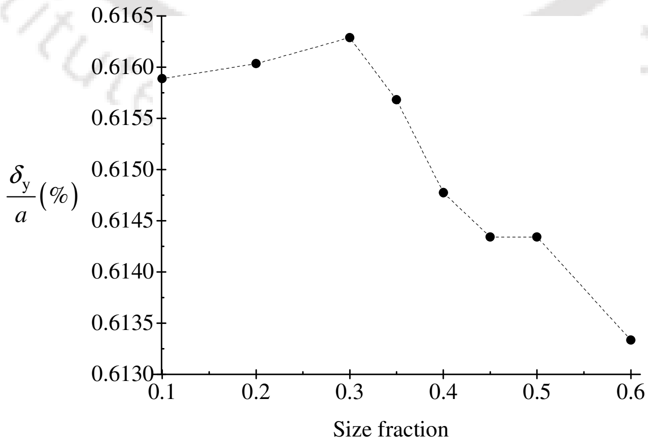

Figure 5.43: Mesh sensitivity of foundation model

Figure 5.43 illustrates the responses obtained from a simulated model of the foundation based on the selected mesh sizes. Notably across the range of mesh sizes, the deviation of displacement values from experimental measurement remains consistently below 0.49 %. Consequently, selecting any mesh size within the specified range yields minimal variations, indicating a negligible influence on the outcomes.

Since it is observed there is less change to measured displacements for mesh sizes of foundation layer, the two-layered system is directly simulated for determination of E_{base}. The selected mesh sizes for the base layer in the two-layer system is deemed sufficient and have been validated through response analysis.

Mesh sensitivity of the RVE is conducted to assess the impact of variation in element size, meshing generation algorithm, and interface interaction property. Element sizes for meshing are considered for global element seed sizes 2.8 mm to 10 mm. Meshing technique employed is sweep meshing, where hexahedral elements are swept from the start to the end face. Sweep meshing technique involves two mesh generation algorithms: (i) initial decomposition of the region into simpler segments prior meshing, and (ii) Generating elements at the region's boundary and systematic progression of element generation towards interior of the region. Across the ranges and types of these parameters, the material elastic property along the direction of loading remains consistent. The standard deviation of the elastic modulus is calculated at 0.3 MPa with a coefficient of variation is 0.001 %. The consistency of the representing and replacement the surface layer with a homogenised is listed in **Table 5.15** and **Table 5.16**.

The current wall clock time required to execute solutions for ICBP sections with actual surface layer is at least 12 times greater than that for ICBP sections with homogenised surface layer. Consequently, mesh sensitivity check is omitted for the former sections and is exclusively performed for the latter sections. The association between the two simulation models, as evidenced by **Table 5.15** and **Table 5.16**, supports the inference of a suitable mesh size selection for the ICBP featuring an actual surface layer. Mesh sensitivity for ICBP with a homogenised surface layer is shown in **Figure 5.44**, in which the range is 0.43 to 1.5 times the global element sizes. The mesh sensitivity is trivial with mesh size smaller than 0.5 times the global mesh sizes. For models consisting of the three smaller mesh sizes the standard deviation is 0.003 % and coefficient of variation is 0.232 %. Considering saving in computation time, a mesh size of 0.5 times the global element sizes is selected for further structural analysis.

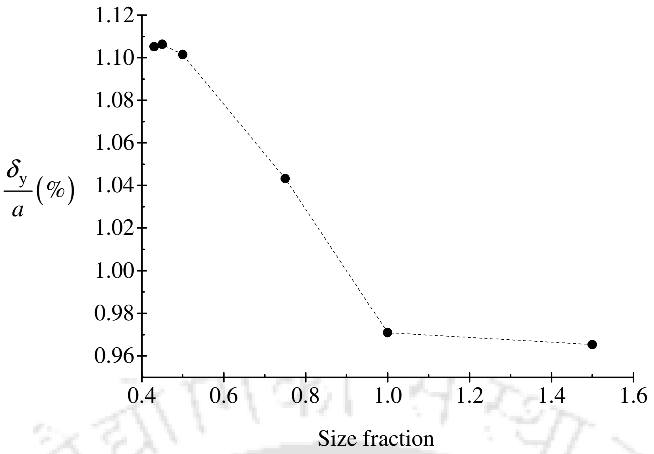

Figure 5.44: Mesh sensitivity of ICBP

5.3.5 Adoption of micromechanical analysed homogenisation

From a design standpoint, accurately modeling the precise geometries of an ICBP section poses significant challenges, requiring laborious efforts to define the geometry and arrangement. The process is further complicated by analytical complexities and the susceptibility to numerous errors, resulting in a time-consuming and prolonged simulation. To address these issues, homogenising the material of the composite surface layer into an equivalent homogeneous, anisotropic material proves effective in streamlining the complexities and expediting the solution. It is noteworthy, the surface layer, composed of blocks arranged in a 90° herringbone with joints filled with recommended sand, can be accurately represented by a single, uniform, and orthotropic elastic layer. Moreover, the homogenised orthotropic surface layer successfully anticipates the behaviour of the actual surface, including the presence of jointing sand exhibiting elasto-plastic characteristics. Besides, cutting the uncertainty of convergence errors occurring, the ICBP with a homogenised surface layer decreases the simulation clock time by a factor of 12 compared to considering the layer with individual blocks and jointing sands.

Chapter 6. Conclusion and Discussion

6.1 General

The conclusion chapter encapsulates the key findings and insights derived from the preceding chapters. In this section, a review of the main outcomes will address the research objectives establish at the outset.

In this study, the characterisation of the bedding layer as a non-structural member of the ICBP is revised and substantiated to demonstrate its inherent structural capabilities. Positioned in a highly stressed region within the ICBP, the bedding can be susceptible to premature deformation. However, with implementation of confinement, the collapse of the bedding sand will be arrested within the geocells walls.

Considering the preceding chapter of experimental investigation and numerical analysis, the following general conclusion is enlisted:

1. The experimental structural evaluation test considered, reflects the performance of the pavement under the initial loading, which is projected to pavement performance immediately after construction.
2. Geocell reinforcement engages various factors such as the confinement effect, frictional action of the sand with geocell walls, passive resistance by adjacent cells, tensioned membrane effect and overall geocell mat slab action. Attempting to replicate the geocell-reinforced bedding layer by introducing confinement induced "apparent cohesive strength" is insufficient, as the slab action of geocell mat could also be activated.
3. Macroscopically homogenising the surface layer and including the bedding layer as an isotropic and uniform single layer, does not accurately predict the actual behaviour of the ICBP section. The reason may be under current loading and layer conditions this equivalent composite approach cannot effectively encompass plastic deformation in bedding layer.
4. Therefore, the ICBPs are modelled with actual geometries as accurately as possible to capture the complex behaviour of each part.

The present study demonstrates that confining the bedding sand within geocells improves the structural efficacy of the bedding layer, consequently contributing to an overall enhancement of the ICBP response. The improvement is attributed to the stabilisation of the riding surface, particularly in mitigating larger deformation. Through the comprehensive examination involving the experimental and numerical analysis of the ICBP sections, an insight into the established results will be discussed henceforth.

6.2 Structural influence of the bedding layer

The main function of the bedding layer lies in serving as a cushion for positioning the blocks and preventing crack propagation within the ICBP system. An essential aspect of providing the bedding layer is that the thin sand bed is purportedly a non-structural member of the ICBP. Pertaining to its location in the ICBP, the layer is susceptibility to early shear failure and potentially affecting the system stability. A collapsing sand bed can trigger the blocks dislocation, leading to a subsiding riding surface. Therefore, enhancing the stability of the bedding layer by stabilisation, and provision of geocells will delay the sand collapse. The improvement in bedding layer stiffness is evident in improved field responses of the ICBP sections, ergo, the bedding layer exerting influence on the ICBP stability. The following observations suggest the influence of the confinement, converting the cushion bed to a structural component of the ICBP:

1. Modelling the ICBP with unconfined bedding layer and treating the bedding sand as an elasto-plastic material suggest that the layer undergoes plastic deformation during the initial loading stage.
2. The incorporation of geocells, strategically placed within the region of load dispersion under the loading location, has effectively capsized the early failure of the bedding layer.
3. It is observed for the current loading conditions that the confined bedding layer experiences elastic behaviour.
4. Inclusion of geocell enhances the resistance of the bedding layer to deformation, as evidenced by the minimum reduction of about 21 % in displacement.
5. In other words, the incorporation of geocells improves the stiffness of the bedding layer, which is supported by a fivefold increase in the equivalent elastic modulus of the bedding layer when utilising the adopted maximum sizes of geocells.

6.3 Influence of geocell sizes on pavement response

Closer the geocell walls to each other, the greater is the equivalent stiffness of the confined layer. Close wall proximity promptly activates the confinement effect, with high density of geocell within the region creating higher magnitude of frictional resistance at multiple interfaces, greater slab action due to denser geocell mat and multiple geocell walls, by activating tensioned membrane effect. The following observations show the influence of the cell density or in other words, reduction in geocell size openings on the structural behaviour of the ICBP.

1. Reduction in displacement, measured during experiments for geocell with cell openings, 350 mm × 350 mm, 250 mm × 250 mm and 150 mm × 150 mm are 27.77 %, 36.62 % and 43.21 % respectively.
2. The effect of geosynthetic inclusion and the influence of geocell sizes on the layer property is measured in terms of modulus improvement factor (MIF). Improvement to stiffness of the bedding layer with inclusion of geocells is corroborated by MIF>1,
3. MIFs for geocell with cell openings, 350 mm × 350 mm, 250 mm × 250 mm and 150 mm × 150 mm are 5.09, 13.26 and 37.13 respectively.

6.4 Homogenisation of the ICBP composite surface

The challenges regarding the design perspective for ICBP modelled to its exact geometries is it is labour-intensive to define the parts geometry and their arrangement. The computational analysis encounters complexities and prone to numerous errors. Consequently, the simulation becomes time- consuming. Hence, homogenising the material of composite surface layer to an equivalent homogeneous, anisotropic material curtails complexities and delivering a faster solution. Two ways homogenisation are attempted, in which macroscopically or homogenising the complete surface layer and bedding layer into a single, uniform and isotropic elastic layer is insufficient to predict the experimental responses. Therefore, engaging homogenisation using micromechanics is deemed satisfactory. The following observations are executed from structural analysis of ICBP with a homogenised surface layer:

1. The surface layer, consisting the blocks arranged in a 90° herringbone with joints filled in with a recommended sand can be replicated by a uniform, homogeneous, orthotropic elastic layer.

2. The homogenised orthotropic surface layer predicts likewise the behaviour of the actual surface consisting jointing sand, which possesses elasto-plastic behaviour.
3. Projection of microscale equivalent property is influenced by the size of the RVE.
4. The responses in terms of displacement underneath the surface layer streams in similar pattern. However, due to the blocks rotation and puncturing into the bedding layer, the stress distribution under the blocks is not similar than under the homogenised layer.
5. Simulation of ICBP section with a homogenised surface layer reduces the simulation clock-time by 12 times than considering the layer with blocks and jointing sand.

Chapter 7. Limitations and Recommendations

The study investigates into the consequences of redefining the conventional view of bedding layer as merely a cushion for seating the blocks and for arresting crack propagation. The present study conducted an initial investigation into stabilising the bedding layer alone, shedding light on how it affects the behavior of ICBP. However, some of the limitations and potential future scope for research in this study are listed below:

- In this study, discrete modelling of the ICBP sections is conducted only for the surface layer. The bedding layer is posited as a uniform and homogeneous bed, featuring an improved equivalent material property in confined condition. By exclusively considering discrete modelling of the geocell and infill material, it becomes possible to predict the complex response of the reinforcement effect due to varying conditions of the geomaterial, geocell, and infill material. A detailed assessment of the influence of the geocell on the overall behavior of ICBP could also be adequately carried out through extensive parametric investigation.
- The compacted thickness of bedding layer is taken to the maximum value recommended in the earlier version of IRC specifications. There is a scope of evaluating the efficacy of geocell reinforcement in thinner bedding layer.
- Due to constraint for compaction of bedding sand prior block arrangement, the sand is compacted to desired thickness by running the compaction machine on the block surface. If availability of a larger test area, vibratory compaction could be carried out longitudinally without excavating the bedding sand around the small test area. The capability to directly compact the bedding sand layer enables the easy achievement of the desired thickness and density, making it feasible to implement geocells with smaller opening sizes.
- The present study is conducted in controlled testing conditions to replicate the pavement response during the initial phase of its service life. Therefore, there is a scope for further research into the long-term performance of ICBP with the confined bedding layer.
- Geocell can be implemented within the bedding layer in situations when marginal bedding sand are available.

Publication

Patent

Patent titled “SYSTEMS AND METHODS FOR CONFINING BEDDING SAND IN INTERLOCKING CONCRETE BLOCK PAVEMENT BY GEOCELLS”

Provisional Patent Application No.: 202331049472 dated 20.07.2023

Book Chapter

Sohlang, Ibaiahun N., Shallam, Regulus Dominic K. Contaminant Reduction in stormwater infiltrated through pervious concrete pavement. *Pervious Concrete Pavements*. Elsevier (Under Review)

References

1. Aboudi, J. (2004). "The generalized method of cells and high-fidelity generalized method of cells micromechanical models - A Review." *Mechanics of Advanced Materials and Structures*, 11(4–5), 329–366.
2. Aboudi, J., and Pindera, M.-J. (1992). *Micromechanics of Metal Matrix Composites Using the Generalized Method of Cells Model (GMC) User's Guide. NASA Contractor Report 190756.*
3. Al-Qadi, I. L., and Hughes, J. J. (2000). "Field evaluation of geocell use in flexible pavements." *Transportation Research Record*, 1(1709), 26–35.
4. Ali, M., Sayet, T., Gasser, A., and Blond, E. (2021). "Computational homogenization of elastic-viscoplastic refractory masonry with dry joints." *International Journal of Mechanical Sciences*, Elsevier Ltd, 196, 106275.
5. Altman, D. G., and Bland, J. M. (1983). "Measurement in Medicine : The Analysis of Method Comparison Studies." *Journal of the Royal Statistical Society. Series D (The Statistician)*, 32(3), 307–317.
6. Álvarez-Barrientos, F., Hurtado, D. E., and Genet, M. (2021). "Pressure-driven micro-poro-mechanics: A variational framework for modeling the response of porous materials." *International Journal of Engineering Science*, 169, 103586.
7. Arjun Siva Rathan, R. T. B., Sunitha, V., and Janani, L. (2023). "Evaluation of Structural and Functional Performance of Interlocking Concrete Block Pavement and Flexible Pavement." *Journal of Testing and Evaluation*, 51(6), 3968–3985.
8. Arjun Siva Rathan, R. T., and Sunitha, V. (2022a). "Development of Deflection Prediction Model for Interlocking Concrete Block Pavements." *Transportation Research Record*, 2676(3), 292–314.
9. Arjun Siva Rathan, R. T., and Sunitha, V. (2022b). "Development of design procedure for interlocking concrete block pavement." *International Journal of Pavement Engineering*, 23(14), 5015–5029.
10. Arjun Siva Rathan, R. T., and Sunitha, V. (2022c). "Development of effective wearing layer elastic modulus for interlocking concrete block pavements." *Construction and Building Materials*, Elsevier Ltd, 341.
11. Arjun Siva Rathan, R. T., Sunitha, V., and Anusudha, V. (2022a). "Parametric study to investigate the deflection and stress behaviour of Interlocking Concrete Block Pavement." *Road Materials and Pavement Design*, 23(10), 2293–2316.
12. Arjun Siva Rathan, R. T., Sunitha, V., Murshida, P., and Anusudha, V. (2022b). "Influence of bedding and jointing sand on the shear strength characteristics of Interlocking Paver Blocks–bedding sand interface." *International Journal of Pavement Engineering*, 23(7), 2160–2175.
13. Arjun Siva Rathan, R. T., Sunitha, V., Pathath, M., Lekshmipathy, J., and Visvanathan, A. (2021). "Experimental and Numerical Evaluation of the Parameters Influencing the Shear-Stress Behavior of Interlocking Paver Blocks–Bedding Sand Interface Using Large-Scale Direct Shear Test." *Journal of Materials in Civil Engineering*, 33(6).

14. Arnold, S. M., Bednarcyk, B. A., Wilt, T. E., and Trowbridge, D. (1999). *Micromechanics Analysis Code With Generalized Method of Cells (MAC/GMC) User Guide: Version 3.0*.
15. Arslan, A., Gümüş, M., and Ünal, E. (2022). "Effect of support conditions on the performance of B70 sleeper overlying reinforced ballast and sub-ballast layer: Experimental and analytical investigation." *Transportation Geotechnics*, 37.
16. Ascher, D., Lerch, T., Oeser, M., and Wellner, F. (2006). "3D-FEM simulation of concrete block pavements." *Eighth International Conference on Concrete Block Paving*, San Francisco, California, USA, 457–466.
17. ASTM. (2018). *ASTM D882-18 -Standard Test Method for Tensile Properties of Thin Plastic Sheeting*. American Society for Testing and Materials, West Conshohocken, Pennsylvania, USA.
18. ASTM. (2019). *ASTM D5199-12(2019) -Standard Test Method for Measuring the Nominal Thickness of Geosynthetics. American Society for Testing and Material*, American Society for Testing and Materials, West Conshohocken, Pennsylvania, USA.
19. ASTM. (2021). *ASTM D1195/D1195M Standard Method of Test for Repetitive Static Plate Load Tests of Soils and Flexible Pavement Components for Use in Evaluation and Design of Airport and Highway Pavements*. American Society for Testing and Materials, West Conshohocken, Pennsylvania, United States.
20. Baadiga, R., Saride, S., Balunaini, U., and Madhira, M. R. (2021). "Influence of tensile strength of geogrid and subgrade modulus on layer coefficients of granular bases." *Transportation Geotechnics*, 29, 100557.
21. Banerjee, L., Chawla, S., and Dash, S. K. (2023). "Investigations on cyclic loading behavior of geocell stabilized tracks with coal overburden refuse recycled as subballast material." *Transportation Geotechnics*, Elsevier Ltd, 40.
22. Barber, S. D., and Knapton, J. (1980). "Structural Design of Block Pavements for Ports." *First International Conference on Concrete Block Paving*, Newcastle, England, 141–149.
23. Bathurst, R., and Karpurapu, R. (1993). "Large-Scale Triaxial Compression Testing of Geocell-Reinforced Granular Soils." *Geotechnical Testing Journal*, 16(3), 296–303.
24. Béguin, P., and Aubert, J. P. (1994). "The biological degradation of cellulose." *FEMS Microbiology Reviews*, 13(1), 25–58.
25. Beld, H. v. d., and Duiven, P. H. (1984). "Maintenance Planning System for Block Pavements." *2nd International Conference on Concrete Block Paving*, Delft, Netherlands, 246–262.
26. Beran, M. (1965). "Statistical Continuum Theories." *Transactions of the Society of Rheology*, 9(1), 339–355.
27. Berechman, J. (2003). "Transportation — economic aspects of Roman highway development : the case of Via Appia." *Transportation Research: Part A*, 37, 453–478.
28. BIS. (1970). *IS 1498 (Reaffirmed 2011) Classification and Identification of Soils for General Engineering Purposes (First Revision)*. Bureau of Indian Standards, New Delhi, India.

29. BIS. (1974). *IS 2720 Part 28 (Reaffirmed 2010) Methods of test for soils-Determination of dry density of soils in-place by the sand replacement method*. Bureau of Indian Standards, New Delhi, India.
30. BIS. (1983). *IS 2720 Part 14 (Reaffirmed 2006) Methods of test for soils: determination of density index (relative density) of cohesionless soils*. Bureau of Indian Standards, New Delhi, India.
31. BIS. (2000). *IS 456: 2000 for Plain and Reinforced Concrete-Code of Practice*. Bureau of Indian Standards, New Delhi, India.
32. BIS. (2002). *IS 2720 Part 11 Determination of The Shear Strength Parameters of a Specimen Tested In Unconsolidated Undrained Triaxial Compression Without The Measurement Of Pore Water Pressure*. *Public Works*, Bureau of Indian Standards, New Delhi, India.
33. BIS. (2006). *IS 15658:2006 Precast Concrete Block for Paving-Specification*. Bureau of Indian Standards, New Delhi, India.
34. Böhm, H. J., Pahr, D. H., and Daxner, T. (2010). “Analytical and Numerical Methods for Modeling the Thermomechanical and Thermophysical Behavior of Microstructured Materials.” *Computational and Experimental Mechanics of Advanced Materials.*, V. V. Silberschmidt, ed., Springer, Vienna, 167–223.
35. Cairns, J., and Gregory, G. (2006). “A Case for the Preferential Use of Concrete Block Paving in Residential Streets.” *Eighth International Conference on Concrete Block Paving*, San Francisco, California, USA, 583–588.
36. Casparie, W. A., and Moloney, A. (1994). “Neolithic wooden trackways and bog hydrology.” *Journal of Paleolimnology*, 12, 49–64.
37. Choi, H. J., and Thangjitham, S. (1991). “Micro- and macromechanical stress and failure analyses of laminated composites.” *Composites Science and Technology*, 40(3), 289–305.
38. Chua, K. M., Askree, Z., and Shackel, B. (2000). “Axisymmetric Finite Element Modeling of Block Pavement Subjected to Repeated Loading.” *Transportation Research Record*, 1730(1), 53–63.
39. Clough, R. W. (1980). “The finite element method after twenty-five years: A personal view.” *Computers and Structures*, 12, 361–370.
40. Clough, R. W., and Wilson, E. L. (1999). “Early Finite Element Research in Berkeley.” *Fifth U.S. National Conference on Computational Mechanics*, U.S. Association for Computational Mechanics, Boulder, Colorado, 1–35.
41. Dash, S. K., Rajagopal, K., and Krishnaswamy, N. R. (2007). “Behaviour of geocell-reinforced sand beds under strip loading.” *Canadian Geotechnical Journal*, 44(7), 905–916.
42. Deshmukh, R., Patel, S., and Shahu, J. T. (2022). “Full-Scale Field Performance of Geocell Reinforced-Fly Ash in the Subbase Course of Flexible Pavement.” *International Journal of Geosynthetics and Ground Engineering*, Springer International Publishing, 8(3).
43. Deshmukh, R. R., Patel, S., and Shahu, J. T. (2021). “Field assessment of improvement in composite modulus of geosynthetic-reinforced pavements.” *Geosynthetics International*, 28(6), 624–633.

44. Drugan, W. J., and Willis, J. R. (1996). “A micromechanics-based nonlocal constitutive equation and estimates of representative volume element size for elastic composites.” *Journal of the Mechanics and Physics of Solids*, 44(4), 497–524.

45. Duncan, J. M., and Chang, C. Y. (1970). “Parametric finite element analyses of geocell-supported embankments.” *Journal of the Soil Mechanics and Foundations Division*, 96(5), 1629–1653.

46. Eisenmann, J., and Leykauf, G. (1988). “Design of concrete block pavement in FRG.” *4th International Conference on Concrete Block Paving*, Rome, Italy, 149–155.

47. Eshelby, J. D. (1957). “The determination of the elastic field of an ellipsoidal inclusion, and related problems.” *Proceedings of the Royal Society of London. Series A, Mathematical and Physical Sciences*, 241(1226), 376–396.

48. Füssl, J., Hengl, H., Eberhardsteiner, L., Kluger-Eigl, W., and Blab, R. (2018). “Numerical simulation tool for paving block structures assessed by means of full-scale accelerated pavement tests.” *International Journal of Pavement Engineering*, 19(10), 917–929.

49. Füssl, J., Kluger-Eigl, W., and Blab, R. (2016). “Experimental identification and mechanical interpretation of the interaction behaviour between concrete paving blocks.” *International Journal of Pavement Engineering*, Taylor & Francis, 17(6), 478–488.

50. Gao, B., Liu, X., Liu, J., Song, L., Shi, Y., and Yang, Y. (2023). “Field Characterization of Dynamic Response of Geocell-Reinforced Aeolian Sand Subgrade under Live Traffic.” *Applied Sciences 2023*, 13(2).

51. Garcia, R. S., and Neto, J. O. A. (2021). “Stress-dependent method for calculating the modulus improvement factor in geocell-reinforced soil layers.” *Geotextiles and Geomembranes*, Elsevier Ltd, 49(1), 146–158.

52. Gedela, R., and Karpurapu, R. (2021). “Laboratory and Numerical Studies on the Performance of Geocell Reinforced Base Layer Overlying Soft Subgrade.” *International Journal of Geosynthetics and Ground Engineering*, Springer International Publishing, 7, Article.

53. Geense, C. W. A. (1980). “The Re-use of Concrete Paving Blocks, Mechanical Laying in Rotterdam.” *First International Conference on Concrete Block Paving*, University of Newcastle-Upon-Tyne, England, 354–363.

54. Giroud, J. P., and Han, J. (2004). “Design Method for Geogrid-Reinforced Unpaved Roads. I. Development of Design Method.” *Journal of Geotechnical and Geoenvironmental Engineering*, 130(8), 775–786.

55. Goud, G. N., Ramu, B., Umashankar, B., Sireesh, S., and Madhav, M. R. (2022). “Evaluation of layer coefficient ratios for geogrid-reinforced bases of flexible pavements.” *Road Materials and Pavement Design*, Taylor & Francis, 23(1), 199–210.

56. Gunatilake, D., and Mampearachchi, W. K. (2014). “Development of a Finite Element Model for Concrete Block Paving.” *9th Asia Pacific Conference on Transportation and the Environment*, Colombo, Sri Lanka, 44–55.

57. Gunatilake, D., and Mampearachchi, W. K. (2019). “Finite element modelling approach to determine optimum dimensions for interlocking concrete blocks used for road paving.” *Road Materials and Pavement Design*, 20(2), 280–296.

58. Haeri, S. M., Noorzad, R., and Oskoorouchi, A. M. (2000). “Effect of geotextile reinforcement on the mechanical behavior of sand.” *Geotextiles and Geomembranes*, 18(6), 385–402.

59. Han, J., Pokharel, S. K., and Parsons, R. L. (2010). “Effect of infill material on the performance of geocell-reinforced bases.” *9th International Conference on Geosynthetics*, São Paulo, Brazil, 1503–1506.

60. Han, J., Yang, X., Leshchinsky, D., and Parsons, R. L. (2008). “Behavior of geocell-reinforced sand under a vertical load.” *Transportation Research Record*, 2045, 95–101.

61. Hand, L. N., and Finch, J. D. (1998). *Analytical Mechanics*. Cambridge University Press, Cambridge CB2 1RP, United Kingdom.

62. Hashin, Z. (1983). “A self-consistent mechanics of composite materials.” *Analysis of Composite Materials- A Survey*, 50(3), 481–505.

63. Hassani, A., and Jamshidi, A. (2006). “Modeling and Structural Design of a Concrete Block Pavement System.” *Eighth International Conference on Concrete Block Paving*, California, USA, 389–398.

64. Hausmann, M. R. (1987). “Geotextiles for unpaved roads-A review of design procedures.” *Geotextiles and Geomembranes*, 5(3), 201–233.

65. Haviv, S., Ishai, I., and Argaman, G. (2009). “The City of Eilat is Going for Concrete Block Paving.” *Ninth International Conference on Concrete Block Paving*, Buenos Aires, Argentina, 1–12.

66. He, Z., and Pindera, M. J. (2021). “Finite volume based asymptotic homogenization theory for periodic materials under anti-plane shear.” *European Journal of Mechanics-A/Solids*, Elsevier Masson SAS, 85, 104122.

67. Hedge, A., and Sitharam, T. G. (2015a). “Three-dimensional numerical analysis of geocell-reinforced soft clay beds by considering the actual geometry of geocell pockets.” *Canadian Geotechnical Journal*, 52(9), 1396–1407.

68. Hedge, A., and Sitharam, T. G. (2015b). “3-Dimensional numerical modelling of geocell reinforced sand beds.” *Geotextiles and Geomembranes*, Elsevier Ltd, 43, 171–181.

69. Hegde, A. M., and Sitharam, T. G. (2015). “Effect of infill materials on the performance of geocell reinforced soft clay beds.” *Geomechanics and Geoengineering*, Taylor & Francis, 10(3), 163–173.

70. Hegde, A., and Sitharam, T. G. (2013). “Experimental and numerical studies on footings supported on geocell reinforced sand and clay beds.” *International Journal of Geotechnical Engineering*, 7(4), 346–354.

71. Hengl, H. L., Kluger-Eigl, W., Lukacevic, M., Blab, R., and Füssl, J. (2018). “Horizontal deformation resistance of paving block superstructures – Influence of paving block type, laying pattern, and joint behaviour.” *International Journal of Pavement Research and Technology*, 11, 846–860.

72. Henkel, D. J., and Gilbert, G. D. (1952). “The effect of the rubber membrane on the measured triaxial compression strength of clay samples.” *Géotechnique*, 3(1), 20–29.

73. Henkes, A., Caylak, I., and Mahnken, R. (2021). “A deep learning driven pseudospectral PCE based FFT homogenization algorithm for complex

microstructures." *Computer Methods in Applied Mechanics and Engineering*, Elsevier B.V., 385, 114070.

74. Hill, R. (1965). "A Self-Consistent Mechanics of Composite Materials." *Journal of the Mechanics and Physics of Solids*, 13(4), 213–222.
75. Houben, L. J. M., and Jacobs, M. M. J. (1988). "Wheel track testing and finite element analysis of concrete block pavements." *3rd International Conference on Concrete Block Paving*, Rome, Italy, 102–113.
76. Houben, L. J. M., Molenaar, A. A. A., Fuchs, G. H. A. M., and Molll, H. O. (1984). "Analysis and Design of Concrete Block Pavements." *2nd International Conference on Concrete Block Paving*, Delft, Netherlands, 86–99.
77. Huang, Y. H. (2009). *Pavement analysis and design*. Pearson Education, Inc, Upper Saddle River, New Jersey.
78. Hufenus, R., Rueegger, R., Banjac, R., Mayor, P., Springman, S. M., and Brönnimann, R. (2006). "Full-scale field tests on geosynthetic reinforced unpaved roads on soft subgrade." *Geotextiles and Geomembranes*, 24(1), 21–37.
79. Huurman, M. (1996). "Resilient behaviour of concrete block pavements and the granular materials used in the substructure." *Sixth International Conference on Concrete Block Paving*, Tel-Aviv, Israel, 239–251.
80. Huurman, M., Houben, L. J. M., Geense, C. W. A., and Van der Vring, J. J. M. (2003). "The upgraded Dutch design method for concrete block road pavements." *Seventh International Conference on Concrete Block Paving*, Sun City, South Africa, 21.
81. Huurman, M., Houben, L. J. M., and Kok, A. W. M. (1993). "Development of a three-dimensional finite element model for concrete block pavements." *4th International Conference on Concrete Block PavingI*, Auckland, New Zealand, 89–99.
82. Huurman, M., Houben, L. J. M., Molenaar, A. A. A., and Kok, A. W. M. (1992). "The Shear Failure Mechanism in Concrete Block Pavements with a Sand Sub-Base only." *Fourth International Conference on Concrete Block Paving*, Auckland, New Zealand, 297–307.
83. ICPI. (2007). *Tech Spec 17: Bedding Sand Selection for Interlocking Concrete Pavements in Vehicular Applications (Revised March 2022)*. Concrete Masonry & Hardscapes Association, Virginia, 20171, United States.
84. Indraratna, B., Khabbaz, H., Salim, W., and Christie, D. (2006). "Geotechnical properties of ballast and the role of geosynthetics in rail track stabilisation." *Proceedings of the Institution of Civil Engineers - Ground Improvement*, 10(3), 91–101.
85. Indraratna, B., Nimbalkar, S., Christie, D., Rujikiatkamjorn, C., and Vinod, J. (2010). "Field Assessment of the Performance of a Ballasted Rail Track with and without Geosynthetics." *Journal of Geotechnical and Geoenvironmental Engineering*, 136(7), 907–917.
86. IRC. (2004). *IRC:SP:63-2004 Guidelines for the use of interlocking concrete block pavement*. Indian Roads Congress, New Delhi, India.
87. IRC. (2012). *IRC: 109-1997 Guidelines for Wet Mix Macadam*. Indian Roads Congress, New Delhi, India.

88. IRC. (2015). *IRC 109-2015-Guidelines for Wet Mix Macadam (First Revision)*. Indian Roads Congress, New Delhi, India.

89. IRC. (2018a). *IRC:SP:63-2018 Guidelines for the use of interlocking concrete block pavement (First Revision)*. Indian Roads Congress, New Delhi, India.

90. IRC. (2018b). *IRC: 37-2018 Guidelines for the Design of Flexible Pavements (Fourth Revision)*. Indian Roads Congress, New Delhi, India.

91. IRC. (2019). *IRC: SP:59-2019 Guidelines for use of geosynthetics in road pavements and associated works (First Revision)*. Indian Roads Congress, New Delhi, India.

92. ISO. (2019). *ISO 13426- 1-2019 (E) Geotextiles and geotextile -related products-Strength of internal structural junctions-Part 1: Geocells*. International Organization for Standardization, Geneva, Switzerland.

93. Jalili, M., and Kabiri, M. (2019). "The effect of reinforced soil type on the value of bearing ratio." *16th Asian Regional Conference on Soil Mechanics and Geotechnical Engineering (16ARC)*, Association of Geotechnical Societies in Southeast Asia (AGSSEA), Taipei, Taiwan.

94. Jamshidi, A., Kurumisawa, K., White, G., Nishizawa, T., Igarashi, T., Nawa, T., and Mao, J. (2019). "State-of-the-art of interlocking concrete block pavement technology in Japan as a post-modern pavement." *Construction and Building Materials*, Elsevier Ltd, 200, 713–755.

95. Janbu, N. (1970). "Method of settlement computation for various types of soils." *Soil Mechanics and Foundation Engineering*, 7, 201–206.

96. Jaster, J., Schlesinger, G. F., Crandell, J. S., and Phillips, R. L. (1938). "Developments of Brick Pavements in the United States." *Public Roads: A Journal of Highway Research*, 19(4), 58–60.

97. Javili, A., Saeb, S., and Steinmann, P. (2017). "Aspects of implementing constant traction boundary conditions in computational homogenization via semi-Dirichlet boundary conditions." *Computational Mechanics*, Springer Berlin Heidelberg, 59, 21–35.

98. Jayanthi, V., Soundara, B., Sanjaikumar, S. M., Siddharth, M. A., Shree, S. D., and Ragavi, S. P. (2022). "Influencing Parameters on experimental and theoretical analysis of geocell reinforced soil." *Materials Today: Proceedings*, Elsevier Ltd, 66, 1148–1155.

99. Jeon, Y.-J., Yun, J.-H., and Kang, M.-S. (2022). "Analysis of Elastic Properties of Al/PET Isotropic Composite Materials Using Finite Element Method." *Materials*, 15(22), 8007.

100. Kabiri Kouchaksaraei, M., and Bagherzadeh Khalkhali, A. (2020). "The effect of geocell dimensions and layout on the strength properties of reinforced soil." *SN Applied Sciences*, 2(1701).

101. Kanit, T., Forest, S., Galliet, I., Mounoury, V., and Jeulin, D. (2003). "Determination of the size of the representative volume element for random composites: statistical and numerical approach." *International Journal of Solids and Structures*, 40(13–14), 3647–3679.

102. Kanzaki, N., Ohmori, Y., and Ishimura, S. (1984). "The Use of Interlocking Block Pavements for the Reduction of Traffic Accident." *Second International Conference on Concrete Block Paving*, 200–206.

103. Al Kassem, G. (2009). *Micromechanical material models for polymer composites through advanced numerical simulation techniques*. PhD Dissertation, Mechanical Engineering, RWTH Aachen University.

104. Kellersmann, G. H. (1980). "Urban block paving The Netherlands." *First International Conference on Concrete Block Paving*, University of Newcastle-Upon-Tyne, England, 93–100.

105. Kellersmann, G. H., Klooster, J. v. D., Bosch, G. R., Beuving, E., Molenaar, A. A. A., and Moll, H. O. (1984). "Design Method for Concrete Block Pavement." *2nd International Conference on Concrete Block Paving, Deflt*, Delft Univ. of Technology, Netherlands, 100–114.

106. Kelly, P. J., Macleod, D., Knoesen, L., and Matthews, A. A. (1996). "Concrete Block Paving for Labour Based Construction of Roads- A South African Study." *Seventh International Conference on Concrete Block Paving*, Tel-Aviv, Israel, 171–181.

107. Khan, A., Puppala, A. J., Biswas, N., and Congress, S. S. C. (2023). "Evaluation of the structural performance of the geocell-stabilized flexible pavement." *Transportation Geotechnics*, Elsevier Ltd, 41.

108. Kief, O., and Rajagopal, K. (2008). "Three Dimensional Cellular Confinement System Contribution To Structural Pavement Reinforcement." *Geosynthetics India '08*, Indian Chapter of International Geosynthetics Society and Central Board of Irrigation & Power, Hyderabad, India, 1–12.

109. Kief, O., Rajagopal, K., Veeraragavan, A., and Chandramouli, S. (2011). "Modulus Improvement Factor for Geocell-Reinforced Bases." *In Proceedings, Geosynthetics India*, Central Board of Irrigation and Power, New Delhi, India, 14–52.

110. Kief, O., Schary, Y., and Pokharel, S. K. (2015). "High-Modulus Geocells for Sustainable Highway Infrastructure." *Indian Geotechnical Journal*, 45(4), 389–400.

111. Knapton, J. (1988). "A Review of Concrete Block Pavements at Ports in the UK." *Third International Conference on Concrete Block Paving*, Rome, Italy, 380–392.

112. Knapton, J. (1996). "The Romans and their roads—The original small element pavement technologists." *Seventh International Conference on Concrete Block Paving*, Tel-Aviv, Israel, 17–52.

113. Knapton, J., and Barber, S. D. (1980). "UK Research into Concrete Block Pavement Design." *First International Conference on Concrete Block Paving*, University of Newcastle-Upon-Tyne, England, 33–37.

114. Krishna, A., and Madhavi Latha, G. (2023). "Evolution of Geocells as Sustainable Support to Transportation Infrastructure." *Sustainability 2023*, 15(15).

115. Kumar, A., Scholar, D., Kumar, R., Scholar, P., Khan, S., and Kumar, S. (2013). "Analysis of Flexible Pavement Using IIT-PAVE Software." *European Chemical Bulletin*, 12(Special Issue 4), 14124–14145.

116. Lekso, S. (1980). "The use of concrete block pavements for highways." *First International Conference on Concrete Block Paving*, University of Newcastle-Upon-Tyne, England, 101–103.

117. Leshchinsky, B., and Ling, H. (2013). "Effects of Geocell Confinement on Strength and Deformation Behavior of Gravel." *Journal of Geotechnical and Geoenvironmental Engineering*, 139(2), 340–352.

118. Levi, M. (1889). "Pavement for Streets or Roads." United States Patent Office.

119. Likitlersuang, S., Teachavorasinskun, S., Surarak, C., Oh, E., and Balasubramaniam, A. (2013). "Small strain stiffness and stiffness degradation curve of Bangkok Clays." *Soils and Foundations*, Elsevier, 53(4), 498–509.

120. Lin, W., Cho, Y., and Kim, I. T. (2016). "Development of Deflection Prediction Model for Concrete Block Pavement Considering the Block Shapes and Construction Patterns." *Advances in Materials Science and Engineering*.

121. Lin, W., Dong, Y., Jung, Y. S., Zheng, H., and Cho, Y. (2021). "Performance Evaluation of Bedding Sand and Load Transfer Characteristic of Concrete Block Pavements." *Applied Sciences*, 11(21).

122. Liu, J., Shi, X., Qi, C., Chen, Z., Bu, F., Qian, W., Jiang, C., Lan, X., and Song, Z. (2021). "Mechanical Properties Improvement of Polyvinyl Acetate Polymer-Treated Sand with Plant Fiber Reinforcement." *Journal of Testing and Evaluation*, 49(3), 1927–1941.

123. Liu, W. K., Li, S., and Park, H. S. (2022). "Eighty Years of the Finite Element Method: Birth, Evolution, and Future." *Archives of Computational Methods in Engineering*, Springer Netherlands, 29, 4431–4453.

124. Luo, X., Lu, Z., Yao, H., Zhang, J., and Song, W. (2022). "Experimental study on soft rock subgrade reinforced with geocell." *Road Materials and Pavement Design*, Taylor & Francis, 23(9), 2190–2204.

125. Madhavi Latha, G. (2000). "Investigations on the behaviour of geocell supported embankments." Indian Institute of Technology Madras.

126. Madhavi Latha, G., Dash, S. K., and Rajagopal, K. (2008). "Equivalent continuum simulations of geocell reinforced sand beds supporting strip footings." *Geotechnical and Geological Engineering*, 26, 387–398.

127. Madhavi Latha, G., and Rajagopal, K. (2007). "Parametric finite element analyses of geocell-supported embankments." *Canadian Geotechnical Journal*, 44(8), 917–927.

128. Madhavi Latha, G., Rajagopal, K., and Krishnaswamy, N. R. (2006). "Experimental and Theoretical Investigations on Geocell-Supported Embankments." *International Journal of Geomechanics*, 6(1), 30–35.

129. Madhavi Latha, G., and Somwanshi, A. (2009). "Effect of reinforcement form on the bearing capacity of square footings on sand." *Geotextiles and Geomembranes*, Elsevier Ltd, 27, 409–422.

130. Maji, V. B., Sowmiyaa, V. S., and Robinson, R. G. (2016). "A Simple Analysis of Reinforced Soil Using Equivalent Approach." *International Journal of Geosynthetics and Ground Engineering*, Springer International Publishing, 2.

131. Mamatha, K. H., and Dinesh, S. V. (2019). "Performance evaluation of geocell-reinforced pavements." *International Journal of Geotechnical Engineering*, Taylor & Francis, 13(3), 277–286.

132. Mampearachchi, W. K., and Gunarathna, W. P. H. (2010). "Finite-Element Model Approach to Determine Support Conditions and Effective Layout for Concrete Block Paving." *Journal of Materials in Civil Engineering*, 22(11), 1139–1147.

133. Mampearachchi, W. K., and Senadeera, A. (2014). "Determination of the Most Effective Cement Concrete Block Laying Pattern and Shape for Road Pavement Based on Field Performance." *Journal of Materials in Civil Engineering*, 26(2), 226–232.

134. Marler, M. (2003). "Evaluating The Economic Empowerment Potential of Concrete Block Paved Roads for Developing Communities." *Seventh International Conference on Concrete Block Paving*, Sun City, South Africa.

135. Di Mascio, P., Moretti, L., and Capannolo, A. (2019). "Concrete block pavements in urban and local roads: Analysis of stress-strain condition and proposal for a catalogue." *Journal of Traffic and Transportation Engineering (English Edition)*, Elsevier Ltd, 6(6), 557–566.

136. Matthews, A. A., and Van Niekerk, A. J. (1996). "Practical Considerations of Labour Based Concrete Block PAving in Major Roadways." *Seventh International Conference on Concrete Block Paving*, Tel-Aviv, Israel, 183–192.

137. Meena, S., Choudhary, L., and Dey, A. (2013). "Quasi-static Analysis of Geotextile Reinforced Unpaved Road Resting on c-φ Subgrade." *Procedia - Social and Behavioral Sciences*, Elsevier B.V., 104, 235–244.

138. Menetrey, P., and Willam, K. J. (1995). "Triaxial Failure Criterion for Concrete and its Generalization." *ACI Structural Journal*, 92(3), 311–318.

139. Meyer, A. (1980). "Materials and Specifications in West Germany." *First International Conference on Concrete Block Paving*, University of Newcastle-Upon-Tyne, England, 8–10.

140. Mhaiskar, S. Y., and Mandal, J. N. (1996). "Investigations on soft clay subgrade strengthening using geocells." *Construction and Building Materials*, 10(4), 281–286.

141. Milder, G. J. W. (1992). "The Human Aspects of Concrete Block Paving." *Fourth International Conference on Concrete Block Paving*, Auckland, New Zealand, 181–186.

142. Mindiastiwi, T., Wu, P.-K., Siswanto, A. B., and Salim, M. A. (2021). "Triaxial Testing on Geogrid-reinforced Granular Soils." *IOP Conference Series: Materials Science and Engineering*, 1200(1), 012030.

143. Miura, Y., Yoshida, K., Mitsuru, K., and Saeki, Y. (1984). "On the serviceability of Concrete Block Pavements used on Streets and Bus Bays." *Second International Conference on Concrete Block Paving*, Delft, Netherlands, 212–215.

144. Molenaar, A. A. A., Moll, H. O., and Houben, L. J. M. (1984). "Structural Model for Concrete Block Pavement." *Transportation Research Record*, 954, 16–27.

145. Mori, T., Kasahara, A., Hara, T., and Tanaka, M. (2000). "In-Service Condition of IL Block Pavement Constructed as a Countermeasure To Plastic Flow." *6th International Conference on Concrete Block Paving*, Tokyo, Japan, 141–150.

146. Morin, D. (2008). "Lagrangian Method." *Introduction to Classical Mechanics: With Problems and Solutions*, Cambridge University Press, VI-1 to VI – 55.

147. Morrish, C. F. (1980). "Interlocking concrete paving–the state of the art in Australia." *First International Conference on Concrete Block Paving*, Newcastle, England, 85–92.

148. Morrish, C. F. (1986). "Current Usage of Interlocking Paving in Australia." *First International Workshop on Interlocking Concrete Pavements*, Melbourne, Australia, 5–10.

149. MoRTH. (2013). *Specifications for Road and Bridge Works (Fifth Revision)*. Indian Roads Congress on behalf of the Government of India, Ministry of Road Transport & Highway, New Delhi, India.

150. Muraleedharan, T. and Sood, V. K. (2003). "Past and Present Efforts for Popularisation of Interlocking Concrete Block Pavement Technology in India." *Seventh International Conference on Concrete Block Paving*, Sun City, South Africa, 3–11.

151. Nejad, F. M., and Shadravan, M. R. (2010). "A study on behavior of block pavement using 3D finite element method." *Computational Methods in Civil Engineering*, 1(1), 65–71.

152. Nicolson, S. (1854). "Improvement in Wooden Pavement." United States Patent Office.

153. Nishizawa, T. (2003). "A tool for structural analysis of block pavements based on 3DFEM." *Proceeding of the 7th International Conference on Concrete Block Paving*.

154. Nishizawa, T., Matsuno, S., and Komura, M. (1984). "Analysis of Interlocking Block Pavements By Finite Element Method." 80–85.

155. Noda, E., Kasahara, A., and Yaginuma, H. (2009). "Revised manual for interlocking block pavement design and construction (2007 version)." *9th International Conference on Concrete Block Paving*, Buenos Aires, Argentina, 1–11.

156. Ogierman, W., and Kokot, G. (2013). "Mean field homogenization in multi-scale modelling of composite materials." *Journal of Achievements in Materials and Manufacturing Engineering*, 61(2), 343–348.

157. Oller, S., Miquel Canet, J., and Zalamea, F. (2005). "Composite material behavior using a homogenization double scale method." *Journal of Engineering Mechanics*, 131(1), 65–79.

158. Omoto, S., Yaginuma, H., Ando, Y., and Toriiminami, K. (2009). "Case Study for the Good Long-Term Serviceability of Interlocking Block Pavement." *9th International Conference on Concrete Block Paving*, Buenos Aires, Argentina, 1–11.

159. Omoto, S., Yaginuma, K., Ando, Y., and Toriiminami, K. (2006). "Investigations into and Evaluation of the Serviceability and Causes of Breakage of Interlocking Block Pavement in Japan." *8th International Conference on Concrete Block Paving*, San Francisco, California, USA, 401–410.

160. Önal, Y., Çalışıcı, M., Kayadelen, C., and Gökhan, A. (2023). "A comparative experimental study of geocell and geogrid-reinforced highway base layers under repeated loads." *Road Materials and Pavement Design*.

161. Öncü, Ş., and Bilsel, H. (2017). "Influence of Polymeric Fiber Reinforcement on Strength Properties of Sand-stabilized Expansive Soil." *Polymer - Plastics Technology and Engineering*, Taylor & Francis, 56(4), 391–399.

162. Pancar, E. B., and Akpinar, M. V. (2016). "Comparison of Effects of Using Geosynthetics and Lime Stabilization to Increase Bearing Capacity of Unpaved Road Subgrade." *Advances in Materials Science and Engineering*, Hindawi, 2016.

163. Panda, B. C. (2006). "Load dispersion ability of concrete block layers." *Eighth International Conference on Concrete Block Paving*, 433–446.

164. Panda, B. C. (2009). “Load dispersion profile of block layer in interlocking Concrete Block Pavement.” *Indian Concrete Journal*, 83(7), 11–16.

165. Panda, B. C., and Ghosh, A. K. (2002a). “Structural behavior of concrete block paving. I: Sand in bed and joints.” *Journal of Transportation Engineering*, 128(2), 123–129.

166. Panda, B. C., and Ghosh, A. K. (2002b). “Structural behavior of concrete block paving II: Concrete Blocks.” *Journal of Transportation Engineering*, 128(2), 130–135.

167. Panda, B. C., and Pani, A. K. (2020a). “Load Deflection Profile of Concrete Block Pavement.” *Journal of The Institution of Engineers (India): Series A*, Springer India, 101(4), 743–751.

168. Panda, B. C., and Pani, A. K. (2020b). “Load Deflection Profile of Concrete Block Pavement.” *Journal of The Institution of Engineers (India): Series A*, 101, 743–751.

169. Patel, K. K., and Singh, D. V. P. (2023). “Study of chemically treated natural plant fibers in soil reinforcement technology: A review.” *Materials Today: Proceedings*, 78(1), 55–61.

170. Peng, B., and Yu, W. (2018). “A micromechanics theory for homogenization and dehomogenization of aperiodic heterogeneous materials.” *Composite Structures*, Elsevier, 199, 53–62.

171. Perdahcioğlu, E. S., and Geijselaers, H. J. M. (2011). “Constitutive modeling of two phase materials using the mean field method for homogenization.” *International Journal of Material Forming*, 4, 93–102.

172. Pinho-da-Cruz, J., Oliveira, J. A., and Teixeira-Dias, F. (2009). “Asymptotic homogenisation in linear elasticity. Part I: Mathematical formulation and finite element modelling.” *Computational Materials Science*, Elsevier B.V., 45(4), 1073–1080.

173. Pokharel, S. K., Han, J., Leshchinsky, D., and Parsons, R. L. (2018). “Experimental evaluation of geocell-reinforced bases under repeated loading.” *International Journal of Pavement Research and Technology*, Chinese Society of Pavement Engineering, 11(2), 114–127.

174. Pokharel, S. K., Han, J., Leshchinsky, D., Parsons, R. L., and Halahmi, I. (2010). “Investigation of factors influencing behavior of single geocell-reinforced bases under static loading.” *Geotextiles and Geomembranes*, Elsevier Ltd, 28(6), 570–578.

175. Rada, B. G. R., Member, A., Smith, D. R., Miller, J. S., Member, A., and Witczak, M. W. (1990). “Structural Design of Concrete Block Pavements.” *Journal of Transportation Engineering*, 116(5), 615–635.

176. Rada, G. R., Smith, D. R., Miller, J. S., and Witczak, M. W. . (1992). “Structural Design of Interlocking Concrete Pavements in North America.” *4th International Conference on Concrete Block Paving*, Auckland, New Zealand, 99–115.

177. Rajagopal, K., Krishnaswamy, N. R., and Madhavi Latha, G. (1999). “Behaviour of sand confined with single and multiple geocells.” *Geotextiles and Geomembranes*, 17(3), 171–184.

178. Rajagopal, K., Veeragavan, A., and Chandramouli, S. (2012). “Studies on geocell reinforced road pavement structures.” *GA 2012 - 5th Asian Regional Conference on Geosynthetics: Geosynthetics for Sustainable Adaptation to Climate Change*, Asian Center for Soil Improvement and Geosynthetics., 497–502.

179. Rao, W., Yu, C., Zhang, J., and Kang, G. (2021). "New incremental secant linearization method for mean-field homogenization approach of elasto-viscoplastic microscopic heterogeneous materials." *Composite Structures*, Elsevier Ltd, 271, 114125.

180. Rodrigues, D. E. S., Belinha, J., Pires, F. M. A., Dinis, L. M. J. S., and Jorge, R. M. N. (2018). "Material homogenization technique for composites: A meshless formulation." *Science and Technology of Materials*, 30(1), 50–59.

181. Rollings, R. S. (1983). *Technical Report on Concrete Block Pavement (GL-83-3)*.

182. Rollings, R. S. (1984). "Corps of Engineers Design Method for Concrete Block Pavements." *2nd International Conference on Concrete Block Paving*, Delft, Netherlands, 147–151.

183. Rollings, R. S. (1986). "Evaluation of Block Pavement Design Procedures." *First International Workshop on Interlocking Concrete Pavements*, Australian Road Research Board, Melbourne, Australia, 123–132.

184. Rollings, R. S., Rollings, M. P., and Sharp, K. G. (1992). "Evaluation of Thickness Design Concepts for Block Pavements." *4th International Conference on Concrete Block Paving*, Auckland, New Zealand, 61–70.

185. Ryntathiang, T. L., Mazumdar, M., and Pandey, B. B. (2006). "Concrete block pavement for low volume roads." *8th International Conference on Concrete Block Paving*, San Francisco, California, USA, 359–374.

186. Saha, G. P., and Kabir, M. H. (1988). "Design of geotextile and geogrid reinforced unpaved roads." *International Geotechnical Symposium on Theory and Practice of Earth Reinforcement*, T. Yamanouchi, N. Miura, and H. Ochiai, eds., CRC PRess, Taylor and Francis Group, Fukuoka, Japan, 233–238.

187. Sapkota, A. (2022). "Microbial degradation of cellulose (Enzymes, Steps, Mechanisms)." *Microbe Notes*, <https://microbenotes.com/microbial-degradation-of-cellulose/> (Sep. 17, 2023).

188. Saride, S., Baadiga, R., Balunaini, U., and Madhira, M. R. (2022). "Modulus Improvement Factor-Based Design Coefficients for Geogrid-and Geocell-Reinforced Bases." *Journal of Transportation Engineering, Part B: Pavements*, 148(3), 1–14.

189. Saride, S., Gowrisetti, S., Sitharam, T. G., and Puppala, A. J. (2009). "Numerical simulation of geocell-reinforced sand and clay." *Proceedings of the Institution of Civil Engineers: Ground Improvement*, 162(4), 185–198.

190. Schmitz, A., and Horst, P. (2014). "A finite element unit-cell method for homogenised mechanical properties of heterogeneous plates." *Composites Part A: Applied Science and Manufacturing*, Elsevier Ltd, 61, 23–32.

191. Shackel, B. (1980). "The performance of interlocking block pavements under accelerated trafficking." *First International Conference on Concrete Block Paving*, University of Newcastle-Upon-Tyne, England, 113–120.

192. Shackel, B. (1986). "A Review of Research into Concrete Segmental Pavers in Australia." *First International Workshop on Interlocking Concrete Pavements*, Melbourne, Australia, 11–18.

193. Shackel, B. (2000). "The Development and Application of Mechanistic Design Procedures for Concrete Paving." *6th International Conference on Concrete Block Paving*.

194. Shackel, B., and Candy, C. C. E. (1988). "Factors influencing the choice of concrete blocks as a pavement surface." *Third International Conference on Concrete Block Paving*, Rome, Italy, 78–84.

195. Shackel, B., Pearson, A., and Vella, A. (1998). "Progress towards a maintenance management for concrete block pavements in Australia." *3rd International Workshop on Concrete Block Paving*, Cartagena de Indias, Columbia, 37–1 to 9.

196. Shafabakhsh, G. A., Family, A., and Abad, B. P. H. (2014). "Numerical Analysis of Concrete Block Pavements and Comparison of its Settlement with Asphalt Concrete Pavements using Finite Element Method." *Engineering Journal*, 18(4), 39–51.

197. Shafer, T. J. (2006). "A Case History of Concrete Block Papers at Dundalk and Seagirt Marine Terminals." *8th International Conference on Concrete Block Paving*, California, USA, 757–766.

198. Shahzamanian, M. M., Akhtar, S. S., Arif, A. F. M., Basirun, W. J., Al-Athel, K. S., Schneider, M., Shakelly, N., Hakeem, A. S., Abubakar, A. A., and Wu, P. D. (2022). "Thermo-mechanical properties prediction of Ni-reinforced Al2O3 composites using micro-mechanics based representative volume elements." *Scientific Reports*, 12, 11076 (2022).

199. Sharp, K. G., and Armstrong, P. J. (1984). "Testing of Concrete Block Pavements By the Australian Road Research Board." *Second International Conference on Concrete Block Paving*, Delft, Netherlands, 40–49.

200. Sheikh, I. R., Mandhaniya, P., and Shah, M. Y. (2021). "A Parametric Study on Pavement with Geocell Reinforced Rock Quarry Waste Base on Dredged Soil Subgrade." *International Journal of Geosynthetics and Ground Engineering*, Springer International Publishing, 7, 1–11.

201. Shin, E. C., Das, B. M., Lee, E. S., and Atalar, C. (2002). "Bearing capacity of strip foundation on geogrid-reinforced sand." *Geotechnical and Geological Engineering*, 20, 169–180.

202. Simulia. (2021). "Abaqus/CAE." Dassault Systèmes Simulia Corp, 92210 Saint-Cloud, France.

203. Simulia. (2022). "Micromechanics Plugin- Version 1.18." Dassault Systèmes, 92210 Saint-Cloud, France.

204. Soutsos, M. N., Tang, K., Khalid, H. A., and Millard, S. G. (2011). "The effect of construction pattern and unit interlock on the structural behaviour of block pavements." *Construction and Building Materials*, Elsevier Ltd, 25, 3832–3840.

205. Sujatha, E. R., Atchaya, P., Darshan, S., and Subhashini, S. (2021). "Mechanical properties of glass fibre reinforced soil and its application as subgrade reinforcement." *Road Materials and Pavement Design*, Taylor & Francis, 22(10), 2384–2395.

206. Superczyńska, M., Józefiak, K., and Zbiciak, A. (2016). "Numerical Analysis of Diaphragm Wall Model Executed in Poznań Clay Formation Applying Selected FEM Codes." *Archives of Civil Engineering*, 62(3), 207–224.

207. Suquet, P. M. (1985). "Part IV Elements of Homogenization for Inelastic Solid Mechanics." *Homogenization Techniques for Composite Media*, E. Sanchez-Palencia and A. Zaoui, eds., Springer, Berlin, Heidelberg, 193–198.

208. Taheri, V., Fakhri, M., and Hayati, P. (2021). "Evaluation of airfield concrete block pavements based on 3-D modelling and plate loading test." *Construction and Building Materials*, Elsevier Ltd, 280.

209. Tang, X., and Yang, M. (2013). "Investigation of Flexural Behavior of Geocell Reinforcement Using Three-Layered Beam Model Testing." *Geotechnical and Geological Engineering*, 31, 753–765.

210. Tchalla, A., Belouettar, S., Makradi, A., and Zahrouni, H. (2013). "An ABAQUS toolbox for multiscale finite element computation." *Composites Part B: Engineering*, Elsevier Ltd, 52, 323–333.

211. Thakur, J. K., Han, J., Pokharel, S. K., and Parsons, R. L. (2012). "Performance of geocell-reinforced recycled asphalt pavement (RAP) bases over weak subgrade under cyclic plate loading." *Geotextiles and Geomembranes*, Elsevier Ltd, 35, 14–24.

212. Thomaz, W. de A., Miyaji, D. Y., and Possan, E. (2021). "Comparative study of dynamic and static Young's modulus of concrete containing basaltic aggregates." *Case Studies in Construction Materials*, Elsevier Ltd, 15.

213. Tian, W., Qi, L., Chao, X., Liang, J., and Fu, M. (2019). "Periodic boundary condition and its numerical implementation algorithm for the evaluation of effective mechanical properties of the composites with complicated micro-structures." *Composites Part B: Engineering*, Elsevier, 162, 1–10.

214. Tohall, P., Vries, H. De, and Zeist, W. van. (1955). "A Trackway in Corlona Bog, Co. Leitrim." *The Journal of the Royal Society of Antiquaries of Ireland*, 85(1), 77–83.

215. Tootkaboni, M., and Graham-Brady, L. (2010). "A multi-scale spectral stochastic method for homogenization of multi-phase periodic composites with random material properties." *International Journal for Numerical Methods in Engineering*, 83(1), 59–90.

216. Uchida, K., Ohmori, H., and Nishi, J. (1992). "Structural design of interlocking concrete block pavement in Japan." *Fourth International Conference on Concrete Block Paving*, Auckland, New Zealand, 71–78.

217. van der Vlist, A. A. (1980). "The Development of Concrete Paving Blocks in the Netherlands." *First International Conference on Concrete Block Paving*, University of Newcastle-Upon-Tyne, England, 14–22.

218. Webster, S. L. (1981). *Investigation of Beach Sand Trafficability Enhancement Using Sand-Grid Confinement and Membrane Reinforcement Concepts-Report 2 (Technical Report GL-79-20). Waterways Experiment Station, U. S. Army Corps of Engineers*, Vicksburg, Mississippi, United States.

219. Wojciechowski, M. (2018). "Weakened Hill-Mandel Condition for Computational Homogenisation of Random Media." *41st Solid Mechanics Conference (SOLMECH 2018)*, Institute of Fundamental Technological Research Polish Academy of Sciences, Warsaw, Poland, 68–69.

220. Yaginuma, H., and Kasahara, A. (2006). "Load transfer efficiency in interlocking block pavements with joint and bedding sand." *8th International Conference on Concrete Block Paving*, 421–432.

221. Yaginuma, H., Tanaka, M., Kasahara, A., and Yazawa, S. (2003). "Development of a standard for block dimensions for use under Japanese conditions." *7th International Conference on Concrete Block Paving*, Sun City, South Africa.

222. Yang, X., and Han, J. (2013). "Analytical Model for Resilient Modulus and Permanent Deformation of Geosynthetic-Reinforced Unbound Granular Material." *Journal of Geotechnical and Geoenvironmental Engineering*, 139(9), 1443–1453.

223. Yang, X., Han, J., Leshchinsky, D., and Parsons, R. L. (2013). "A three-dimensional mechanistic-empirical model for geocell-reinforced unpaved roads." *Acta Geotechnica*, 8, 201–213.

224. Yang, X., Han, J., Parsons, R. L., and Leshchinsky, D. (2010). "Three-dimensional numerical modeling of single geocell-reinforced sand." *Frontiers of Architecture and Civil Engineering*, 4(2), 233–240.

225. Yang, X., Han, J., Pokharel, S. K., Manandhar, C., Parsons, R. L., Leshchinsky, D., and Halahmi, I. (2012). "Accelerated pavement testing of unpaved roads with geocell-reinforced sand bases." *Geotextiles and Geomembranes*, Elsevier Ltd, 32, 95–103.

226. Yang, Z., Sun, Y., Huang, S., and Yang, Z. (2021). "A higher-order three-scale reduced homogenization approach for nonlinear mechanical properties of 3D braided composites." *International Journal of Mechanical Sciences*, Elsevier Ltd, 208, 106684.

227. Yasuhisa, K., Ando, Y., Omoto, S., Yaginuma, K., and Toriiminami, K. (2006). "Study on Block Shifting of Interlocking Block Pavement." *8th International Conference on Concrete Block Paving*, 447–456.

228. Yoshida, S., McGibboney, C., and Sasaki, T. (2020). "Nondestructive Evaluation of Solids Based on Deformation Wave Theory." *Applied Sciences*, 10(16).

229. Yünkül, K., Usluoğulları, Ö. F., and Gürbüz, A. (2021). "Numerical Analysis of Geocell Reinforced Square Shallow Horizontal Plate Anchor." *Geotechnical and Geological Engineering*, 39, 3081–3099.

230. Zabihyan, R., Mergheim, J., Javili, A., and Steinmann, P. (2018). "Aspects of computational homogenization in magneto-mechanics: Boundary conditions, RVE size and microstructure composition." *International Journal of Solids and Structures*, Elsevier Ltd, 130–131, 105–121.

231. Zhang, L., Zhao, M., Shi, C., and Zhao, H. (2010). "Bearing capacity of geocell reinforcement in embankment engineering." *Geotextiles and Geomembranes*, Elsevier Ltd, 28(5), 475–482.

232. Zhao, Y., Ling, X., Gong, W., Li, P., Li, G., and Wang, L. (2020). "Mechanical properties of fiber-reinforced soil under triaxial compression and parameter determination based on the Duncan-Chang model." *Applied Sciences*, 10(24), 1–16.

233. Zhou, H., and Wen, X. (2008). "Model studies on geogrid- or geocell-reinforced sand cushion on soft soil." *Geotextiles and Geomembranes*, 26(3), 231–238.

234. Zoccali, P., Moretti, L., Di Mascio, P., Loprencipe, G., D'Andrea, A., Bonin, G., Teltayev, B., and Caro, S. (2018). "Analysis of natural stone block pavements in urban shared areas." *Case Studies in Construction Materials*, Elsevier, 8, 498–506.